Diagnostic Tools for Lithium-ion Batteries

Catarina Matias Vieira

Thesis to obtain the Master of Science Degree in

Materials Engineering

Supervisor: Prof. João Salvador Fernandes

Examination Committee

Chairperson: Prof. José Paulo Sequeira Farinha
Supervisor: Prof. João Carlos Salvador Fernandes
Members of the Committee: Prof. Raquel Alexandra Galamba Duarte

November 2022

Declaration

I declare that this document is an original work of my own authorship and that it fulfills all the requirements of the Code of Conduct and Good Practices of the Universidade de Lisboa.

Declaração

Declaro que o presente documento é um trabalho original da minha autoria e que cumpre todos os requisitos do Código de Conduta e Boas Práticas da Universidade de Lisboa.

Acknowledgments

To my supervisor, Professor João Salvador Fernandes, for giving me the opportunity to work on this project and for all the guidance and time that was placed in me.

To my colleague Luísa Chiavassa, for helping me settle in the laboratory and for all the support while carrying out the experimental work of this thesis. To Professor Raquel Duarte for the important advice and dedication.

To my parents, Helena and José, and to my sister Margarida for always supporting and motivating me during the most challenging times, thank you for always believing in me.

To my dear friends and colleagues Ana Marta, Catarina and Rita for being always by my side during these five years. All my accomplishments during this course would not have been possible without your constant support, motivation, patience and friendship.

Lastly to all my friends and laboratory colleagues for the constant support.

Abstract

One of the main difficulties associated with the management of end-of-life electric vehicle batteries is related to the diagnosis of their state of health (SOH). This diagnosis is fundamental to evaluate the battery's state compared to its initial state, and thus making a decision regarding its possible use in second life applications.

The goal of this work is to understand the degradation phenomena of lithium-ion batteries by applying the Electrochemical Impedance Spectroscopy technique over charge-discharge cycles, with subsequent analysis through an Electrical Equivalent Circuit.

Determining the SOH of a battery based on capacity loss requires applying a full charge and discharge, and this process is quite time consuming and impractical. Alternatively, the SOH can be calculated based on the internal resistance of the cell.

A new cell, a cell already used in an electric vehicle, two new cells connected in parallel and two used cells connected in parallel were tested over 50 charge-discharge cycles. Through analysis of the impedance spectra and the Electrical Equivalent Circuit it was found that the internal resistance is the parameter that contributes most to the total impedance of the cell and that the variation of the internal resistance may be used as an indicator of the evolution of the capacity.

Different methods for determining SOH based on impedance and internal resistance are presented and tested in order to seek a correlation with the SOH values calculated using capacity.

Keywords

Lithium-ion Batteries, State-of-Health, Electrochemical Impedance Spectroscopy, Charge-discharge cycles, Electrical Equivalent Circuit.

Resumo

Uma das principais dificuldades associadas à gestão das baterias de veículos elétricos em fim de vida prende-se com o diagnóstico do seu estado de saúde (SOH). Este diagnóstico é fundamental para avaliar o estado da bateria comparativamente ao seu estado inicial, e assim tomar uma decisão quanto à sua possível utilização em aplicações de segunda vida.

O objetivo deste trabalho é compreender os fenómenos de degradação de baterias de iões-lítio através da aplicação da técnica de Espetroscopia de Impedância Eletroquímica ao longo de ciclos de carga-descarga, com posterior análise através de um Circuito Elétrico Equivalente.

Para determinar o SOH de uma bateria com base na perda de capacidade é necessário aplicar uma carga e uma descarga completas, sendo este processo bastante demorado e pouco prático. Alternativamente, o SOH pode ser calculado com base na resistência interna da célula.

Uma célula nova, uma célula já usada num veículo elétrico, duas células novas em paralelo e duas células usadas em paralelo foram testadas ao longo de 50 ciclos de carga-descarga. Através da análise dos espetros de impedância e do Circuito Elétrico Equivalente foi verificado que a resistência interna é o parâmetro que mais contribui para a impedância total da célula e que a variação da resistência interna pode ser usada como indicador da evolução da capacidade.

Diferentes métodos para a determinação do SOH com base na impedância e resistência interna são apresentados e testados de forma a procurar uma correlação com os valores de SOH calculados através da capacidade.

Palavras Chave

Baterias de iões-lítio, State-of-Health, Espetroscopia de Impedância Eletroquímica, Ciclos de carga-descarga, Circuito Elétrico Equivalente.

Contents

List of Tables xi

List of Figures xiii

Acronyms xvii

1 | Introduction 1

- 1.1 Background 1
  - 1.1.1 Battery electric vehicles 2
  - 1.1.2 Hybrid electric vehicles 2
  - 1.1.3 Plug-in hybrid electric vehicles 3
  - 1.1.4 Battery Management System 3
- 1.2 Problem definition 4
- 1.3 Objective and selected approach 5

2 | Literature Review 7

- 2.1 Batteries 7
  - 2.1.1 Primary Batteries 7
  - 2.1.2 Secondary Batteries 8
    - 2.1.2.1 Lithium-ion batteries 9
- 2.2 Ageing Mechanisms 12
  - 2.2.1 Degradation Modes 12
- 2.3 Battery State Estimation 15
  - 2.3.1 Battery State Indicators 16
    - 2.3.1.1 State-of-Charge 16
    - 2.3.1.2 State-of-Energy 16
    - 2.3.1.3 State-of-Power 17
    - 2.3.1.4 State-of-Temperature 17
    - 2.3.1.5 State-of-Safety 17
    - 2.3.1.5 State-of-Health 18

3 | Methodology 19

- 3.1 Charge-discharge cycles 19
  - 3.1.1 C-rates 20
- 3.2 Electrochemical Impedance Spectroscopy 22
  - 3.2.1 Nyquist diagram 23
  - 3.2.2 Bode diagram 24
  - 3.2.3 EIS applied to batteries 25
    - 3.2.3.1 Electrical circuit elements 26
  - 3.2.4 Electrical Equivalent Circuit 28

3.2.5 EEC of a lithium-ion battery 29
3.2.5 Influence of ageing on a battery’s impedance 31
4 | Experimental Part 33
4.1 Equipment and material 33
4.2 Procedure 34
4.2.1 Cycling and EIS testing of individual cells 34
4.2.1.1 New cell 35
4.2.1.2 Used cell 36
4.2.2 Cycling and EIS tests of two parallel-connected cells 37
4.2.2.1 New cells 37
4.2.2.2 Used cells 39
5 | Results and Discussion 41
5.1 Capacity and impedance analysis of individual cells 41
5.1.1 Capacity and impedance analysis of a new cell 41
5.1.2 Capacity and impedance analysis of a used cell 48
5.2 Capacity and impedance analysis of two parallel-connected cells 55
5.2.1 Capacity and impedance analysis of two new cells 55
5.2.2 Capacity and impedance analysis of two used cells 60
5.3 SOH definition based on resistance 63
6| Conclusions 76
6.1 Future Work 77

List of Tables

Table 1: Properties of commercially available secondary batteries [11 ,20, 21]. 8

Table 2: Influence of extrinsic factors on the ageing mechanisms of a LIB and associated degradation modes [8, 35]. 14

Table 3: Current-voltage relationship and impedance of simple circuit elements [12, 44]. 26

Table 4: Specifications of Panasonic NCR18650 cells [53]. 34

Table 5: Specifications of Panasonic NCR18650B cells [43]. 34

Table 6: Selected parameters for the EIS tests. 35

List of Figures

Figure 1: EV battery demand by mode, 2015-2020 [5]. 1

Figure 2: Types of electric vehicles. 2

Figure 3: a. Without a BMS cells within a battery can have charge imbalance, with some overcharged or overdischarged cells; b. BMS ensures protection, constant monitoring and charge balance among all cells [11]. 4

Figure 4: Specific Power (W/kg) and Specific Energy (Wh/kg) of different types of secondary cells [22]. 9

Figure 5: Structure of a lithium-ion battery [26]. 9

Figure 6: a. Cylindrical; b. prismatic; and c. pouch Li-ion cells. 10

Figure 7: Ion and electron flow during discharging and charging in lithium-ion batteries [26]. 11

Figure 8: Ageing mechanisms of lithium-ion batteries and their respective degradation modes [8]. 12

Figure 9: The same charge throughput at different SOC corresponds to a different amount of released energy. 17

Figure 10: Influence of discharge current on discharge profile and discharge capacity [43]. 20

Figure 11: Typical potential charge (dark green) and discharge (dark blue) profiles and charge (light green) and discharge (light green) current curves of a Li-ion battery [3]. 21

Figure 12: Capacity evolution of a battery with cycling, in Ampere hour (darker points) and percentage (lighter points), calculated during charging (green) and discharging (blue) [3]. 21

Figure 13: The applied voltage signal and the current response are shifted in phase [44]. 22

Figure 14: Lissajous Figure [41]. 23

Figure 15: Representation of |Z| as a vector in a Nyquist plot [44]. 24

Figure 16: Representation of a Bode diagram [44]. 25

Figure 17: Nyquist plot of a charged NCA battery. 26

Figure 18: R_{int}, R_{SEI} and R_{CT} on a Nyquist plot [23]. 28

Figure 19: Circuit elements in series [44]. 28

Figure 20: Circuit elements in parallel [44]. 28

Figure 21: Electrical Equivalent Circuit of a Lithium-ion battery [23]. 30

Figure 22: Simplified Electrical Equivalent Circuit for a lithium-ion battery [27]. 31

Figure 23: a. New Panasonic NCR18650B cells; b. Used Panasonic NCR18650 cells in an EV battery module. 33

Figure 24: Expected runtime of a single cycle for a new cell. 36

Figure 25: Expected runtime of a single cycle for a used cell. 37

Figure 26: Expected runtime of a single “long cycle” for two new cells in parallel. 38

Figure 27: Expected runtime of a single “fast cycle” for two new cells in parallel. 39

Figure 28: Expected runtime of a single “long cycle” for two used cells in parallel. 40

Figure 29: Expected runtime of a single “fast cycle” for two used cells in parallel. 40

Figure 30: Electrical Equivalent Circuit defined for the lithium-ion batteries being studied. 41

Figure 31: Capacity of a NCR18650B new cell over 50 charge-discharge cycles. 41

Figure 32: Full Nyquist plots of the new cell at different charge states in the a. 1st cycle; b. 50th cycle.42

Figure 33: Nyquist plots of the new cell at different charge states in the a. 1st cycle; b. 50th cycle, with R_{int} subtracted to all the spectra. 43

Figure 34: Nyquist plots of a new cell at different charge states for the 1st and 50th cycles. 44

Figure 35: a. Nyquist plots of the charged new cell for every 10 cycles; b. Nyquist plots of the discharged new cell for every 10 cycles........ 45

Figure 36: a. Nyquist plots of the charged new cell for every 10 cycles, moved to $R_{int} = 0\ \Omega$; Nyquist plots of the discharged new cell for every 10 cycles, moved to $R_{int} = 0\ \Omega$. 46

Figure 37: a. Impedance of a charged new cell between the 10th and 20th cycle, with R_{int} subtracted to all the spectra; b. Impedance of a charged new cell between the 20th and the 30th cycle, with R_{int} subtracted to all the spectra. 47

Figure 38: R_{int}, R_{SEI}, R_{CT} and W_o of the charged new cell over cycling. 48

Figure 39: Capacity of a NCR18650 module cell over 50 charge-discharge cycles. 49

Figure 40: Full Nyquist plots of the used cell at different charge states in the a. 1st cycle; b. 50th cycle. 50

Figure 41: Nyquist plots of the used cell at different charge states in the a. 1st cycle; b. 50th cycle, with R_{int} moved to the origin of the coordinate system. 51

Figure 42: Nyquist plots of a used cell at different charge states for the 1st and 50th cycles. 51

Figure 43: a. Nyquist plots of the charged used cell for every 10 cycles; b. Nyquist plots of the discharged used cell for every 10 cycles. 52

Figure 44: a. Impedance of a charged used cell between the 20th and 30th cycle; b. Impedance of a charged used cell between the 30th and the 40th cycle. 52

Figure 45: a. Nyquist plots of the charged used cell for every 10 cycles, moved to $R_{int} = 0\ \Omega$; Nyquist plots of the discharged used cell for every 10 cycles, moved to $R_{int} = 0\ \Omega$. 53

Figure 46: Voltage instability in a charge curve of the used cell (50th cycle). 54

Figure 47: R_{int}, R_{SEI}, R_{CT} and W_o of the charged used cell over cycling. 54

Figure 48: Nyquist diagrams in the charged state of new and used cells at the 1st and 50th charge-discharge cycle. 55

Figure 49: Capacity of two parallel-connected NCR18650B new cells over 50 charge-discharge cycles. 55

Figure 50: Electrical equivalent circuit for two cells in parallel. 56

Figure 51: Full Nyquist plots of the two parallel-connected new cells at different charge states in the a. 1st cycle; b. 50th cycle. 57

Figure 52: Nyquist plots of two new cells connected in parallel at the charged and discharged states for the 1st and 50th cycles. 58

Figure 53: a. Impedance of two charged new cells connected in parallel for every 10 cycles; b. Impedance of charged new cells connected in parallel for every 10 cycles, moved to $R_{int} = 0\ \Omega$. 59

Figure 54: Capacity of two parallel-connected module used cells over 50 charge-discharge cycles... 60

Figure 55: Full Nyquist plots of the two parallel-connected used cells at different charge states in the a. 1st cycle; b. 50th cycle. 61

Figure 56: Nyquist plots of two used cells connected in parallel at the charged and discharged states for the 1st and 50th cycles. 62

Figure 57: a. Impedance of two charged used cells connected in parallel for every 10 cycles; b. Impedance of charged used cells connected in parallel for every 10 cycles, moved to $R_{int} = 0\ \Omega$. 62

Figure 58: Evolution of R_{int} of the new charged and discharged cell, R_{int}(C) and R_{int}(D), respectively, R_{SEI}, R_{CT}, W_o and |Z| of the new cell at charged state with cycling. 63

Figure 59: Evolution of R_{int} of the used charged and discharged cell, R_{int}(C) and R_{int}(D), respectively, R_{SEI}, R_{CT}, W_o and |Z| of the used cell at charged state with cycling. 64

Figure 60: Evolution of R_{int} of the new charged and discharged cells, R_{int}(C) and R_{int}(D), respectively, R_{SEI}, R_{CT}, W_o and |Z| of the two new parallel-connected cells at charged state with cycling. 64

Figure 61: Evolution of R_{int} of the used charged and discharged cell, R_{int}(C) and R_{int}(D), R_{SEI}, R_{CT}, W_o and |Z| of the two used parallel-connected cells at charged state with cycling. 65

Figure 62: Capacity and R_{int} variation of a new charged cell over cycling. 66

Figure 63: Capacity and R_{int} variation of a used charged cell with cycling. 66

Figure 64: Capacity and R_{int} variation of two new cells connected in parallel with cycling. 67

Figure 65: Capacity and R_{int} variation of two used cells connected in parallel with cycling. 67

Figure 66: SOH calculated based on capacity, SOH(C) and based on resistance replacement criteria, SOH(2) for a. the new cell; b. the used cell; c. the parallel-connected new cells; d. the parallel-connected used cells. 69

Figure 67: SOH of the new cell calculated based on capacity, SOH(C), internal resistance, SOH(R), impedance modulus at the lowest frequency, SOH(Z), and battery replacement criteria, SOH(2). 71

Figure 68: SOH of the used cell calculated based on capacity, SOH(C), internal resistance, SOH(R), impedance modulus at the lowest frequency, SOH(Z), and battery replacement criteria, SOH(2). 71

Figure 69: SOH of the used cell calculated based on capacity, SOH(C), internal resistance, SOH(R), and impedance modulus at the lowest frequency, SOH(Z). 72

Figure 70: SOH of the two new cells in parallel, calculated based on capacity, SOH(C), internal resistance, SOH(R), impedance modulus at the lowest frequency, SOH(Z) and battery replacement criteria, SOH(2). 73

Figure 71: SOH of the two used cells in parallel, calculated based on capacity, SOH(C), internal resistance, SOH(R), impedance modulus at the lowest frequency, SOH(Z) and battery replacement criteria, SOH(2). 73

Acronyms

BEV Battery electric vehicle.

BMS Battery management system.

CC-CV Constant current-constant voltage.

CL Conductivity loss.

CPE Constant phase element.

DM Degradation mode.

DOD Degree of discharge.

EEC Electrical equivalent circuit.

EIS Electrochemical Impedance Spectroscopy.

EV Electric vehicle.

GHG Greenhouse gases.

HEV Hybrid electric vehicle.

ICEV internal combustion engine vehicle.

LAM Loss of active material.

LCO Lithium cobalt oxide.

LFP Lithium iron phosphate.

LIB Lithium-ion battery.

LLI Loss of lithium inventory.

LMO Lithium manganese oxide.

LTO Lithium titanium oxide.

LTS Lithium titanium disulfide.

NCA Nickel cobalt aluminum oxide.

NCR Nickel cobalt aluminum oxide rechargeable.

NMC Nickel manganese cobalt oxide.

PHEV Plug-in hybrid electric vehicle.

SEI Solid Electrolyte Interphase.

SOC State-of-Charge.

SOE State-of-Energy.

SOH State-of-Health.

SOP State-of-Power.

SOS State-of-Safety.

SOT State-of-Temperature.

1 Introduction

1.1 Background

Given the increasing growth in global energy consumption over the years and the reliance on fossil fuels as the energy source, the problems associated with greenhouse gas (GHG) emissions into the atmosphere and the scarcity of these non-renewable energy sources are intensifying. To reverse these problems, it is urgent to find alternatives for more sustainable and cleaner energy production, greenhouse gas emissions reduction and more efficient energy storage [1, 2].

Energy storage through batteries becomes advantageous as those are compact and portable devices, so they can be used for stationary and mobile applications, and for both smaller and larger devices, such as vehicles and power plants. Due to the growing demand for batteries for various applications, the need to study and develop increasingly more efficient, lower cost, and more power and energy-dense batteries arises [1, 3].

In the transportation sector, light commercial vehicles contribute substantially to overall greenhouse gas emissions and energy consumption. As the number of light-duty vehicles in operation is expected to increase in the coming years, the demand for fossil fuels will tend to intensify [2, 4].

Aiming to reverse this trend, the development of new technologies in the transport sector started to get more attention, notably with the reintroduction of electric vehicles (EVs). The demand for EV batteries has been growing fast, increasing from about 40 to 155 GW/year between 2015 and 2020, with a particularly significant growth for light-duty vehicles. (Figure 1).

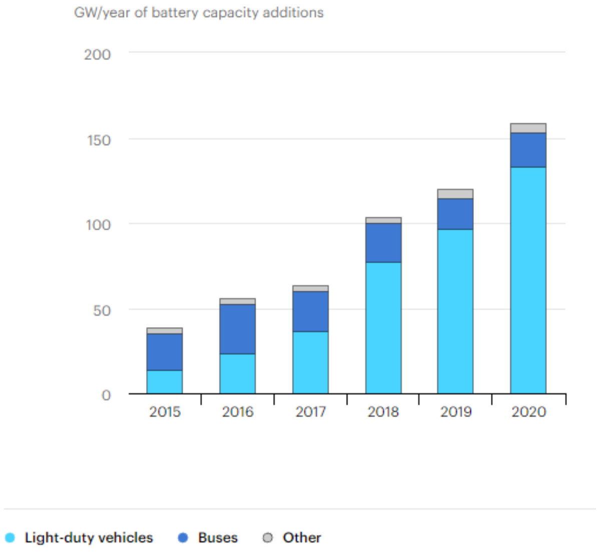

Figure 1: EV battery demand by mode, 2015-2020 [5].

Due to the presence of an electric motor, these vehicles emit less or no GHG into the atmosphere while in use, unlike internal combustion engine vehicles (ICEVs). For this reason, electric vehicles show great potential for reducing global greenhouse gas emissions, although the environmental impact of their production and the management of their end-of-life components, as well as the source of the electrical energy that powers them, are important factors to consider [2].

Electric vehicles can be divided into different categories, namely hybrid electric vehicles (HEV), plug-in hybrid electric vehicles (PHEV), and purely battery-driven electric vehicles (BEV) (Figure 2) [2].

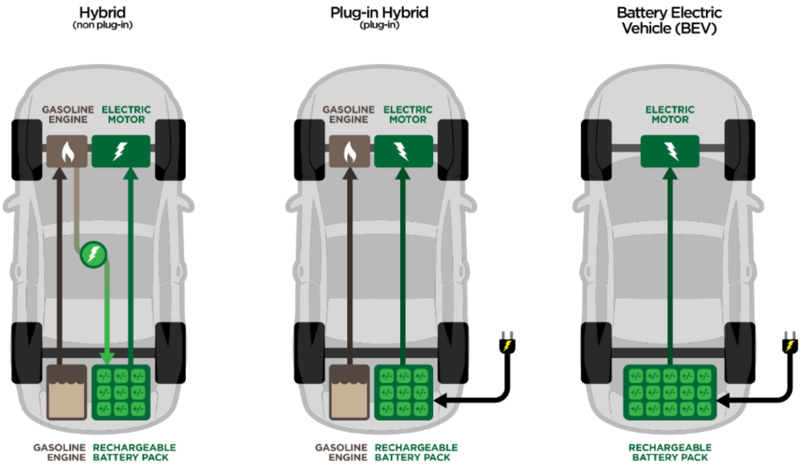

Figure 2: Types of electric vehicles.

1.1.1 Battery electric vehicles

BEVs do not have an internal combustion engine, they are equipped with an electric motor and run exclusively on electricity, i.e., the energy is obtained from the grid and stored in a high-capacity battery. Battery electric vehicles have a driving range that may go from about 200 to 600 km, depending on the capacity of the battery. The major advantage is that BEVs do not emit GHG while they are operating [6].

1.1.2 Hybrid electric vehicles

HEVs have a smaller internal combustion engine and an electric motor, and while the vehicle is being driven it switches easily between the combustion engine and the electric motor, usually using fuel at higher driving speed (highway driving) and electric power for lower driving speed (city driving). Hybrid electric vehicles cannot be charged from the grid, the energy stored in the battery comes from regenerative braking, meaning that some of the kinetic energy usually wasted to slow down the car can be stored, and from some energy produced by the engine during combustion, which is turned into electricity. The battery in HEVs is not as powerful as in BEVs, making them more dependent on fuel. The greatest advantages of HEVs are their high driving range and not needing to be charged, so they do not consume electricity from the grid [6].

1.1.3 Plug-in hybrid electric vehicles

PHEVs differ from HEVs in the sense that PHEVs can be charged from the grid, they have larger capacity batteries that could not be fully charged with regenerative braking alone, and these vehicles only use the combustion engine when the battery is fully discharged. Therefore, PHEVs are mostly driven by the electric motor, relying less on fuel, emitting less GHG than HEVs, and usually achieving larger driving ranges than purely BEVs [6].

Since electric vehicles require high voltage and current output, many individual electrochemical cells are needed in an EV battery. The individual cells are the basic units of a battery, and these are grouped in battery modules, which are then grouped to form the battery pack. The individual cells within a module and the modules comprising the battery pack are connected in series and/or in parallel in order to achieve the desired voltage and power requirements.

1.1.4 Battery Management System

While an EV battery is operating, a certain charge or discharge current is applied, which results in a voltage increase or decrease with consequent temperature variations. All these parameters (current, voltage and temperature) can be monitored and controlled by a Battery Management System (BMS), coupled to the cells. The functions of this device include monitoring, protecting and balancing the battery. Different parameters are measured continuously to ensure that they are within their acceptable levels, for example preventing overcharging or overdischarging of the cells and controlling the acceptable temperature range (Figure 3). To track these parameters, BMSs are composed of sensors, actuators and regulators [7–10].

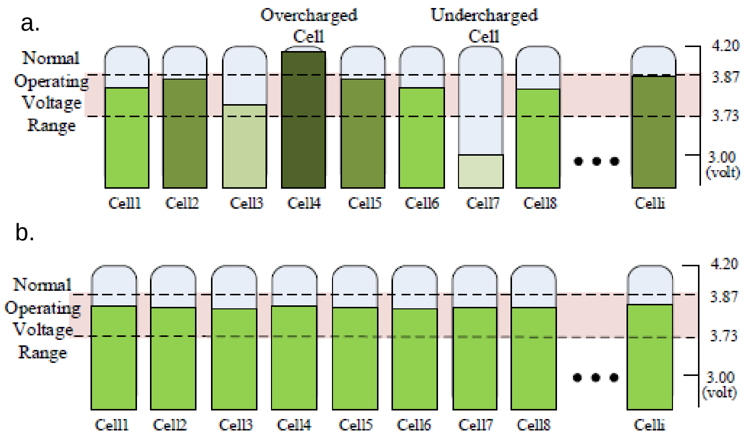

Figure 3: a. Without a BMS cells within a battery can have charge imbalance, with some overcharged or overdischarged cells; b. BMS ensures protection, constant monitoring and charge balance among all cells [11].

Monitoring becomes even more important because even in a set of identical cells with the same specifications there are differences between the cells, including differences in voltage, impedance, amount of electrical charge, self-discharge, capacity, and life cycle time. In addition, the failure of a single cell might compromise the performance of the entire battery, so it is important to constantly monitor the condition of the battery [3, 12].

BMS data acquired during the lifetime of an EV battery would be extremely helpful for its battery state estimation, however this access is usually protected by the manufacturer. Furthermore, depending on the data acquisition and battery state estimation model used on a BMS, the discrepancy between the calculated values and the real ones may be significant [13]. These issues highlight the importance of simple and accessible diagnostic techniques for electric vehicle batteries.

1.2 Problem definition

Despite the advances that have been made in the electric mobility sector, the useful lifetime of batteries used in electric vehicles, which are mostly of the lithium-ion type, is still a major limitation, since battery degradation sometimes leads to its unusability before the expected lifetime [14].

As a result of various ageing mechanisms that occur during the life cycle of a battery, it degrades over time, resulting in capacity and power fade. Understanding these ageing mechanisms is of utmost importance for battery state estimation and for developing longer-lasting batteries and establishing the most suitable operating conditions for them. Extending the life of a battery will result in delaying its replacement and thereby reducing the environmental impact related to the production of a new battery and the disposal of the end-of-life one [2].

An electric vehicle battery should be disposed of when it reaches 80% of its initial capacity or when its internal resistance doubles compared to the initial resistance [15, 16]. The challenge relies on simple, cost-effective, and fast monitoring and diagnosis of battery condition during and after its use in an electric vehicle, which allows not only to understand when it should be replaced, but also to decide according to its condition whether it still fits the requirements for a second life application, or whether it needs to be disposed of by separating and recycling its components.

For example, a capacity of 80% compared to the original is the indicator for replacement in electric vehicles, but, in some cases, it can be maintained for as low as 65% of the rated capacity. If the battery is able to be cycled 1000 times with a state-of-health (SOH) higher than 60%, it is considered suitable for industrial electric mobility applications, such as lift platforms or electric stackers. For lower SOH values the batteries can only be used for stationary storage applications. A SOH of 40% or lower indicates that the battery is no longer appropriate for second life use [8].

1.3 Objective and selected approach

So far, several indicators have been defined to characterize the state of a battery based on different parameters, such as capacity, resistance, and open circuit voltage. Among the established indicators, State-of-Health (SOH) shows to be extremely useful in the evaluation of lithium-ion batteries used in electric vehicles, since SOH assesses the condition of a battery compared to its initial state and quantitatively evaluates the battery’s remaining usable capacity. Thus, in this dissertation, SOH is the chosen parameter for battery state assessment.

The most common definition of SOH allows for evaluating the state of a battery based on its loss of capacity compared to the initial state. However, capacity measurement involves a complete charge and discharge, which is time and energy-consuming, especially if an analysis is performed on battery modules rather than individual cells. Given that resistance increase is critical for the performance of electric vehicle batteries, it should be evaluated and considered for battery state assessment.

The objective is to deeply understand the dynamics of cell ageing employing Electrochemical Impedance Spectroscopy (EIS) tests during cycling, to study the viability of impedance measurement for state-of-health (SOH) estimation and to assess whether there is a correlation between any of the parameters obtained by EIS and capacity.

For this, new and already used batteries are both subjected to charge-discharge cycles, thus obtaining capacity values through Coulomb counting. After each charge and discharge step, Electrochemical Impedance Spectroscopy is performed to obtain impedance values, allowing to analyze the variation of the cell’s resistance.

This work is organized according to the following structure:

- **Chapter 2: Literature Review.** Lithium-ion batteries, their operating principle, main advantages and characteristics are presented. The degradation mechanisms associated with lithium-ion battery ageing are addressed and, finally, battery state estimation is approached;

- **Chapter 3: Methodology.** The two testing techniques used in this work are discussed - charge-discharge cycles and Electrochemical Impedance Spectroscopy -, including their application to lithium-ion batteries;
- **Chapter 4: Experimental Part.** Describes the selected experimental procedure and conditions to perform the charge-discharge and EIS tests;
- **Chapter 5: Results and Discussion**;
- **Chapter 6: Conclusions** and future work.

2 Literature Review

2.1 Batteries

The first battery was created by Alessandro Volta in 1800, demonstrating that by using zinc as the negative electrode material and copper as the positive electrode material in an acidic electrolyte, an electric current is generated due to the decomposition of water and consequent hydrogen formation. Only a few decades later rechargeable batteries were developed, namely the lead-acid battery by Gaston Planté in 1859, the nickel-cadmium battery by Waldemar Jungner in 1899, and the nickel-iron battery by Thomas Edison in 1901 [1].

A battery consists of several cells, connected in series and/or in parallel to meet the needs of energy and power required for a particular application, even though the term “battery” is often used to designate a single cell [3, 8].

For applications that require high voltage, individual cells can be assembled in series, where the total potential is equal to the sum of the individual potentials of each cell:

$$E = \sum_{i=1}^{n} E_i \tag{1}$$

For applications that require high current, the cells are assembled in parallel, where the total current is equal to the sum of the currents of each cell:

$$I = \sum_{i=1}^{n} I_i \tag{2}$$

Electrochemical cells convert chemical energy into electric energy through redox reactions. When an oxidation reaction occurs at the anode, cations flow through the electrolyte from the anode to the cathode and anions flow from the cathode to the anode, while the electrons flow to the cathode through an external electric circuit, providing electrical energy.

Cells can be classified as primary or secondary, depending on the reversibility of the chemical system.

2.1.1 Primary Batteries

Primary batteries, such as lithium, alkaline-manganese and zinc-carbon batteries cannot be recharged, their stored chemical energy is released when the battery is being used, and when there are no more electrons to flow from the anode to the cathode, the battery is considered dead. With these batteries it is possible to obtain high specific energies that can be stored for a long time [3].

2.1.2 Secondary Batteries

On the other hand, secondary cells, like lead-acid, nickel-cadmium, or lithium-ion batteries, can be recharged hundreds or thousands of times, having a long life cycle. In this case, when the battery is discharging, i.e., providing energy, cations flow from the anode to the cathode and anions flow in the opposite direction, through the electrolyte and separator, and the electrons flow in the same direction through the external electric circuit. When the battery is charging, the reverse process occurs, the cations and the electrons flow from the cathode to the anode, through the separator and the electric circuit, respectively [3].

Lithium-ion batteries (LIBs) have been widely used for many applications, such as in mobile phones, laptops, medical devices, power tools, energy storage systems and electric vehicles. Their high energy density and power output make them the preferred option as traction batteries in electric vehicles (BEVs) and plug-in hybrids (PHEVs) [1, 2].

Some of the characteristics that make lithium-ion batteries so attractive for energy storage applications are lithium's small ionic radius, which facilitates its diffusion, and its low molecular weight that allows for lighter-weight batteries and devices. Additionally, lithium is the metal with the lowest reduction potential value ($E°(Li^+/Li) = -3.04V$ vs standard hydrogen electrode), which allows it to generate higher potentials, resulting in a higher energy density. Therefore, it is possible to have smaller and lighter cells than the other types of secondary batteries [1]. Furthermore, LIBs have a long shelf life and do not present memory effect, meaning that incomplete discharges will not cause capacity reduction [12, 17, 18].

These batteries outperform other types of secondary batteries, such as lead-acid and nickel-metal hydride batteries in terms of specific energy (can reach up to 450Wh/kg in the case of $LiCoO_2$/graphite cells), and lifetime (lasting over 20000 cycles in $Li_4Ti_5O_{12}$ negative electrode cells) (Table 1) [19, 20]. Additionally, Li-ion batteries can reach power density values up to 3000W/kg in the case of $LiFePO_4$ (LFP)/graphite cells (Figure 4) [13].

Table 1: Properties of commercially available secondary batteries [11 ,20, 21].

Battery type	Nominal cell voltage (V)	Specific energy (Wh/kg)	Power density (W/kg)	Cycle life (up to 80% initial capacity)
Lead-acid	2	30-50	180	200-350
Ni-Cd	1.25	45-80	150	1500
Ni-MH	1.25	60-120	250-1000	300-500
Li-ion	3.6	110-180	1800	500-1000

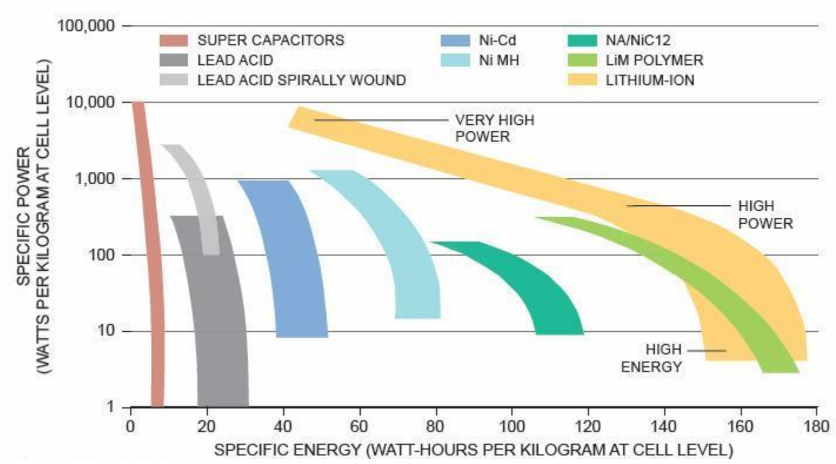

Figure 4: Specific Power (W/kg) and Specific Energy (Wh/kg) of different types of secondary cells [22].

2.1.2.1 Lithium-ion batteries

A lithium-ion cell includes a negative electrode, a positive electrode, a separator, an electrolyte, and current collectors (Figure 5) [23]. The separator is a porous polyolefin membrane embedded in a mixture of organic solvents with a lithium salt, permeable to lithium-ion transfer. This membrane prevents the passage of electrons, ensuring that there is no electronic contact between the positive and negative electrodes through the electrolyte [24]. Binders are used to adhere the electrodes to their respective current collectors, which are copper foil for the anode and aluminum foil for the cathode. The battery has a protective metal casing, and it may have a plastic covering and an electronic control unit [25].

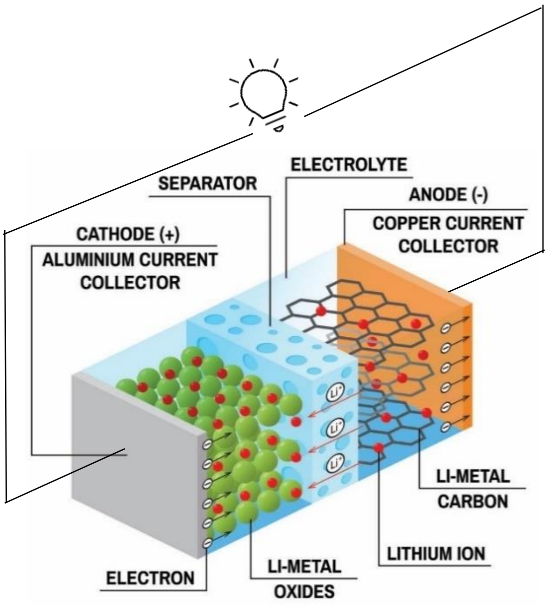

Figure 5: Structure of a lithium-ion battery [26].

Lithium-ion batteries have three main formats: cylindrical, prismatic and pouch (Figure 6).

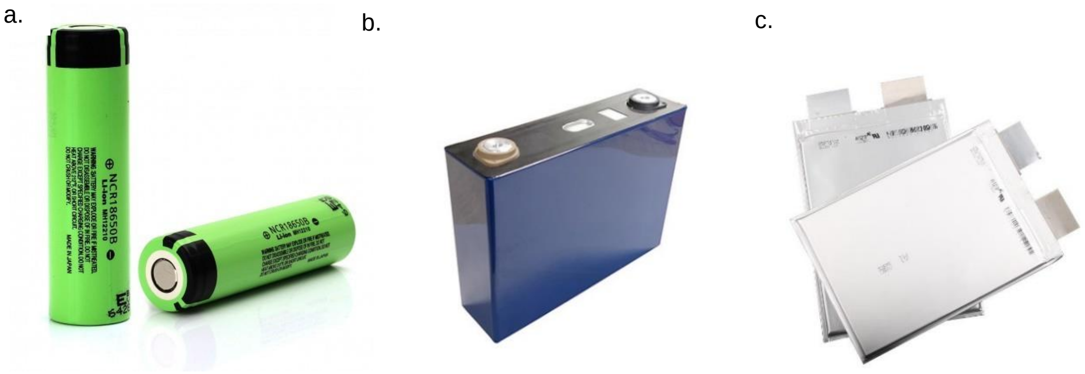

Figure 6: a. Cylindrical; b. prismatic; and c. pouch Li-ion cells.

It is important to mention that although the negative electrode is designated as the anode and the positive electrode as the cathode, this is only true during the discharge process, i.e., when the battery is delivering power. During the charging process, the electrodes change their role as anode and cathode. Throughout this dissertation, the designation corresponding to the discharge process is the one used, for reasons of simplicity [24].

There are different types of lithium-ion batteries that differ essentially in the composition of the positive electrode. The cathode materials are transition metal oxides such as $LiCoO_2$ (LCO), $LiMnO_2$, $Li_4Ti_5O_{12}$ (LTO), $LiTiS_2$ (LTS), $LiNi_{0.80}Co_{0.15}Al_{0.05}O_2$ (NCA or NCR), $LiMn_2O_4$ (LMO), $LiFePO_4$ (LFP) and $Li(Ni_xCo_yMn_z)O_2$ (NMC), where x, y and z represent different ratios. For the anode, lithium-titanate ($Li_4Ti_5O_{12}$) or different forms of carbon compounds may be used, such as hard carbon, graphite, or meso-carbon microbead (MCBM), graphite being the most widely used material [1–3, 6, 24, 27].

Electrodes use porous materials to achieve a high active surface area between the electrode and the electrolyte, thereby increasing the number of lithium-ion intercalation sites and increasing the number of available voids, which can accommodate volumetric changes during cycling [1, 3, 18].

When a LIB is charging (Figure 7), the lithium-ions flow from the cathode ($LiTMO_2$) and are intercalated in the anode and, at the same time, the electrons are attracted to the current collector and move from the cathode to the anode through the external current circuit, to ensure charge balance. At the anode, the lithium ions are accommodated in the graphite structure (LiC_6) [1, 3, 18, 24, 28].

During the discharge of the battery, the process is the opposite: the lithium is oxidized to Li^+ at the anode and Li-ions migrate to the cathode through the separator, being reduced to Li at the cathode and intercalated in the cathode structure. The movement of lithium ions from the anode to the cathode forces the electrons to flow through the electric circuit, generating the electric current that powers a device [3].

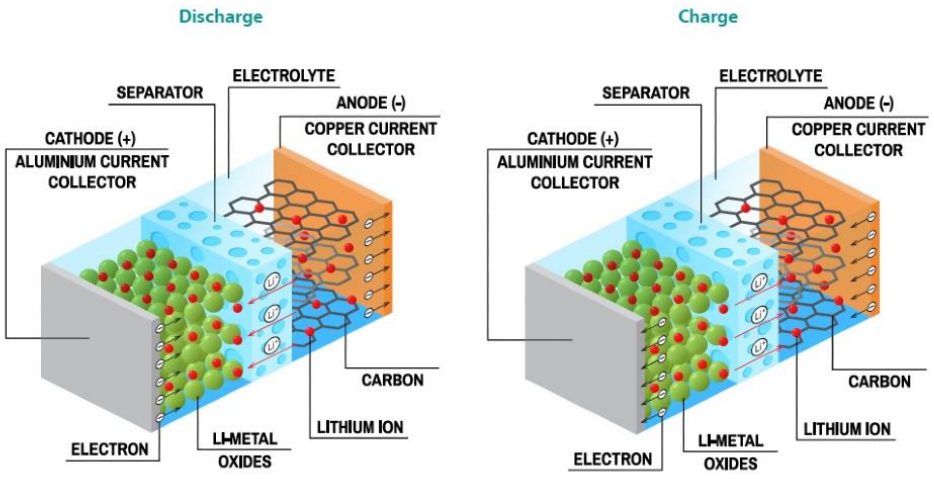

Figure 7: Ion and electron flow during discharging and charging in lithium-ion batteries [26].

The reactions occurring at the anode and at the cathode are the following:

$$Anode: xLi^+ + xe^- + C_6 \rightleftharpoons Li_xC_6 \tag{3}$$

$$Cathode: LiTMO_2 \rightleftharpoons xLi^+ + xe^- + Li_{1-x}TMO_2 \tag{4}$$

And the overall reaction that occurs during charge and discharge is as follows: [24]

$$LiTMO_2 + x\,C_6 \rightleftharpoons Li_{1-x}TMO_2 + x\,LiC_6 \tag{5}$$

, where the direct reactions are charge reactions and *TM* represents a transition metal.

During the first cycles of a battery, a passivation layer forms between the anode and the electrolyte, composed of particles of different sizes and chemical compositions, resulting from reduction reactions products, including the reduction of the electrolyte. This layer is designated Solid Electrolyte Interphase (SEI).

The most used electrolytes in commercial LIBs have a reduction potential of about 1.0V vs. Li^+/Li, this being higher than the reduction potential of lithium in graphite (between 0 ~ 0.25V vs. Li^+/Li), so the electrolyte tends to decompose on the anode surface, forming the SEI. The formation of the SEI is extremely important as it prevents electron tunneling, i.e., electrons are not capable to cross that physical barrier and be in direct contact with the electrolyte, therefore they will not take part in any parasitic reactions. Furthermore, the SEI reduces the kinetics of decomposition of the electrolyte and decreases the active lithium consumption from the lithiated graphite [16, 29–32].

Although it is possible to achieve quite positive results with some types of lithium-ion batteries, they are all subject to complex and irreversible physical and chemical degradation processes that eventually impair their performance [33]. Several factors can result in their rapid ageing and, consequently, in the need for the replacement of the degraded battery with a new one.

2.2 Ageing Mechanisms

2.2.1 Degradation Modes

Batteries can undergo calendar ageing (when no current is being applied) or cycling ageing (when a non-zero current is applied), modes that represent, respectively, the periods when the car is stopped and when it is being driven or charged [31].

There are several interdependent mechanisms involved in the ageing of lithium-ion batteries (Figure 8), and these are, according to Pastor Fernández et al. [8] divided into three Degradation Modes (DMs): conductivity loss (CL), loss of active material (LAM), and loss of lithium inventory (LLI).

Conductivity loss is related to the degradation of the electronic parts of the battery, which affects the battery's internal resistance, and includes corrosion of current collectors and binder decomposition. Loss of active material is related to structural transformations in the active material, including particle cracking, electrolyte oxidation, electrode decomposition, and crystal structure disorder. LLI is related to the decline in the number of lithium ions available for intercalation and deintercalation reactions by being consumed in parasitic and decomposition reactions, including SEI growth and decomposition, electrolyte decomposition, and lithium plating [8, 9, 13].

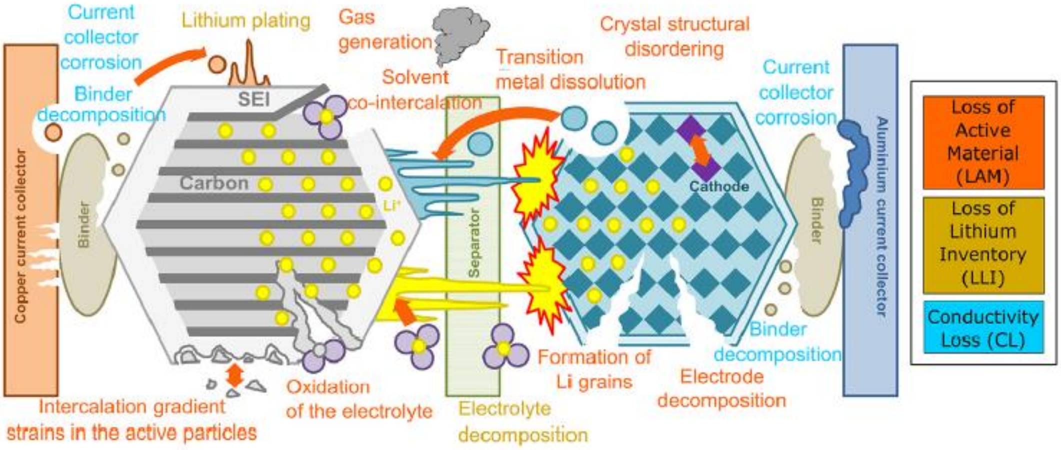

Figure 8: Ageing mechanisms of lithium-ion batteries and their respective degradation modes [8].

The ageing of lithium-ion batteries might be caused by both intrinsic and extrinsic factors. Defects related to the production methods and the materials used in the fabrication of the batteries are examples of intrinsic factors that can affect ageing. Extrinsic factors are related to the operating conditions applied to the battery, such as temperature, charge and discharge rates, depth of discharge (DOD), and state-of-charge (SOC), which may result in faster or slower ageing [9]. In addition to the influence that each of these factors has on the ageing of a single cell, it is also common for the battery to be subjected to inhomogeneous conditions, such as having cells operating at different temperatures and non-uniformly distributed currents (due to the intrinsic differences between the cells) [3, 8, 13, 16, 34].

- **Temperature**

Within an acceptable temperature range for proper battery operation, higher temperatures enhance ion mobility, which reduces the overpotential and internal resistance of the cell. This allows the cell to charge and discharge more energy until the cut-off potential is reached, increasing battery capacity. In contrast, lower temperatures decrease ion mobility, and, additionally, the electrolyte becomes more viscous, decreasing ion transfer and battery capacity [13].

However, operating a battery at too high temperatures tends to result in faster ageing, causing decomposition of the cathode and electrolyte, increased SEI growth at the anode, and even decomposition of the binder [6]. As a consequence, the internal resistance increases, and the battery capacity decreases [16, 29].

In addition, high temperatures can lead to gas formation, increasing the internal pressure of the battery. This may correspond to the formation of CO_2 by the reaction between the electrolyte and the films on the cathode surface, which is mainly promoted by high SOC, corresponding to a lithium-depleted cathode. Gas could also be formed by the decomposition of the electrolyte and the SEI. Due to the decomposition of the SEI, the lithiated graphite may come in contact with the electrolyte, promoting undesirable exothermic reactions that further increase the temperature in the cell [29, 35].

If the temperature is too low, lithium metal deposition (lithium plating) can occur on the anode surface. This deposition may be heterogeneous, forming lithium dendrites that, when growing and crossing the separator, result in a short circuit of the battery. Furthermore, the capacity declines due to higher overpotentials since the battery reaches its cut-off potential much faster [24, 29].

- **Current**

Fast charging usually involves high currents and high temperatures, which accelerate ageing. Thus, most lithium-ion cells are severely affected by high currents in two main ways:

1) charging at high current rates can lead to lithium plating on the anode surface, especially at high SOC or combined with low temperatures, and dendrite formation. Additionally, the deposited lithium might react with the electrolyte, resulting in LLI and increasing the impedance [36].
2) there can be unstable SEI growth and localized exothermic decomposition of the electrolyte, which reacts undesirably with some of the electrode’s active material. [6, 13, 24, 29, 35, 36].

- **SOC and DOD**

State-of-Charge corresponds to the percentage of the charge stored in a battery at a certain moment, compared to the rated charge it is able to store (rated capacity). Therefore, SOC varies when the battery is charging or discharging, and due to ageing, the maximum SOC that can be achieved decreases over time.

Depth of Discharge is the percentage of released charge during discharge, compared to the rated capacity. If a battery is totally discharged, a DOD of 100% was applied.

Overcharging the battery, i.e., exceeding the battery's maximum potential, or in some cases even just charging the battery up to SOC > 95%, enhances decomposition of the electrolyte, the binder, and the cathode. Solvent co-intercalation and SEI growth occur, as well as gas generation, and consequent crack formation in the anode. [3, 6, 8].

A high DOD may result in volume changes and mechanical stresses with consequent particle cracking and loss of contact between the active material particles and SEI growth. If the discharge is carried out to a potential lower than the minimum battery potential, corrosion of the current collectors and binder, and disorganization of the crystalline structure of the cathode can occur [13, 35].

Thus, overcharging, overdischarging and high DODs lead to a loss of cell capacity and should be avoided [3].

A summary of the influence of the extrinsic factors on the ageing of a cell and the associated degradation modes is presented in Table 2.

Table 2: Influence of extrinsic factors on the ageing mechanisms of a LIB and associated degradation modes [8, 35].

Extrinsic Factor		Ageing Mechanism	Predominant DM
Temperature	High (>35°C)	● Electrolyte decomposition and SEI growth ● Transition metal dissolution ● Gas generation	LLI LAM LAM
	Low (<5°C)	● Lithium plating on the anode and dendrite formation ● Electrolyte decomposition by the metallic lithium	LLI LLI
Charge-discharge rate (C-rate)	> 2C	Changes in the porosity of the anode due to volume changes, gas generation and SEI growth	LLI, LAM
SoC	> 95%	● Electrolyte decomposition ● Binder decomposition ● Co-intercalation of the solvent, gas generation and consequent crack formation on the anode	LAM CL LAM
	< 0%	● Current collectors corrosion ● Disorganization of the cathode's crystalline structure ● Binder corrosion	CL LAM CL
DoD	> 70%	Loss of contact between particles of the active material due to volume changes	LAM

It is important to note that the ageing behavior of the cells, as well as the influence that each extrinsic factor plays in this process, depends on the composition of the cells.

As a result of these different ageing processes, the internal resistance of the battery increases (power fade), and the capacity (the total electrical charge that a battery is able to store) decreases (capacity fade) compared to the values at the beginning of its lifetime, which in the case of electric vehicles translates into a reduction of the driving range and power of the vehicle, respectively [3, 8, 12, 16].

Capacity loss of LIBs is mostly attributed to the formation and growth of the SEI. The SEI grows as the battery ages, and the thicker the layer, the greater the resistance of the battery. During cycling, the battery undergoes volume expansion and contraction, creating mechanical stresses that result in small fractures in the SEI and even on the electrodes, and loss of electrical contact [31]. The fractured zone of the graphite is then exposed to the electrolyte, which leads to SEI formation in that zone. Thus, it is important to consider that the lithium initially available for intercalation and de-intercalation processes is consumed in the initial formation of SEI (during the first cycles) and its growth and later in the formation and growth of SEI on the surface of fractures that arise as the number of cycles increases [33, 37, 38].

Lithium-ion batteries are characterized by three main stages of degradation:

(i) rapid decline of the capacity associated with initial SEI formation;
(ii) approximately linear ageing in terms of capacity associated with lithium consumption in secondary reactions;
(iii) rapid decrease in capacity as the cell approaches the end of its life until it eventually fails, associated with an impedance rise [27, 36, 39].

As degradation occurs, capacity decreases and impedance increases until they reach a critical value for electric vehicle applications: batteries should be replaced when they reach 80% of their initial capacity or when the internal resistance of the cell increases 100% compared to the rated internal resistance [1, 13, 15, 40].

Thus, it becomes essential to evaluate batteries' condition, by means of battery state parameters, in order to identify when they should be replaced, and if they can later be reused in a second-life application, depending on their condition. In this way, more efficient and sustainable management of end-of-life lithium-ion batteries is ensured [1].

2.3 Battery State Estimation

Some important parameters to consider regarding batteries, such as temperature, capacity, open circuit potential and impedance can be obtained experimentally through different techniques. These parameters change in real-time, so their measurement is crucial for effective battery monitoring and management [15].

Regarding EV batteries, the capacity and internal resistance are extremely important parameters for battery condition assessment, since these are what the replacement criteria are based on.

Independently of the chosen measurement method, the experimentally obtained parameters can then be translated into battery state indicators, such as State-of-Charge (SOC), State-of-Energy (SOE), State-of-Power (SOP), State-of-Temperature (SOT), State-of-Safety (SOS), and State-of-Health (SOH) [13].

2.3.1 Battery State Indicators

2.3.1.1 State-of-Charge

The State-of-Charge represents the available capacity, Q_a, as a percentage of the nominal battery capacity, Q_n, i.e., it indicates the amount of charge present in a cell relative to the maximum charge that can be stored. It can be calculated by the coulomb counting method, which reads the integration of the charge or discharge current during the period of operation [7, 13, 15].

This indicator can be calculated using the following expression:

$$SOC(t) = SOC(t_0) + \int_{t_0}^{t} \frac{I(t)\eta}{Q_n} dt \tag{6}$$

, where SOC(t) e SOC(t_0) are the SOC values at time t and the initial time t_0, respectively, and η is the coulombic efficiency, which represents the ratio between the energy released in a total discharge and the energy stored during charging that is required to recover the original capacity [15].

Thus, the SOC of a battery increases during the charge process and decreases during discharge. As battery ageing occurs, the amount of lithium available declines (LLI), resulting in a decrease in the amount of charge that can be stored while charging, which translates into a gradual reduction in the maximum SOC that can be obtained.

2.3.1.2 State-of-Energy

During discharge, the potential decreases rapidly at both the beginning and the end of the process, with a slower reduction in between, which means that at different SOCs, the release of the same amount of charge does not equal the same amount of released energy. Furthermore, the energy released depends on the current applied, since high currents lead to higher energy losses. Thus, the SOC only gives an indication of the available capacity (Ah), but not the available energy (Wh) [15].

State-of-Energy can then be defined as follows:

$$SOE(t) = SOE(t_0) + \int_{t_0}^{t} \frac{P(t)}{E_n} dt \tag{7}$$

, where SOE(t) and SOE(t_0) correspond to the State-of-Energy at the moments t and t_0, respectively, P(t) corresponds to the power at time t and E_n represents the nominal power value of the battery.

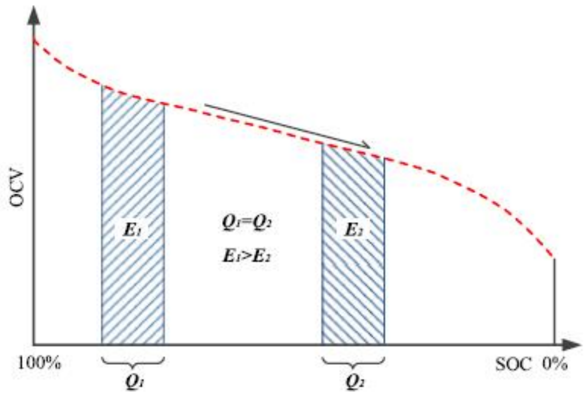

Figure 9: The same charge throughput at different SOC corresponds to a different amount of released energy.

2.3.1.3 State-of-Power

This parameter represents the power that the battery is able to deliver or gain during a given time interval, assuming a positive power value in the discharge step and a negative one in the charge step. The State-of-Power for charge and discharge can be obtained, respectively, by the following expressions:

$$SOP^{charge}(t) = \max\ [P_{min}, V(t+\Delta t)I_{min}^{charge}\ ] \tag{8}$$

$$SOP^{discharge}(t) = \min\ [P_{max}, V(t+\Delta t)I_{max}^{discharge}\ ] \tag{9}$$

, where P_{min} and P_{max} are the lower and upper limits of battery power, respectively, Δt is the time interval of the charge or discharge, V (t+Δt) is the value of the potential at time t+Δt, and I_{min}^{charge} and $I_{max}^{discharge}$ are the minimum and maximum continuous currents, respectively, applied during that time interval [15].

2.3.1.4 State-of-Temperature

Temperature has a major influence on the degradation mechanisms of a battery and is therefore an important parameter to take into consideration. The determination of the SOT is a rather complex process, based on thermodynamic models, which evaluate the internal temperature of the cell and the temperature distribution [15].

2.3.1.5 State-of-Safety

State-of-Safety evaluates the dangerousness of the battery, classifying it in different levels, and allows defining the conditions of voltage, temperature, and current that are safe for the battery to operate [15].

2.3.1.5 State-of-Health

The State-of-Health (SOH) of a battery is an indicator that quantitatively assesses the state of the battery compared to its initial state [7]. Different parameters may be used to calculate the SOH of a battery as long as they show a significant change over time, with the most common calculations being based on capacity (capacity fade), which is directly related to the driving range of a vehicle. This estimation evaluates the battery's condition in terms of storage and release of electrical energy [8, 13].

The SOH of a battery in terms of capacity can be calculated as follows:

$$SOH = \frac{C_a}{C_r} \times 100\% \tag{10}$$

, where C_a and C_r represent the actual and rated capacity values, respectively [15].

This indicates that a battery is expected to have a SOH of 100% right after manufacturing, decreasing over time, but this is not necessarily true, as a battery may have a slightly lower or higher capacity than the rated capacity right after it is manufactured [7].

The definition of SOH based on capacity is not consensual among authors. For example, in the definition proposed by Hu et al. [15], a SOH of 0% is reached only when the battery's capacity C_a equals zero. According to this definition, a battery should be replaced at a SOH of 80%. On the other hand, authors such as Ungurean et al. [41] defend that the moment when the battery is replaced, i.e., when the capacity reaches 80%, corresponds to a SOH of 0%.

In this work, SOH based on capacity is defined as in equation 10, assuming battery replacement at a SOH of 80%.

Another alternative is to define SOH based on the battery's internal resistance since this is an important parameter to evaluate battery performance. Thus, resistance-based SOH can be defined as:

$$SOH = \frac{R_{int,subs} - R_{int}}{R_{int,subs} - R_{int,NEW}} \times 100\% \tag{11}$$

, $R_{int,subs}$ being the internal resistance when the battery is substituted, R_{int} is the current internal resistance and $R_{int,NEW}$ is the internal resistance of the battery when it is new [41].

However, the definition of SOH based on resistance is also not as straightforward. First, because at the moment when a battery is replaced, the SOH would be 80% for the capacity-based SOH definition, while it would be 0% using the resistance-based SOH definition. Furthermore, the rated internal resistance value is not always readily available for all cell models.

These concepts are further investigated in the experimental part of this work, as well as a possible correlation between the capacity-based and resistance-based SOH definitions.

3 | Methodology

Multiple techniques can be employed to test capacity and resistance of lithium-ion cells. For this study in particular, where it is important to fully understand the processes occurring in a cell as it ages, Electrochemical Impedance Spectroscopy is the selected technique, as not only it provides important information on the electrochemical dynamics of a cell, but it is also the only technique where the different contributions to the total impedance can be separately identified, allowing analyzing the resistive component of impedance. EIS can be combined with cycling tests, where the capacity is measured, by being performed at different charge states, after a charge or discharge step.

3.1 Charge-discharge cycles

Cycling tests can be performed to track the loss of capacity of a cell (capacity fade) over time, which corresponds to a decrease in the maximum energy stored by the battery due to ageing mechanisms. These tests are easily repeatable and allow an accurate calculation of capacity [13, 42].

The measurement of cell capacity is done during a full charge or discharge: the current is integrated as a function of time and recorded in Ah by Coulomb counting. The measured capacity can be affected by the charge-discharge profile, which is related to the applied current, and the cell temperature [13].

Lithium-ion batteries are typically charged using the Constant Current - Constant Voltage (CC-CV) mode. A constant current specified by the manufacturer is initially applied and the battery’s potential gradually increases. During this phase, the lithium ions and electrons flow from the cathode to the anode, until the battery reaches its specified maximum voltage. At this point, the constant potential mode begins, holding the battery at its maximum potential while the current lowers until it reaches its cut-off value (usually less than 10% of the constant current value). During this step the battery is still storing charge, which ensures that a higher SOC is achieved [3, 7, 13].

Discharge is usually done by applying a constant current, specified by the manufacturer. A full discharge ends when the battery reaches its specified minimum voltage, and at this point, the SOC of the battery is expected to be 0%.

The main disadvantage of cycling tests is their duration. The charge and discharge currents specified by the manufacturer cannot be too high to avoid high overpotentials and excessive ageing, therefore the testing time is long. Furthermore, the Constant Voltage mode during charging takes longer than the Constant Current mode, meaning that even after reaching the maximum potential, the battery continues charging as the current slowly decreases for an even longer timeframe.

A single cell needs about 1 hour to fully discharge and more than 1 hour to fully charge (CC-CV mode) using a 1C-rate. Then, in the viewpoint of electric vehicle batteries, if capacity testing is performed to a stack of cells connected in series and/or in parallel, the total testing time increases substantially, demanding that the vehicle cannot be used for several hours.

3.1.1 C-rates

The rate at which a battery is charged or discharged is referred to as C-rate, and this concept relates the selected charge or discharge current with the cell's capacity. For example, using a 1C-rate means that the current (in A) used in the process is equal to 1x the rated capacity of the battery (in Ah), meaning that it will be fully charged/discharged in one hour. Similarly, a rate of 0.5C is half that current value, which means that the battery will take two times longer to charge or discharge. As an example, a 1C-rate of a 3Ah capacity battery corresponds to charging or discharging the battery with a 3A current, in 1 hour [13].

Lower currents result in slower charges and discharges and the overpotential is lower, thus it is possible to store and release, respectively, more charge than if higher C-rates are used. Lower C-rates (1C or lower) are more useful to study the thermodynamic capacity loss by LAM and LLI. Moreover, lower currents facilitate the accuracy of EIS tests due to the lower overpotentials, so the rest time before the EIS is more likely to be sufficient for voltage stabilization [13]. However, the lower the C-rate, the longer the duration of the tests, which is the main disadvantage.

On the other hand, higher C-rates result in faster testing and there is a stronger resistive effect, which makes them more suitable for the study of the kinetics of the cell [3]. However, high discharge currents lead to a higher overpotential, resulting in lower and more imprecise capacity values [13].

C-rates should be carefully chosen to better fit the purpose of the study, and the effect of too high or too low currents on the ageing of the battery should be taken into account. If possible, the C-rates specified by the manufacturer should be used.

Figure 10 shows how the discharge current affects the discharge capacity, as well as the initial voltage drop.

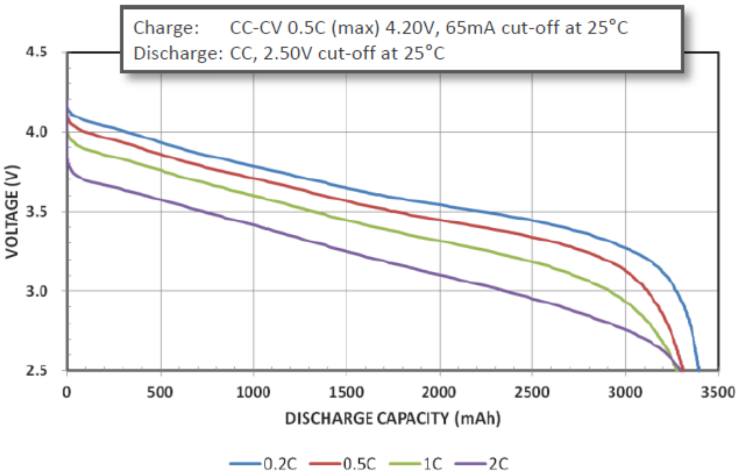

Figure 10: Influence of discharge current on discharge profile and discharge capacity [43].

Figure 11 shows the typical potential and current charge and discharge curves of a battery.

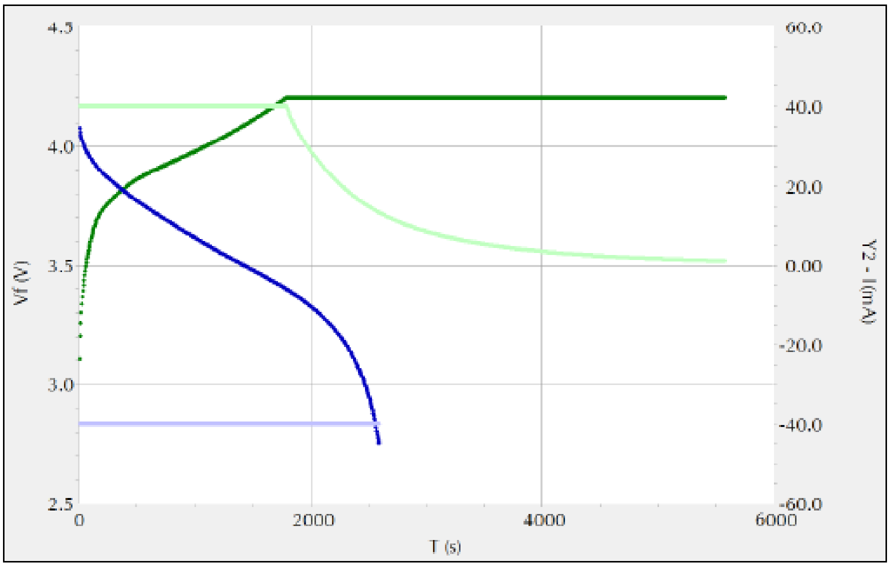

Figure 11: Typical potential charge (dark green) and discharge (dark blue) profiles and charge (light green) and discharge (light green) current curves of a Li-ion battery [3].

Figure 12 is an example of a healthy behavior of the evolution of a battery's capacity during cycling, in percentage and Ah, as a function of the number of cycles. During cycling, the capacity was calculated in each full charge and full discharge.

This allows calculating Coulombic Efficiency (the ratio between the energy released in a total discharge and the energy stored during charging that is required to recover the original capacity) over cycling. The higher the Coulombic efficiency, the less capacity is lost during a charge/discharge cycle, which translates in a longer life cycle. Capacity decreases with the number of cycles but this evolution is not linear [3].

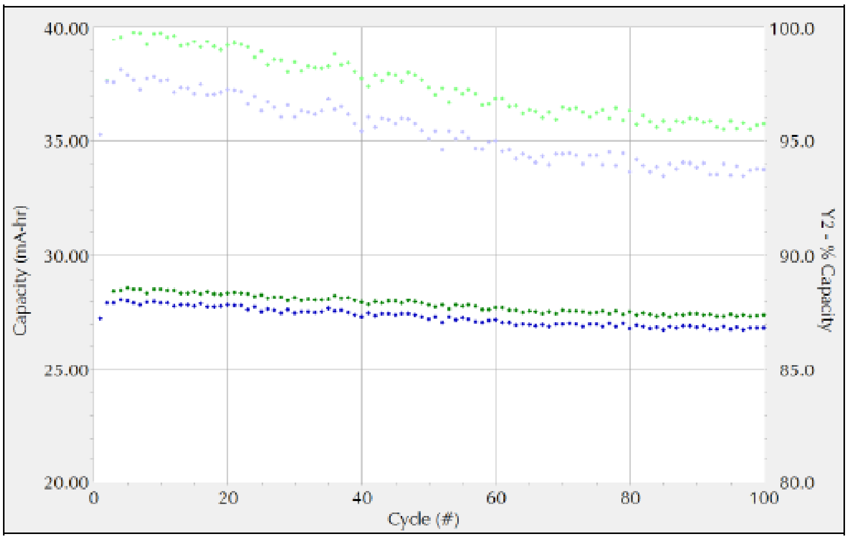

Figure 12: Capacity evolution of a battery with cycling, in Ampere hour (darker points) and percentage (lighter points), calculated during charging (green) and discharging (blue) [3].

3.2 Electrochemical Impedance Spectroscopy

Impedance is defined as the opposition of an electrochemical system to electric current flow [23, 44].

Electrochemical Impedance Spectroscopy is a non-destructive technique, so the physical and chemical properties of the component being studied are maintained, and it is possible to apply it to all the different types of cells. EIS allows studying the kinetic and mechanistic processes occurring in an electrochemical system, providing important information about its mechanisms in a single test. In an infinite frequency range, EIS tests obtain information about all the processes taking place in an electrochemical cell, which can be happening at very different rates [8, 12, 45–47]. In addition, this technique is highly sensitive to degradation effects that occur in batteries, allowing them to be identified and their variation to be studied. EIS tests are much faster than capacity tests, so SOH determination based on impedance is of highest interest [23, 29].

Impedance may be measured by applying a low-amplitude sinusoidal potential signal to an electrochemical cell and measuring the resulting sinusoidal current signal (potentiostatic measurement), or by applying a current signal to the electrochemical cell and measuring the potential (galvanostatic measurement). This signal is applied so that the subsequent response is, in a linear or pseudo-linear system, phase-shifted by an angle ϕ but with the same frequency (ω) as the excitation signal, as described by the following equations of the potential perturbation and the consequent current response, respectively [44, 48]:

$$V(t) = V_0 \, sen \, (\omega t) \tag{12}$$

, where V_0 is the amplitude and

$$\omega = 2\pi f \tag{13}$$

is the angular frequency of the applied signal in radians per second

$$I(t) = I_0 \, sen \, (\omega t + \phi) \tag{14}$$

, where I_0 is the amplitude and ϕ is the phase angle between the two signals [47].

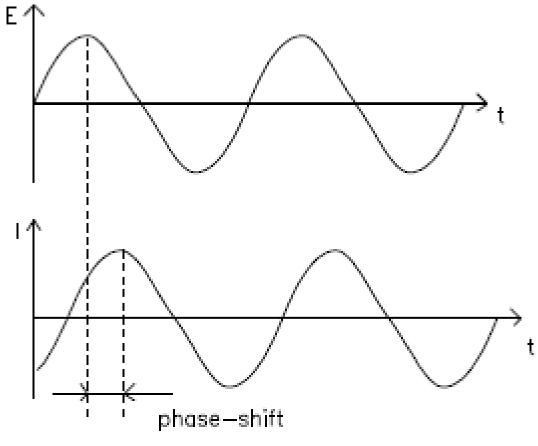

Figure 13: The applied voltage signal and the current response are shifted in phase [44].

By plotting the voltage signal on the X-axis and the current signal on the Y-axis, their overlay results in an oval shape, designated as a Lissajous Figure (Figure 14).

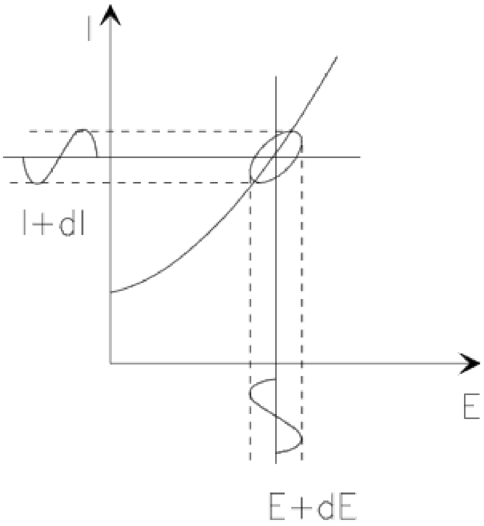

Figure 14: Lissajous Figure [41].

According to Ohm's law, the impedance Z(t) can be expressed as [23, 47]:

$$Z(t) = \frac{V(t)}{I(t)} = \frac{V_0\, sen\,(\omega t)}{I_0\, sen\,(\omega t + \phi)} = \frac{V_0}{I_0} sen(-\phi) \tag{15}$$

According to Euler's formula [44]:

$$e^{j\phi} = cos\phi + j\; sen\phi \tag{16}$$

Therefore, it is possible to express the potential and current signals as follows:

$$V(t) = V_0\, e^{j\omega t} \tag{17}$$

$$I(t) = I_0\, e^{j(\omega t - \phi)} \tag{18}$$

Thus, considering a phase angle $\theta = \omega t - (\omega t + \phi) = -\phi$, impedance can be represented by a complex number:

$$Z(t) = \frac{V(t)}{I(t)} = Z_0\, e^{j\theta} = Z_0\, (cos\theta + j\; sen\theta) \tag{19}$$

3.2.1 Nyquist diagram

By plotting the real part of Z(t), represented as Z', Re(Z) or Z_{real}, on the abscissa (X-axis) and the imaginary part, represented as Z'', Im(Z) or Z_{imag}, on the ordinate (Y-axis) of a Cartesian coordinate system with the Y-axis reversed, a Nyquist Diagram is obtained, where each point is obtained at a given frequency. In general, the leftmost region of the diagram corresponds to high frequencies, while the region on the right corresponds to low frequencies.

The impedance can also be represented as a vector [47]:

$$\vec{Z} = \frac{\vec{V}}{\vec{I}} \tag{20}$$

, where the length of $\vec{Z}$ corresponds to the modulus of the impedance

$$|\vec{Z}| = \frac{|\vec{V}|}{|\vec{I}|} \tag{21}$$

$$|\vec{Z}| = \sqrt{Z_{real}^2 + Z_{imag}^2} \tag{22}$$

, and the angle with the X-axis is

$$\arg(Z) = \theta = \omega t - (\omega t + \phi) = -\phi \tag{23}$$

$$\tan\theta = \frac{Z_{imag}}{Z_{real}} \tag{24}$$

A representation of |Z| as a vector in a Nyquist diagram is shown in Figure 15 [13, 44]:

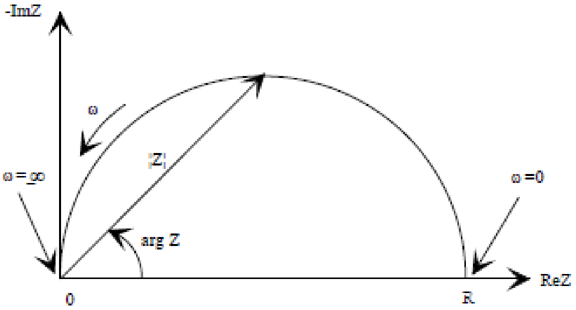

Figure 15: Representation of |Z| as a vector in a Nyquist plot [44].

3.2.2 Bode diagram

Another possibility to represent the impedance is through a Bode diagram (Figure 16). By plotting the logarithm of the frequency on the X-axis and the impedance modulus and phase angle on the Y-axis, a Bode diagram is obtained [44].

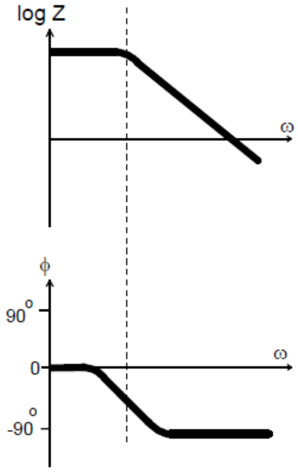

Figure 16: Representation of a Bode diagram [44].

3.2.3 EIS applied to batteries

Resistance testing becomes useful to obtain information about the dynamics of a cell, allowing to quantify its ageing in terms of power fade, which is related to an increase in internal resistance. Electrochemical Impedance Spectroscopy with subsequent Electrical Equivalent Circuit analysis allows not only to measure the internal resistance of the cell, but also to obtain more in-depth information on the cell’s dynamics and degradation mechanisms [9].

When applied to batteries, the impedance is measured at a steady state of charge, usually after a rest period to allow the battery to stabilize, reaching its equilibrium potential, and to provide accurate results. Therefore, the reproducibility of EIS tests is highly dependent on the prior rest period [49]. Impedance values are usually measured over a frequency range between 100 kHz and 10 mHz [23, 48].

For the study of battery impedance, obtained by EIS, the analysis of Nyquist diagrams is extremely useful, because these diagrams allow obtaining relevant information about the electrochemical processes that occur in the cell. It is also possible to evaluate the impact that extrinsic factors have on the battery impedance through the analysis of the changes that are seen on the Nyquist diagrams [9].

A typical Nyquist diagram of a lithium-ion battery is represented in Figure 17.

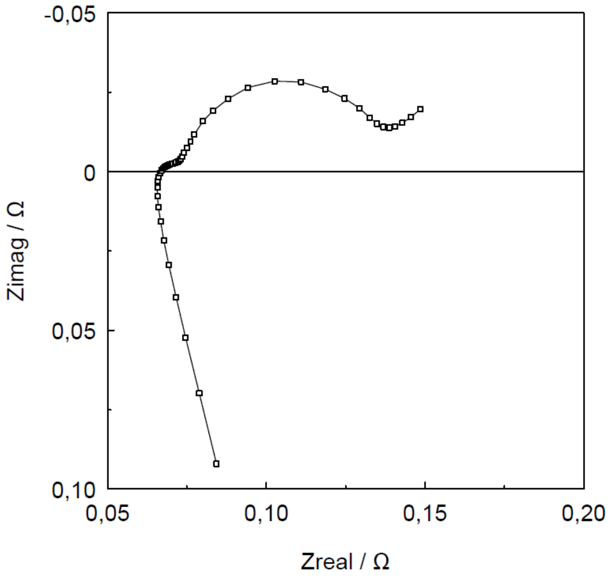

Figure 17: Nyquist plot of a charged NCA battery.

A Nyquist plot can be divided into different parts, associated with frequency regions. Each of them is related to certain dynamics and electrical behavior. To better understand what represents the real and imaginary parts of the plot, it is important to understand that a battery is an electrochemical system and, therefore, its components or interfaces where electrochemical reactions occur, may have properties similar to electric circuit elements.

3.2.3.1 Electrical circuit elements

The impedance of each of these elements is given by the expressions in Table 3:

Table 3: Current-voltage relationship and impedance of simple circuit elements [12, 44].

Component	Current Vs. Voltage	Impedance
Resistor	$E = IR$	$Z = R$
Inductor	$E = L\, di/dt$	$Z = j\omega L$
Capacitor	$I = C\, dE/dt$	$Z = 1/j\omega C$

As shown in Table 3, the impedance of a resistive element does not depend on frequency, it only has a real impedance component, represented as a point on the real axis. In a resistive element, current and potential are in phase. The impedance of an inductor element increases with frequency and has only an imaginary impedance component. Inductive behavior is represented in the positive part of the imaginary axis, where the ordinate of each point is proportional to frequency. In an inductor element, the current and potential have a phase angle of 90 degrees. The impedance of a capacitor increases as the frequency decreases and has only one imaginary impedance component. Therefore, it is represented in the negative part of the imaginary axis, where the ordinate of each point is inversely proportional to frequency. In a capacitor, the current and potential present a phase angle of 90 degrees [44, 47].

Thus, it is now easier to address the different regions of a typical lithium-ion cell's Nyquist plot.

The positive part of Z_{imag} at high frequencies is related to inductive behavior. Inductance is defined as the ability to store energy in an electric field, caused by a changing current flowing through the circuit. Thus, the connecting wires that are part of the external current circuit can present inductive behavior. However, this behaviour is not related to interfacial electrochemical processes, therefore the inductive region is often not considered. The Z_{real} value when the Nyquist plot intersects the X-axis, i.e., when $Z_{imag} = 0$, represents the moment where inductive and capacitive behavior balance each other, resulting in a purely resistive behavior. This value of Z_{real} represents the internal resistance of the cell. The first semicircle is attributed to the SEI, while the second relates to the charge transfer process, both having a capacitive and a resistive component. The 45º slope line represents the Warburg impedance, which is related to the diffusion process.

Since the real part of the diagram corresponds to the resistive component of the impedance, it is possible to distinguish and quantify different resistances in a typical Nyquist diagram of a battery, namely the internal resistance of the cell (R_{int}), of the Solid Electrolyte Interphase (R_{SEI}), of the charge transfer reaction (R_{CT}), and of the diffusion process (W) (Figure 18). The impedance of each of these components can be identified in the different frequency regions of the Nyquist diagram [13, 23].

(i) High frequency region

In the high frequency region, the point where the Nyquist diagram intersects the X-axis corresponds to the internal resistance of the battery [8, 48, 50].

(ii) Middle frequency region

In the mid-frequency region, two semicircles can be identified. The first, more to the left, is related to the resistance of the layer that forms between the electrolyte and the anode (SEI) due to the decomposition of the electrolyte, and its breakdown [9, 23]. The value of this resistance corresponds to the distance (on the real axis) between the starting and ending points of the first semicircle [8].

The second semicircle, rightmost, represents the charge transfer resistance, and the resistance value is calculated in the same way as the first semicircle [48, 50].

(iii) Low frequency region

The low frequency region, represented by a 45° slope line, describes the linear finite diffusion process [48, 50].

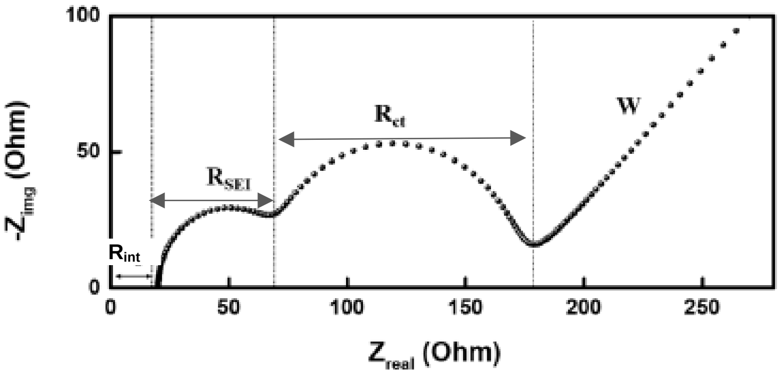

Figure 18: R_{int}, R_{SEI} and R_{CT} on a Nyquist plot [23].

3.2.4 Electrical Equivalent Circuit

It is common to analyze the impedance of a battery by fitting it to an Electrical Equivalent Circuit: an electrical circuit where different elements are associated to symbolize the physical/electric behavior of the cell since its components have capacitive and resistive properties. Thus, this circuit can be composed of common electrical elements such as resistors, capacitors, and inductors associated in series and/or in parallel [12, 44].

In these associations, the total impedance of a set of elements in series is equal to the sum of the individual impedances of each element:

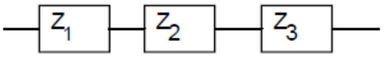

Figure 19: Circuit elements in series [44].

$$Z_{eq} = Z_1 + Z_2 + Z_3 \tag{25}$$

, and the inverse of the impedance of a set of elements in parallel is equal to the sum of the inverses of the impedances of each element:

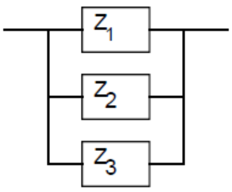

Figure 20: Circuit elements in parallel [44].

$$\frac{1}{Z_{eq}} = \frac{1}{Z_1} + \frac{1}{Z_2} + \frac{1}{Z_3} \tag{26}$$

3.2.5 EEC of a lithium-ion battery

The choice of an Electrical Equivalent Circuit should be focused not only on a good fitting result but mostly on its physical meaning, i.e., the model should be directly related to the physical processes occurring in the cell.

Several types of models can be found in the literature to represent batteries, depending on the obtained impedance spectrum, which differ in the type of elements chosen to represent the different processes taking place in a battery. The most used elements in an EEC of a lithium-ion battery are the following [9, 13]:

- **Resistor:** a purely resistive element that represents the internal resistance of the battery, obtained by EIS at high frequencies.
- **Capacitor:** an element which represents the electrochemical double layer, that forms due to charge separation at the electrode/electrolyte interphase. The electrode/electrolyte interphase is able to store charge in an electric field and release it through consecutive charges and discharges, allowing a non-faradaic current to flow [47].
- **Constant Phase Element (CPE):** an empirical element that best describes components whose capacitive properties are not those of an ideal capacitor. In battery components that exhibit a capacitive effect, the electrode surface has roughness and porosity due to the distribution of the active material particles, which means that the lithium intercalation and deintercalation process is not uniform along the surface. Thus, the elements with capacitive properties are replaced by CPEs, which better represent the heterogeneities of the surface. The impedance of a CPE is given by:

$$Z_{CPE} = \frac{1}{Q^0 (j\omega)^n} \tag{27}$$

  , where Q^0 is the admittance and n is a value between 0 and 1. When n=0, the CPE represents a resistor, when n=0.5, it represents a Warburg impedance and when n=1, it represents a capacitor [13].
- **Warburg Element:** an element that represents the diffusion of ions (mass transport) within the electrodes or electrolyte, governed by concentration gradients. Warburg impedance is observed in the low frequency zone of the Nyquist plot and is given by the following expression:

$$Z_{W_o} = \sigma\omega^{-\frac{1}{2}} - j\sigma\omega^{-\frac{1}{2}} \tag{28}$$

, where ω is the frequency and σ is the Warburg coefficient

$$\sigma = \frac{RT}{n^2 F^2 \sqrt{2}} \left(\frac{1}{c_{ox} D_{ox}^{1/2}} + \frac{1}{c_{ox} D_{ox}^{1/2}} \right) \tag{29}$$

, with *R* and *F* being the gas and Faraday constants, respectively, *T* is the temperature, n is the number of electrons involved in the process, c_{ox} and c_{red} are the concentrations of the oxidized and the reduced species, respectively, and D_{ox} and D_{red} are their respective diffusion coefficients.

Since the real and imaginary parts of the Warburg impedance are equal, it is represented in the Nyquist diagram as a 45º slope line.

However, this expression is only valid for an infinite diffusion length. A finite-length diffusion impedance can be defined by different expressions, being one of them the following:

$$Z_{W_o} = W_o \frac{\coth\left(\left(I\frac{l^2}{D}\omega\right)^{\phi}\right)}{\left(I\frac{l^2}{D}\omega\right)^{\phi}} \tag{30}$$

, where W_o is the Warburg resistance, ω is the frequency, l corresponds to the specific diffusion thickness, D is the diffusion coefficient of the particle and ϕ is the phase angle shift between current and voltage [13, 47, 51].

The electrical equivalent circuit of a lithium-ion battery, considering its components, can be represented as follows:

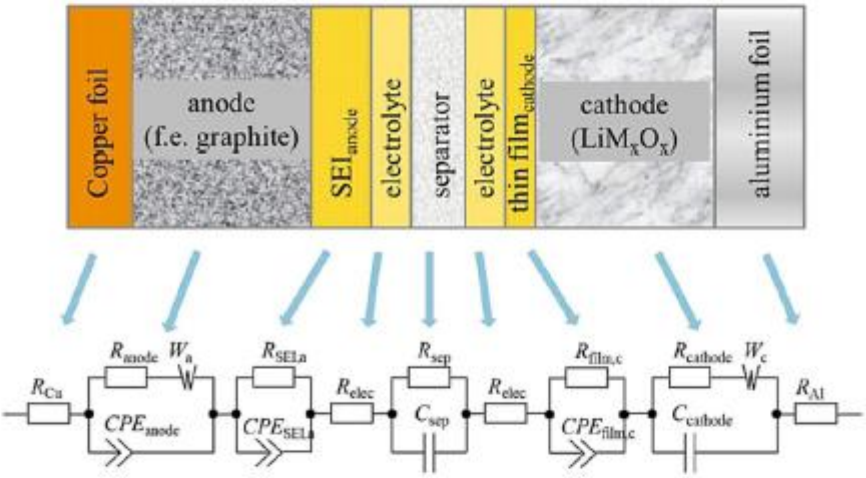

Figure 21: Electrical Equivalent Circuit of a Lithium-ion battery [23].

However, the capacitive effect of the separator (C_{sep}) is considered small enough to be neglected in a simplified model. Moreover, one might also consider joining the resistances of the current collectors, $R_{\text{current collector}}$, the electrolyte, $R_{electrolyte}$, and the separator, $R_{separator}$, into a single parameter, the internal resistance, R_{int} [13]. The capacitance of certain components is modeled with a CPE, as they do not behave as an ideal capacitor.

Thus, it is common to use a simplified electrical equivalent circuit that can still describe the most significant phenomena occurring in the cell. The preferred model for lithium-ion batteries whose Nyquist diagram shows two semicircles is composed of a resistor to represent the internal resistance, a ZARC circuit (a CPE element in parallel with a resistor) to represent the first semicircle, and, to represent the second semicircle and the diffusion process, a ZARC circuit is used, where in the resistor branch a Warburg element is added in series (the points corresponding to inductance behavior are not included in this type of EEC) [9, 23]. This model is schematized in Figure 22:

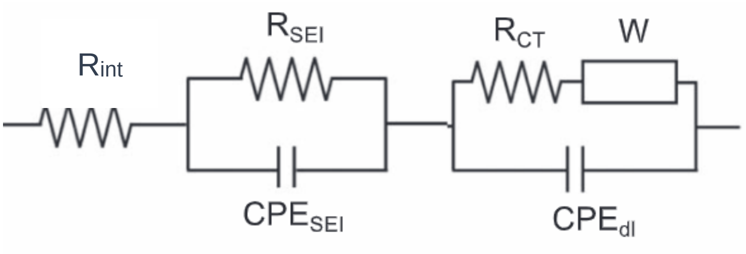

Figure 22: Simplified Electrical Equivalent Circuit for a lithium-ion battery [27].

Where R_{int} represents the internal resistance of the cell (which includes the resistances of the electrolyte, separator and current collectors); R_{SEI} and CPE_{SEI} represent the resistance and capacitance of the SEI formed on the anode, respectively; R_{CT} represents the charge transfer resistance in the cathode (resistance to the movement of electrons); CPE_{dl} represents the capacitance of the double layer (formed by separation of positive and negative charges at both sides of the cathode/electrolyte interphase) and W represents the finite diffusion (mass transport process) [13, 23, 27, 47].

Some of these parameters can be readily obtained by analyzing the Nyquist plot typically obtained for lithium-ion batteries, as already mentioned and shown in Figure 18.

3.2.5 Influence of ageing on a battery's impedance

As the battery degrades, the Nyquist diagram shifts to higher Z_{real} values, and some changes in the shape of the semicircles are observed [13, 23].

R_{int} is not expected to present any significative changes with SOC, over a single cycle. Instead, R_{int} increases with the number of cycles mostly due to electrolyte decomposition and SEI formation from its decomposition products. Since these are the most significant mechanisms in LIBs, R_{int} is normally the parameter that changes more substantially with cycling, thus internal resistance is a very important parameter on the determination of the SOH of a battery. However, it is noteworthy that the first semicircle of the Nyquist plot is related to the SEI, so the contribution of SEI formation to R_{int} increase consists only in being a secondary effect of electrolyte decomposition. R_{int} tends to decline for higher temperatures [8, 9, 23, 48].

The SEI is a solid layer that forms at the interface between the anode and the electrolyte, thus having both capacitive and resistive properties, represented in a Nyquist diagram by a semicircle. SEI formation and growth makes the intercalation and de-intercalation reactions of lithium-ions more difficult by acting as a barrier to their movement, causing simultaneously an impedance increase and a loss of capacity. Since this growth happens gradually over time, R_{SEI} is expected to increase with the number of cycles [8, 27].

The second semicircle is related to the interfacial processes, comprising the reactional impedance, $R_{CT,}$ and the double layer capacitance. Therefore, it is expected that at the beginning of a discharge, as the system tends to evolve to a more disordered state, charge transfer is facilitated, so R_{CT} will be low, increasing as discharge progresses. A fully charged battery has a high R_{CT}, because during charging the lithium ions have moved to the anode, occupying a large portion of the intercalation spaces. As there are fewer and fewer intercalation spaces at the anode to accommodate lithium ions, the resistance to transfer of ions and electrons increases. When the battery starts to be discharged, the reaction occurs in the opposite direction. Thus, lithium ions migrate to the still lithium-poor cathode, so R_{CT} decreases dramatically at this early stage of discharge since there are still many free intercalation spaces and both ions and electrons flow easily. As the discharge proceeds, R_{CT} increases, reaching its maximum when the battery is fully discharged. Overall, R_{CT} values are higher for a completely discharged battery than for a completely charged one. This behavior is attributed to the structure of the cathode itself, which offers more resistance to Li-ion transfer than the graphite. Furthermore, R_{CT} is expected to increase with cycling since both Li-ions and electrons take part in secondary irreversible reactions, such as SEI formation and growth. Thus, the SEI is only indirectly related to charge transfer resistance since it is a solid barrier that hinders charge transfer and its formation and growth consume active material [8, 27, 52].

Warburg impedance is always higher for lower frequencies, given that the distance over which species diffuse is greater. Diffusion depends on the diffusion coefficient, which is higher when there are more available intercalation spaces. Therefore, the diffusion coefficient decreases for the cathode and increases for the anode as SOC decreases (during discharge). Thus, while the Li-ions are diffusing to the cathode (lower SOC), Warburg impedance increases [34, 51].

4 Experimental Part

The experimental work of this dissertation is divided into two parts. The first part consists of studying individual cells, one new and one already used, by charge-discharge cycling and galvanostatic EIS. The second part comprises the same type of studies, but for two cells connected in parallel and two used cells connected in parallel.

4.1 Equipment and material

In this work, two types of cells were studied.

1) Panasonic NCR18650B cells, 3.6V nominal voltage, NCR cathode, 3.25Ah capacity. These commercial cells were acquired as new. For simplicity, these cells will be further addressed as “new cells”.
2) Panasonic NCR18650 cells, 3.6V nominal voltage, NCR cathode, 2.9Ah capacity. These cells are inserted in a discarded battery module of an electric vehicle (the reason for the replacement of this module is not known, therefore it cannot be assumed that it reached its end-of-life capacity or resistance values, but it is assumed that it was already subjected to some cycle ageing). The electrical connections between individual cells were removed. For simplicity, these cells will be further designated as the “used cells”.

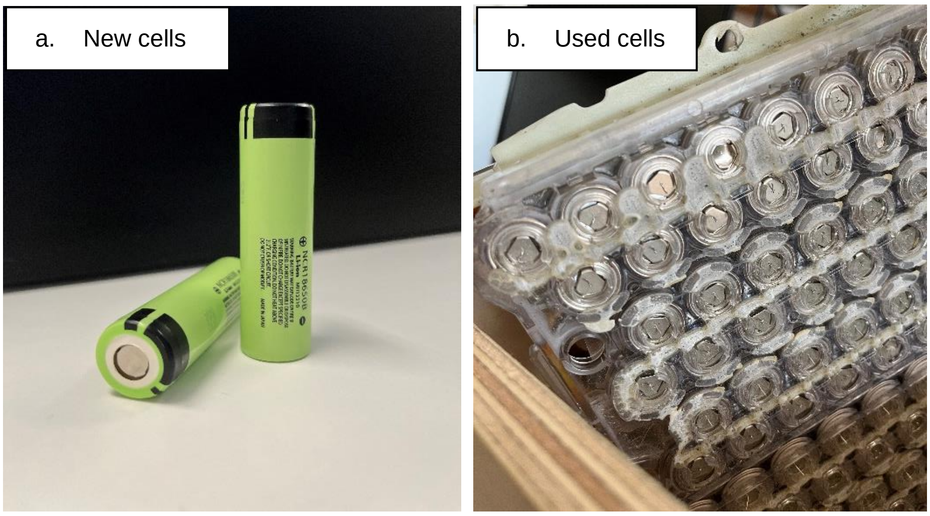

Figure 23: a. New Panasonic NCR18650B cells; b. Used Panasonic NCR18650 cells in an EV battery module.

Further information about the characteristics of these cells can be found in Tables 4 and 5.

Table 4: Specifications of Panasonic NCR18650 cells [53].

Rated Capacity at 20°C	**2.9 Ah**
Nominal Voltage	3.6V
Charging	CC-CV, Std. 1925mA, 4.2V, 50mA cut-off
Discharging	CC, 550mA, 2.5V
Weight	44.5g
Dimensions	Max 65.2mm x Ø16.6mm

Table 5: Specifications of Panasonic NCR18650B cells [43].

Capacity at 25°C	**Min. 3.25 Ah**
Nominal Voltage	3.6V
Charging	CC-CV, Std. 1625mA, 4.2V, 65mA cut-off
Discharging	CC, 3250 mA, 2.5V
Weight (max.)	48.5g
Temperature	Charge: 0 to +45°C Discharge: -20 to +60°C Storage: -20 to +50°C
Energy Density (based on bare cell dimensions)	Volumetric: 676 Wh/l Gravimetric: 243 Wh/kg
Dimensions	Max 65.3mm x Ø18.5mm

For both charge-discharge cycling and Electrochemical Impedance Spectroscopy measurements, a Gamry Interface 5000E™ potentiostat was used.

The fitting of an Electrical Equivalent Circuit to the obtained Nyquist diagrams was performed based on the non-linear least squares method (NLLS) using the software ZView® Version 4.0f.

4.2 Procedure

4.2.1 Cycling and EIS testing of individual cells

For each of the cell models, one cell was subjected to cycling, and the cell’s capacity value was obtained during every charge step.

The external current circuit was connected to the batteries by pressing metallic contacts against the positive and negative terminals of the battery. Soldering was avoided to ensure maximum battery safety conditions. Since the external circuit was only connected to the cell by direct contact, previously to any cycling it was confirmed that the system was stabilized and that the resistance for current flow is minimized.

For both models, the selected cell was fully discharged prior to cycling. Each cycle consisted in a full charge in CC-CV mode to 4.2V by applying the constant charge current specified by the manufacturer for each of the models, and then holding that maximum potential until the current decreased to the specified cut-off current value. This step was followed by a 1-hour rest period, with subsequent impedance measurement. The discharge was divided into four steps of equal potential interval. For the new battery, where higher discharge currents were applied, as soon as the discharge started, the voltage dropped to 3.6V. Therefore, the discharge potential range was considered between 3.6V and 2.5V, so each discharge step corresponds to an interval of 0.275V. The first discharge step stops at 3.325V, the second at 3.05V, the third at 2.775V and the fourth at 2.5V. Even though the initial voltage drop for a used cell was not as high as for a new cell since a lower current is applied, the same voltage thresholds were maintained for purposes of potential comparison. After each discharge step there was a 30-minute rest period, followed by an impedance measurement.

The galvanostatic EIS tests were performed according to the following conditions:

Table 6: Selected parameters for the EIS tests.

DC current (A)	0
AC current (A rms)	0.03
Initial frequency (Hz)	50000
Final frequency (Hz)	0.01
Points/decade	7
Estimated Z (ohm)	0.01

In order to have an estimation of the runtime of a single cycle, and from there define the appropriate number of cycles to apply to the cells, a schematization of the cycling plan was done for both new and used cells, taking into account their specifications.

4.2.1.1 New cell

The different stages of a single charge-discharge cycle and their respective duration were estimated for a new cell, in order to predict the average runtime of a single cycle (Figure 24).

As the specified charge current is 1.625A (0.5C-rate), ideally the cell would take about 2 hours to fully charge up to its 3.25Ah rated capacity. However, this does not account for the Constant Voltage step of the charging process. To have a more realistic idea of the charge time, its duration was verified experimentally, and it was found that the Constant Current stage is expected to last for about 1 hour and 15 minutes and the Constant Voltage stage for about 1 hour and 55 minutes.

As for discharge, using the specified current of 3.25A (1C-rate), it is expected to fully discharge a battery within 1 hour. Since there are 4 discharge steps, this time is divided by 4 to represent average time per discharge, however this is done for schematization purposes only and should not be assumed as true, since it is known that the typical discharge of a battery evolves much faster in the beginning and at the end of the discharge than in the middle. The rest period after charging was defined as 1 hour and the rest period after each discharge step is 30 minutes. One EIS test has approximately 20 minutes of runtime.

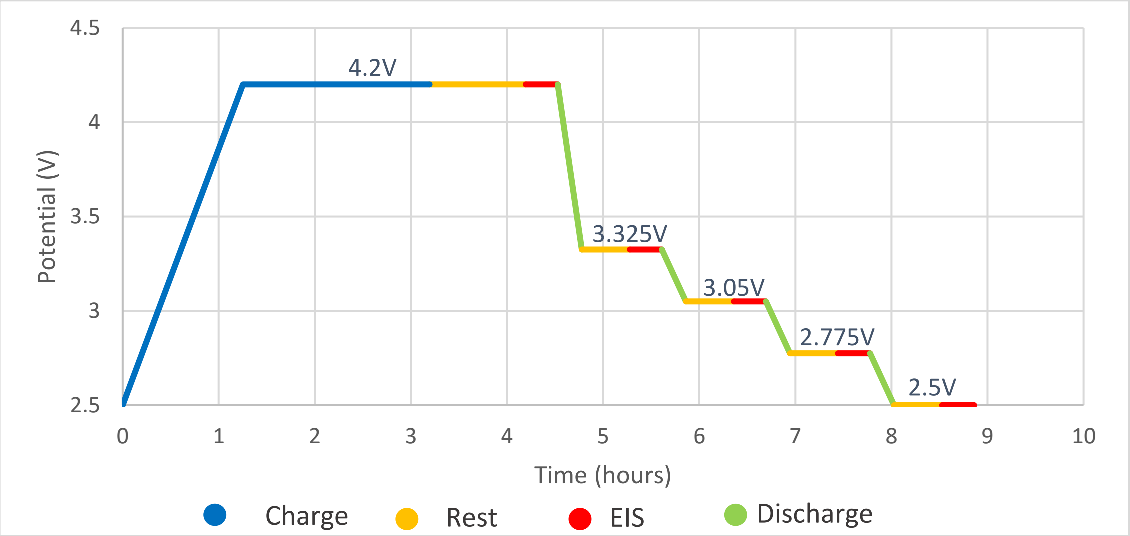

Figure 24: Expected runtime of a single cycle for a new cell.

A new cell would take about 9 hours to complete a full charge-discharge cycle, which corresponds to less than 3 cycles per day.

4.2.1.2 Used cell

For the used cell, a schematic of a single cycle was also defined (Figure 25). The specified charge current is 1.925A, and at this current it would take about 1 hour and 30 minutes to fully charge a cell, not accounting for the Constant Voltage step. Experimentally it was concluded that the duration of the Constant Current step is about 1 hour, and the Constant Voltage step lasts for about 1 hour and 40 minutes. At the specified discharge current of 0.55A, the cell is expected to fully discharge within 5 hours and 15 minutes. This discharge time was divided by the four discharge steps. As in section 4.2.1.1, the rest period after charging is 1 hour and the rest period after every step of the discharge is 30 minutes. EIS tests have a duration of 20 minutes.

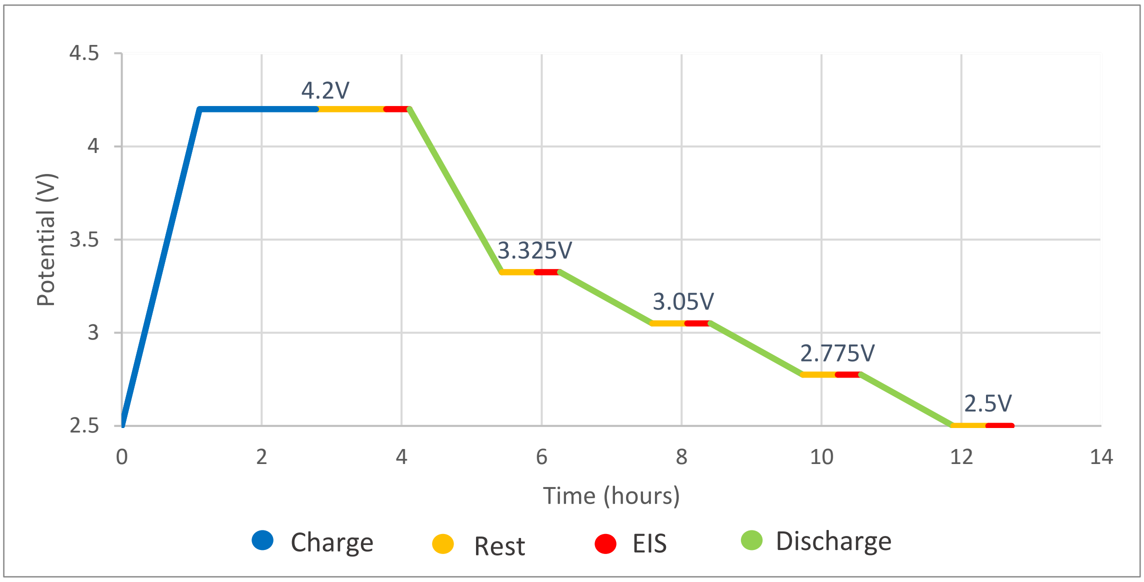

Figure 25: Expected runtime of a single cycle for a used cell.

A used cell takes more than 12 hours to complete a single cycle, corresponding to less than 2 cycles per day.

Considering the average runtime of a single cycle for new and used cells and the available time to carry out this work, it was defined that the best option was to subject each cell to 50 charge-discharge cycles, since at this point it is already possible to identify some ageing effects.

In total, cycling the new battery 50 times corresponds to 440 hours (18 days and 8 hours), and cycling the used battery 50 times corresponds to 636 hours (26 days and 12 hours).

4.2.2 Cycling and EIS tests of two parallel-connected cells

As electric vehicle battery diagnosis is often performed in modules rather than individual cells, it can be useful to study the impedance of cells connected to each other. As the available equipment could not support twice as the specified maximum potentials, it was not possible to cycle two cells in series. Instead, two of the new cells are connected in parallel, subjected to 50 charge-discharge cycles, and their impedance is measured by EIS during cycling.

4.2.2.1 New cells

For two cells in parallel, the applied charge and discharge current must be doubled, while the potential values are maintained. The specified discharge current for a single new cell is 3.25A, so, for two cells in parallel, a discharge current of 6.5A should be used. However, the used potentiostat has a current limit of 5A. The selected approach was to define a discharge current of 5A for the two cells in parallel (corresponding to a discharge current of 2.5A for a single cell). Regarding charging, the current to apply to two cells in parallel does not reach the maximum current of the equipment, therefore the specified conditions were maintained.

Furthermore, a different cycling sequence was applied. Every 5 cycles (i.e., cycles 1, 5, 10, 15…50), the discharge was divided into 4 steps, exactly like the methodology for cycling individual cells (this type of cycle will be referred to as "long cycle"). For the rest of the cycles, discharge was performed in a single step, i.e., those cycles consist of a full charge followed by impedance measurement and a full discharge followed by impedance measurement (this type of cycle will be referred to as "fast cycle").

Therefore, to understand the behavior of these two cells individually, subjected to these different cycling conditions and discharge current values, each of them was subjected to two cycles: one where the discharge was done in 4 steps (long cycle) and another where discharge was done in 1 step (fast cycle), already applying the new defined discharge currents.

These individual tests also provided important information about the expected runtime of a single long cycle and a single fast cycle, schematized in Figure 26 and 27, respectively. The charge time was determined experimentally due to the CV step (it was verified that even though the specified charging conditions were maintained, the charge time for the CC step was the same as for the individual cell, but the CV step takes longer), and the discharge time was calculated based on the discharge current.

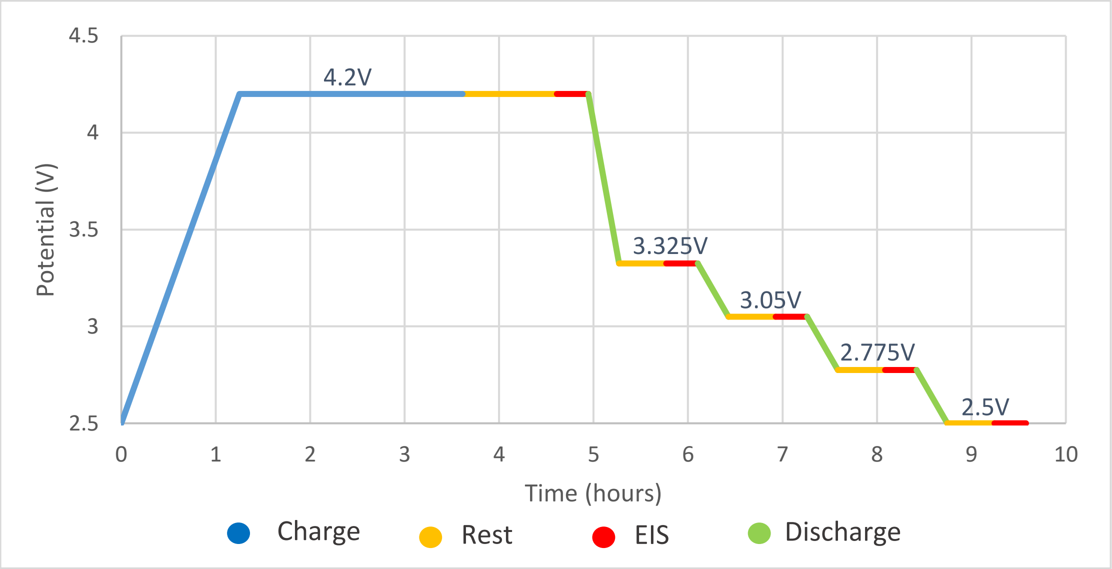

Figure 26: Expected runtime of a single "long cycle" for two new cells in parallel.

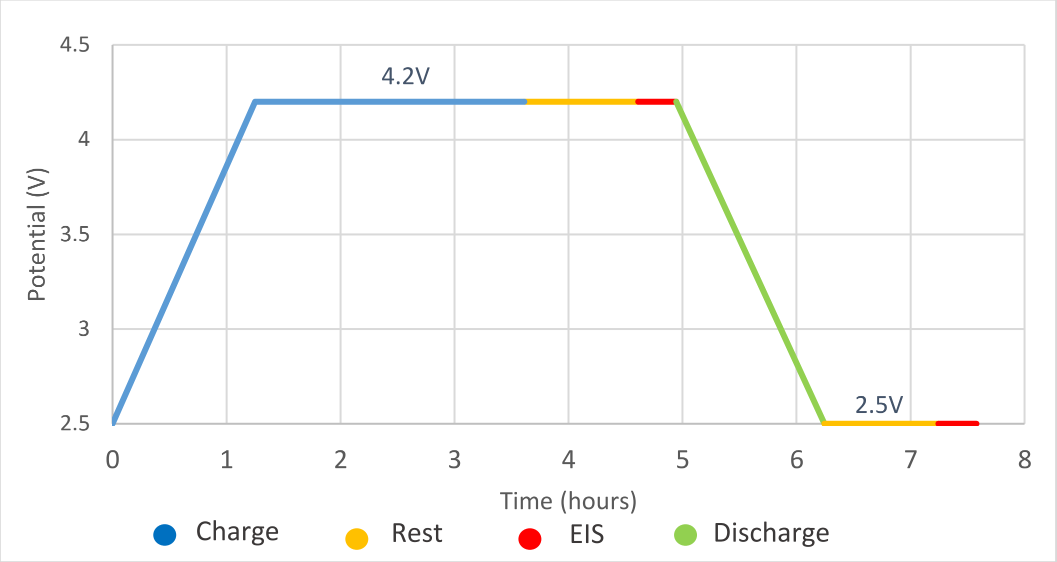

Figure 27: Expected runtime of a single "fast cycle" for two new cells in parallel.

Each one of the long cycles takes almost 10 hours, while the duration of the short cycles is less than 8 hours. The 50-cycle sequence is composed of 11 long cycles and 39 short cycles, corresponding to a total of 398 hours (19 days and 14 hours).

After the two cells were individually tested, they were finally connected in parallel and subjected to the 50 charge-discharge cycles.

The parameters used for measuring the impedance values were the same as for the individual cells (Table 6).

4.2.2.2 Used cells

For the used cells in parallel, the charge and discharge conditions specified by the manufacturer were maintained since the charge current is now 3.65A and the discharge current is 1.1A, which does not reach the maximum current values of the potentiostat. The same cycling sequence as in 4.2.2.1 was applied.

Likewise, the expected runtime of each "long cycle" and "fast cycle" was estimated and represented in Figures 28 and 29, respectively.

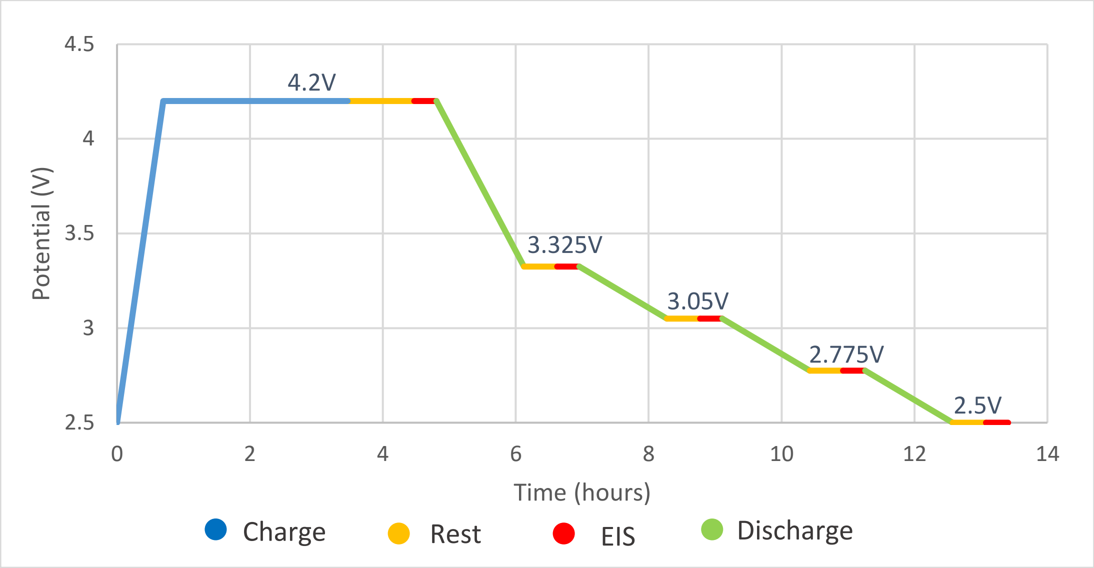

Figure 28: Expected runtime of a single "long cycle" for two used cells in parallel.

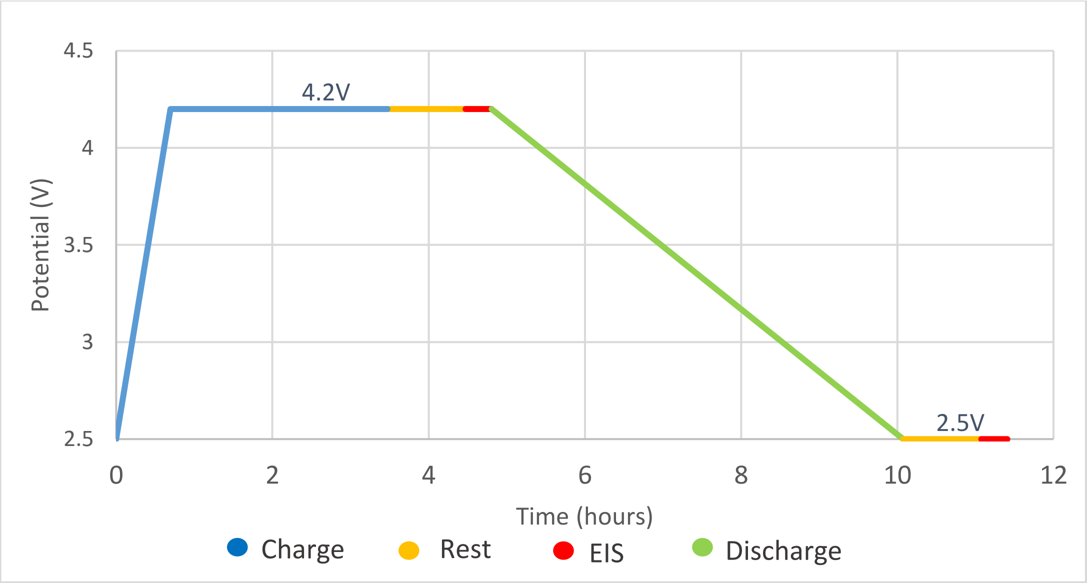

Figure 29: Expected runtime of a single "fast cycle" for two used cells in parallel.

Each one of the long cycles takes about 13 and a half hours and each of the fast cycles takes almost 11 and a half hours. Therefore, 50 cycles take 592 hours, which corresponds to 24 days and 16 hours.

Like for the new cells in parallel, the individual used cells were previously tested separately and then connected and subjected to 50 charge-discharge cycles.

5 Results and Discussion

5.1 Capacity and impedance analysis of individual cells

The electrical equivalent circuit defined for the studied batteries is shown in Figure 30. This type of EEC, already reviewed in Chapter 3, revealed to be a good physical approximation to the processes happening in the cell, with the addition of having a goodness of fit in the order of 10^{-6}.

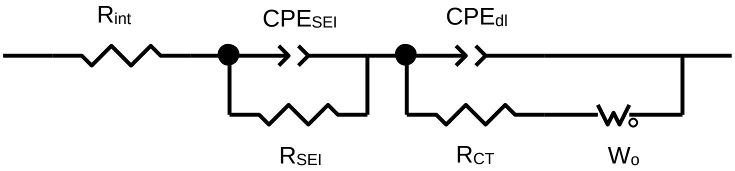

Figure 30: Electrical Equivalent Circuit defined for the lithium-ion batteries being studied.

5.1.1 Capacity and impedance analysis of a new cell

For every cycle, during charging, the amount of charge provided to the battery was tracked in Coulomb, which is the unit of electric charge transferred by a 1A current over one second. Since 1 Ah equals 3600 Coulomb, the charge value in Coulomb is divided by 3600 (seconds) to obtain actual capacity in Ah. Battery capacity is represented as a percentage of the rated capacity in Figure 31.

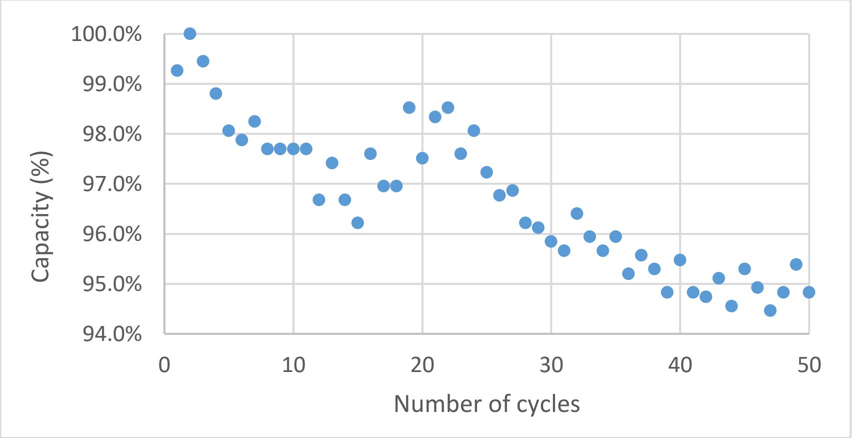

Figure 31: Capacity of a NCR18650B new cell over 50 charge-discharge cycles.

It is noticeable that the overall capacity loss of 5-6% over the 50 cycles is not linear. In fact, it is even possible to identify a substantial capacity recovery between cycles 15 and 19.

Figures 32.a. and 32.b. represent the Nyquist plots of a new cell at different charge states (after a complete charge and after every discharge step, with “Discharge 4” corresponding to the totally discharged cell) for the 1st and the 50th cycles, respectively.

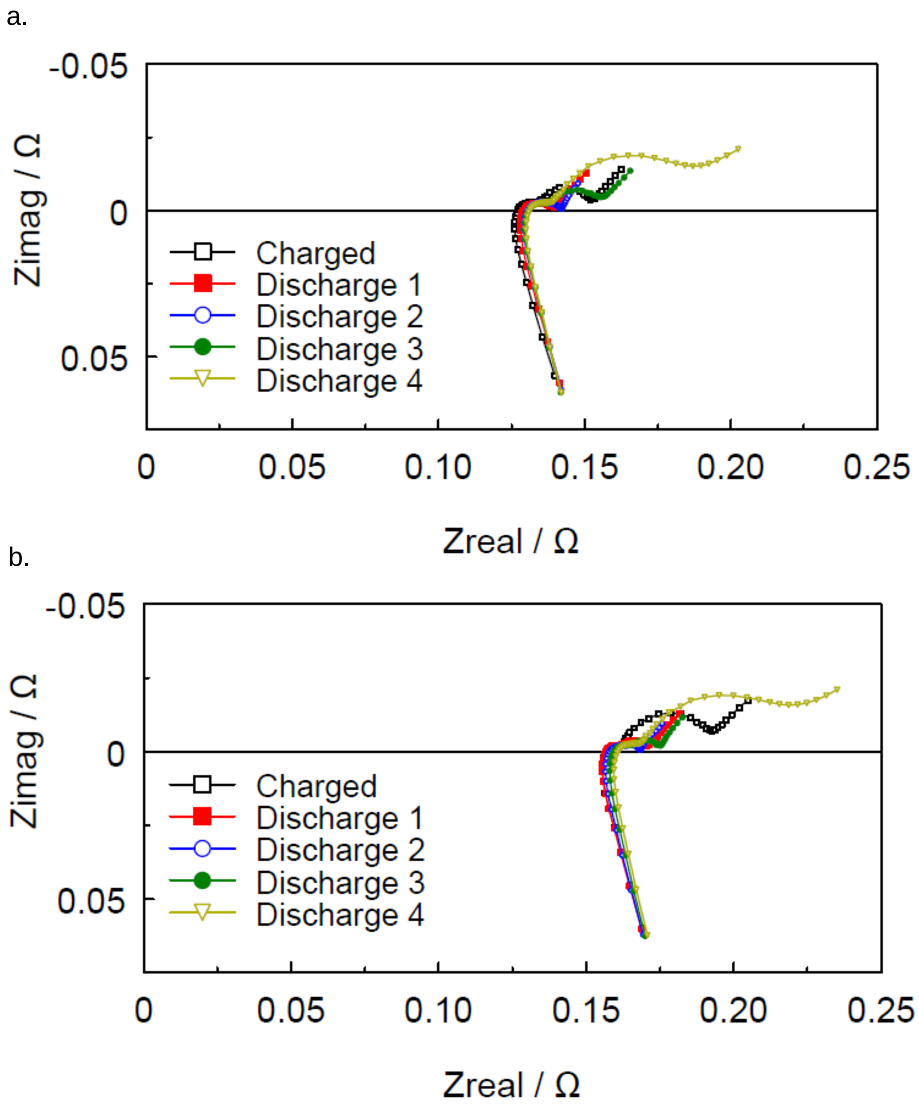

Figure 32: Full Nyquist plots of the new cell at different charge states in the a. 1st cycle; b. 50th cycle.

As the cell charges and discharges over a single cycle, the cell impedance changes. For both 1st and 50th cycles (Figure 32), it is possible to identify a slight increase of R_{int} as the cell discharges (lower SOC). To better visualize and compare impedance changes other than the internal resistance, R_{int} was subtracted to all the spectra (R_{int}= 0 Ω) (Figure 33).

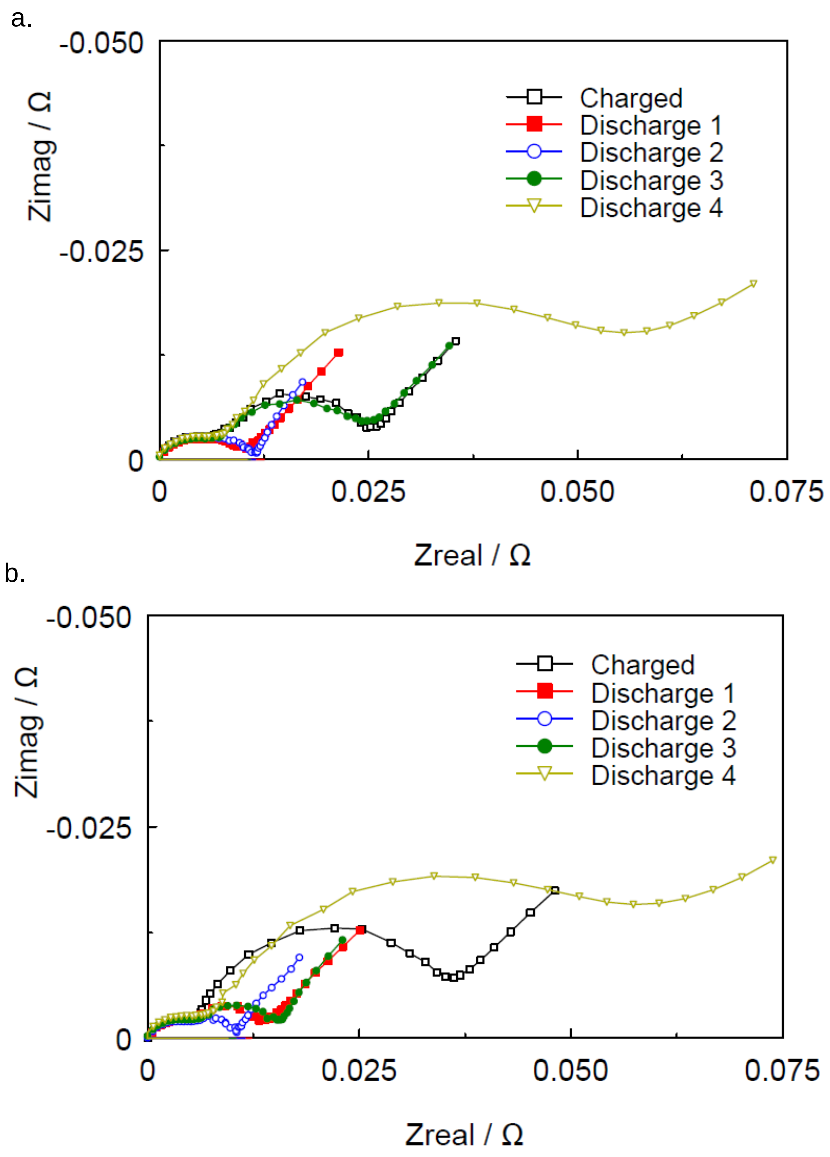

Figure 33: Nyquist plots of the new cell at different charge states in the a. 1st cycle; b. 50th cycle, with R_{int} subtracted to all the spectra.

In the 1st cycle, when the battery is fully charged, the value of R_{CT} is higher than the value of R_{SEI}. After the first discharge stage, both values decrease. R_{SEI} evolution over the discharge process is difficult to visualize, due to the small diameter of the first semicircle (Figure 33). By analyzing the R_{SEI} values obtained by the EEC fitting, it was possible to verify that this parameter declines by one order of magnitude in the first discharge, compared to the charged state, and increases in the same proportion for the last discharge stage. This change is not as significative as the remainder parameters. This is in accordance with the fact that R_{SEI} is expected to increase as the thickness of the SEI grows, therefore, any significant changes will probably be seen only after a long cycle number, and not at different charge states of a single cycle.

R_{CT} decreases substantially after the first discharge, compared to the fully charged state, but then increases gradually as SoC is lower (Figure 33.a.). This effect may be explained by the fact that when the battery is fully charged, the lithium-ions have already occupied most of the intercalation spaces in the anode, and therefore there is a higher resistance to this charge transfer. When the discharge begins the reaction starts to occur in the opposite direction, and it is expected that the resistance to charge transfer decreases considerably, because the system tends to evolve to a disordered state, so the Li-ions tend to flow to the opposite electrode, while the electrons flow in the same direction through the external circuit. There is still enough space available to accommodate the lithium ions in the lithium-depleted cathode, and there is a high number of electrons flowing.

This increase of R_{CT} is even more significant after the third and fourth stages of discharge (Figure 33.a.). As expected, the resistance to charge transfer is always higher at the end of the discharge process, since at this stage there are less electrons being transferred and Li^+ ions have less intercalation spaces to accommodate them.

W_o is lower for Discharge 1, compared to the charged state, and starts increasing after the third discharge. The higher value of W_o corresponds to the totally discharged state, as diffusion gets progressively more difficult at the end of the discharge.

In the 50th cycle, R_{SEI} shows the same behavior as in the 1st cycle. Regarding R_{CT}, it decreases significantly as discharge begins, but this second semicircle does not change considerably in the following second and third discharges, appearing much larger after the 4th discharge. As for W_o, the behavior is similar to the 1st cycle, having the higher value of W_o at the totally discharged stage. (Figure 33.b.).

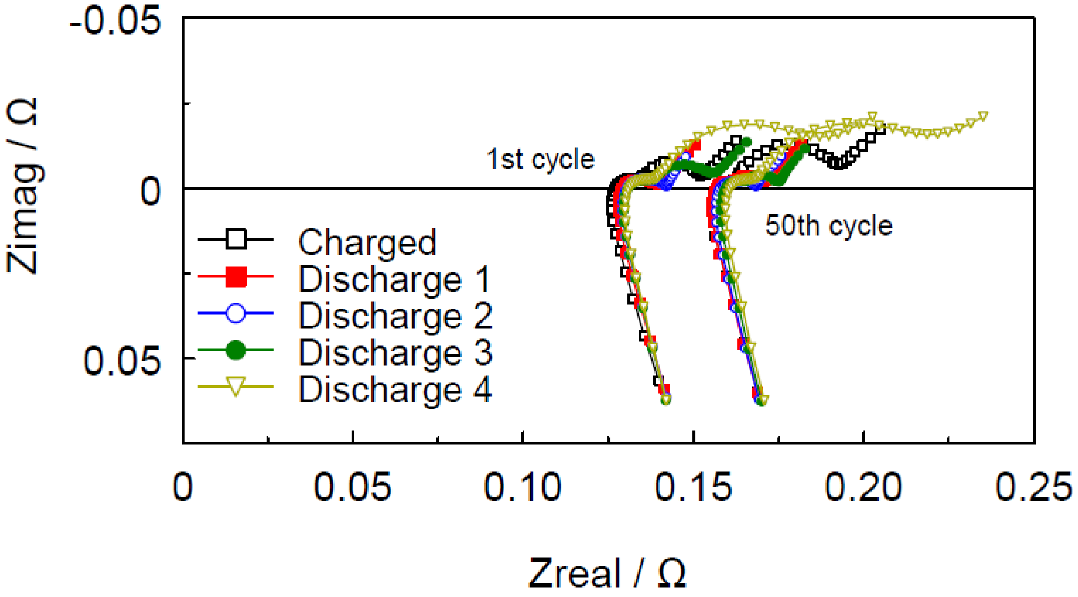

Figure 34: Nyquist plots of a new cell at different charge states for the 1st and 50th cycles.

By analyzing the Nyquist plots at different charge states for the 1st and the 50th cycle (Figure 34) it is verified that R_{int} is the parameter that changes more substantially with ageing, showing an increase of 23.9% during the 50 cycles. While R_{int} showed to increase mostly over cycling, the other parameters are clearly more influenced by the SOC and their variation at different charge states is not coherent. R_{int} being the most notable change was already expected since SEI formation is the main degradation mechanism in LIBs. Even though the first semicircle of the Nyquist plot is related to the SEI, the formation of this layer also plays a role on internal resistance since its formation is an effect of the reduction of the electrolyte.

Figure 35 shows the Nyquist plots obtained at fully charged and fully discharged states for every 10 cycles.

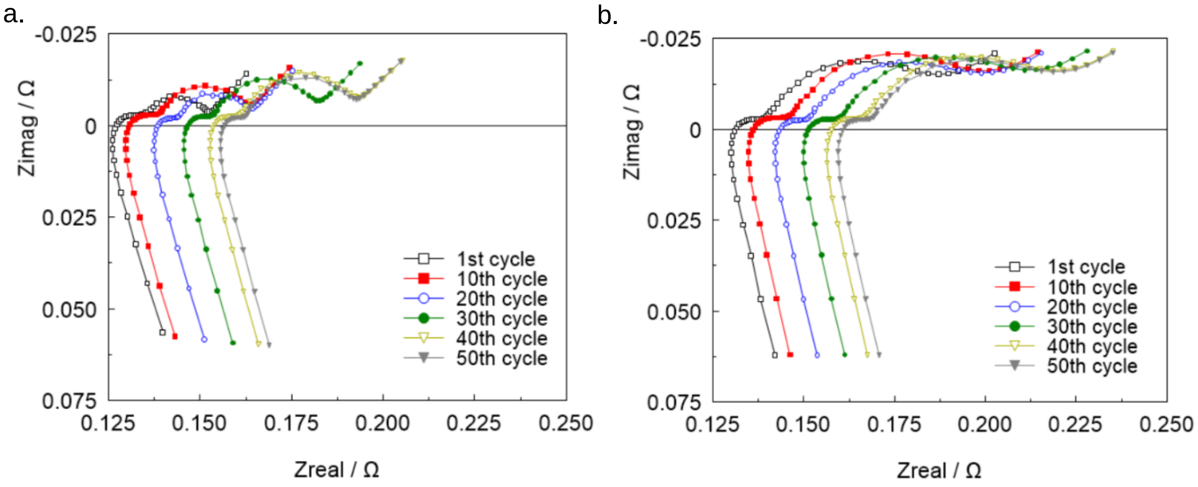

Figure 35: a. Nyquist plots of the charged new cell for every 10 cycles; b. Nyquist plots of the discharged new cell for every 10 cycles.

As expected, R_{int} increases gradually with cycling. While at the fully discharged state (Figure 35.b.) the Nyquist plot appears similar over cycling (Figure 35.a.), the same is not verified at the charged state.

In order to understand how R_{SEI}, R_{CT} and W_o evolve over cycling, R_{int} was subtracted to the Nyquist diagrams (Figure 36).

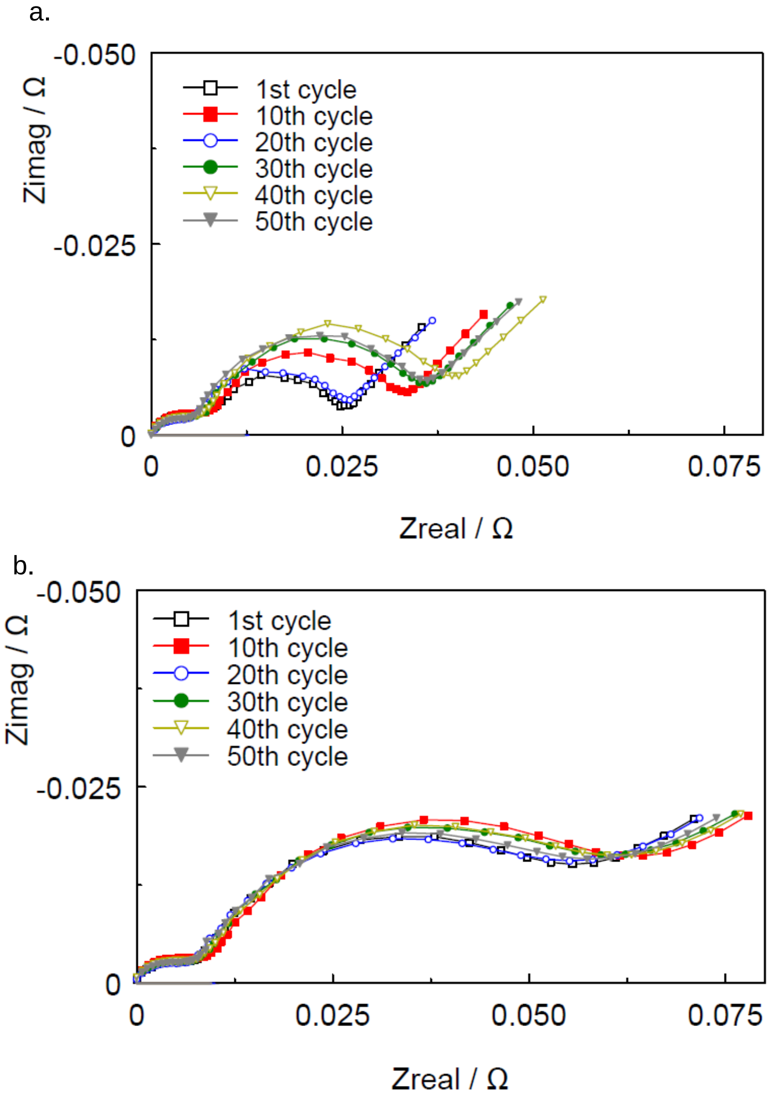

Figure 36: a. Nyquist plots of the charged new cell for every 10 cycles, moved to R_{int} = 0 Ω; Nyquist plots of the discharged new cell for every 10 cycles, moved to R_{int} = 0 Ω.

Even though R_{SEI} evolution cannot be clearly identified in Figure 36, it was found from the EEC fitting data that this parameter does not increase over the 50 cycles, its evolution is irregular, showing a slight decline overall. R_{SEI} is related to the resistance of the SEI layer, therefore this parameter is expected to increase over cycling, although its evolution will not be as significant as the other parameters. Most likely, 50 cycles are insufficient to identify the increase of R_{SEI}. A decrease in R_{SEI} over the first 100 cycles was reported by Krause et al. [27] and was attributed to the instability of the as-formed SEI layer, verifying a posterior R_{SEI} increase with cycling once it achieves stability.

From Figure 36.a. it is possible to verify that at a charged state, the second semicircle, and therefore R_{CT}, does not always increase gradually. In fact, the second semicircle of the 20^{th} cycle is very similar to the one of the 1^{st} cycle, when it was expected to be between the 10^{th} and the 30^{th}-cycle semicircles. The R_{CT} increase from the 1^{st} to the 10^{th} cycles and from the 20^{th} to the 40^{th} cycles coincides with a capacity loss. Between the 10^{th} and the 20^{th} cycles, capacity shows an incoherent behaviour, increasing and decreasing, with capacity percentages being almost the same for the 10^{th} and 20^{th} cycles, while R_{CT}

showed to be much lower for the 20th cycle than for the 10th. Between the 40th and 50th cycles capacity irregularly increased and decreased, being lower for the 50th cycle than for the 40th, and R_{CT} decreased. As for the discharged state (Figure 36.b.), it was confirmed that impedance is very similar over cycling, even though the same impedance decrease at the 20th cycle is identified. Since R_{CT} is highly dependent on SOC, having higher variations of R_{CT} at the charged state compared to almost no variation at the discharged state could be related to the decrease of the maximum attainable SOC as the cell ages, while when the cell is discharged the SOC is always zero.

Warburg impedance increases slightly with cycling, which is verified for both the charged and discharged state.

In order to assess the decrease of R_{CT} in the 20th cycle, compared to the 10th, a closer look was taken at impedance evolution between the 10th and 20th cycles and between the 20th and 30th cycles, for the charged cell.

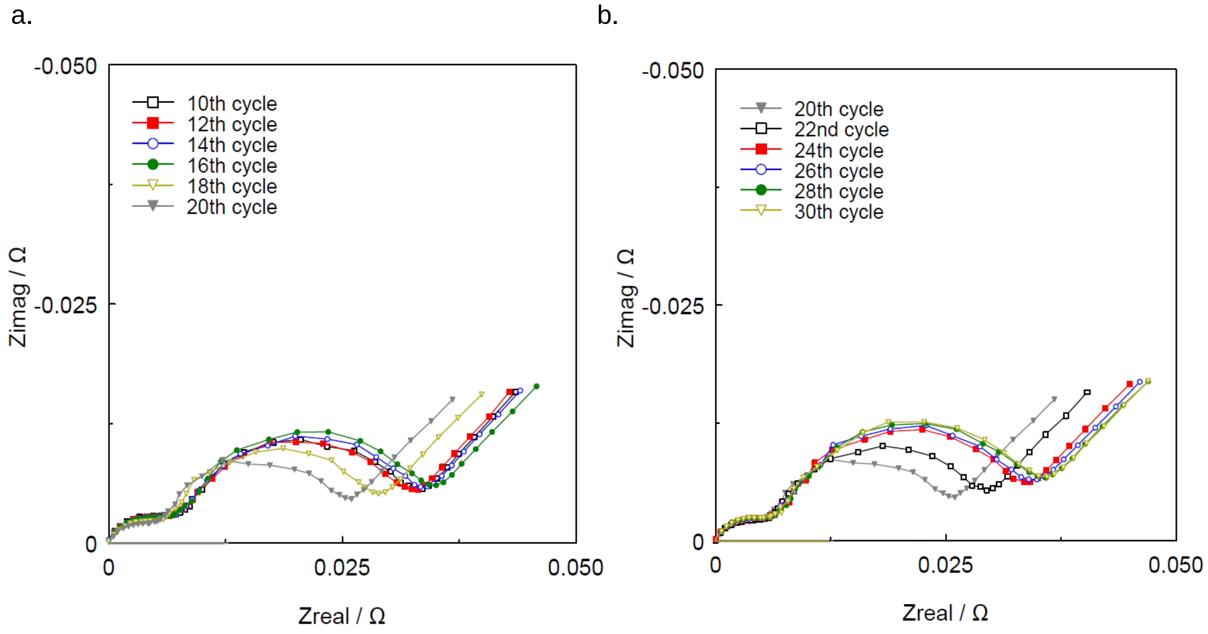

Figure 37: a. Impedance of a charged new cell between the 10th and 20th cycle, with R_{int} subtracted to all the spectra; b. Impedance of a charged new cell between the 20th and the 30th cycle, with R_{int} subtracted to all the spectra.

Figure 37.a. shows that the second semicircle grows from the 10th to the 16th cycle, while capacity decreases and increases over the same interval, followed by a more accentuated decrease of R_{CT} until the 20th cycle, again with capacity varying irregularly. In Figure 37.b. it can be seen that impedance increases gradually from the 20th to the 30th cycle, while capacity decreased more gradually too. It was not found a specific reason for the incoherent behavior of impedance and capacity, as there were no considerable differences in charging time for these cycles, however it can be identified that a more stable R_{CT} evolution coincides with a stable capacity variation, and the same is verified for irregular variations.

R_{int}, R_{SEI}, R_{CT} and W_o variations of the new cell over 50 cycles are represented in Figure 38.

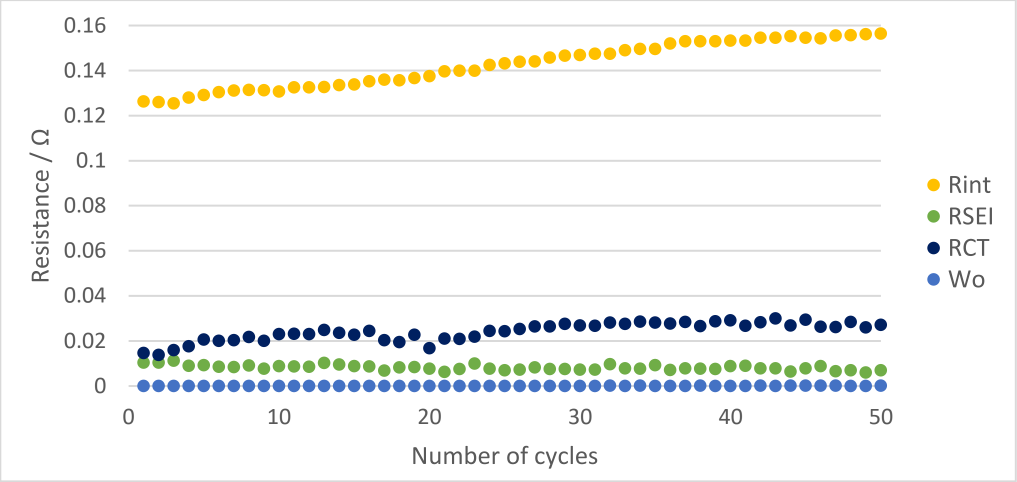

Figure 38: R_{int}, R_{SEI}, R_{CT} and W_o of the charged new cell over cycling.

By impedance analysis of the new cell, it was possible to verify that even though impedance generally increases over cycling, not all of the impedance components necessarily increase over consecutive cycles, as was verified particularly for R_{CT}.

R_{int} increased most significantly over cycling, not having any substantial variation at different SOC. Even though the decrease in R_{int} between the 30th and 40th cycles did not coincide with a capacity recovery, the overall R_{int} increase over the 50 cycles is consistent with a capacity loss. Therefore, this parameter reveals to be useful for quantifying the ageing of a battery, independently of its current SOC. Regarding R_{SEI}, a significant variation could probably only be identified over a larger number of cycles, so this parameter is not the most adequate for SOH determination. R_{CT} is strongly affected by SOC and even though its stable or unstable evolution can be found also on capacity evolution, its variation does not seem to be related with capacity.

It would have been important to study cycling ageing of a larger sample of cells and over a higher cycle number in order to identify impedance evolution patterns common to several cells, allowing easily identifying when a certain cell presents a different behavior, either due to intrinsic characteristics of the cell or due to experimental errors. Unfortunately, the long cycling runtime and the lack of more equipment available made it impossible to cycle other new cells during the timeframe of this work.

5.1.2 Capacity and impedance analysis of a used cell

Figure 39 shows capacity evolution of a used cell over 50 charge-discharge cycles.

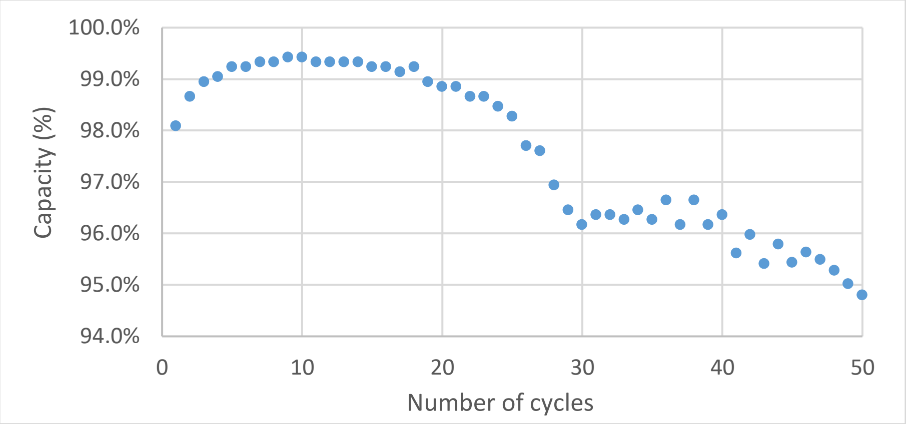

Figure 39: Capacity of a NCR18650 module cell over 50 charge-discharge cycles.

The used module cell presented less capacity variation in between consecutive cycles than the new cell, but about the same overall capacity loss of 5%. Capacity increases in the first 10 cycles, decreasing slowly between the 10th and the 20th cycles, followed by a significant decrease between the 20th and the 30th cycles. At this point, capacity increases slightly up to the 40th cycling, followed by a decrease until the 50th cycle.

Figures 40.a. and 40.b. show the Nyquist plots of a used cell at different charge states (after a complete charge and after every discharge step), for the 1st and the 50th cycles, respectively.

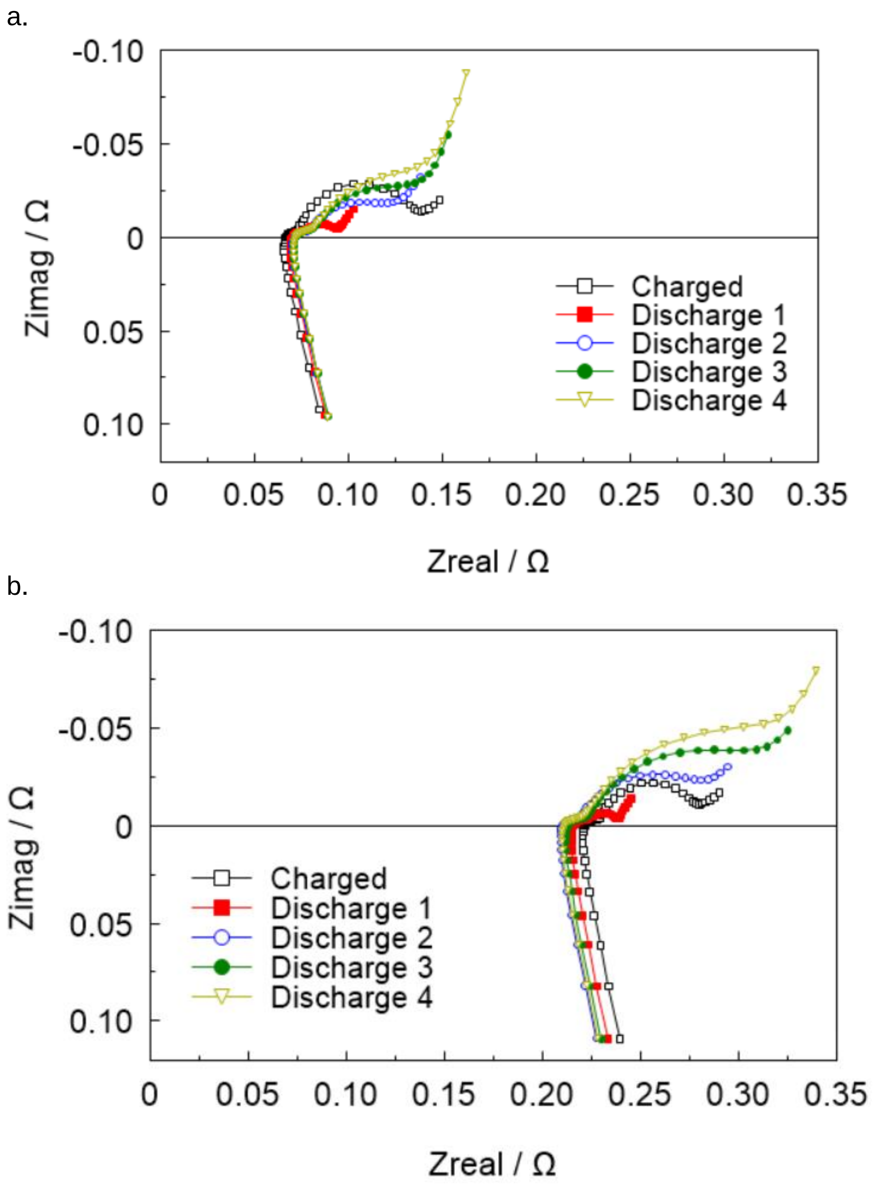

Figure 40: Full Nyquist plots of the used cell at different charge states in the a. 1st cycle; b. 50th cycle.

While a small increase in R_{int} can be verified during the 1st cycle, as the cell discharges, the same is not true for the 50th cycle, where R_{int} is the highest for the charged state.

To better visualize and compare impedance evolution over a single cycle, R_{int} of the Nyquist plots is subtracted.

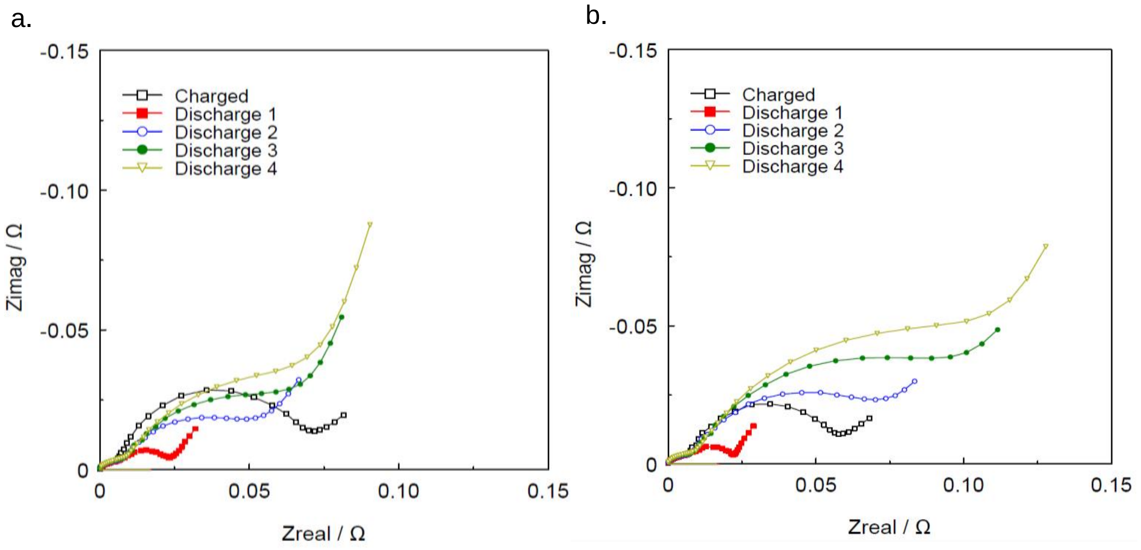

Figure 41: Nyquist plots of the used cell at different charge states in the a. 1st cycle; b. 50th cycle, with R_{int} moved to the origin of the coordinate system.

For both the 1st and the 50th cycles (Figure 41), there are no substantial changes in R_{SEI}. The second semicircle decreases considerably in the first discharge, compared to the fully charged state, and gets progressively larger as the discharge evolves. For both cycles, W_o increases as discharge evolves (lower SOC), but decreases at the last discharge stage.

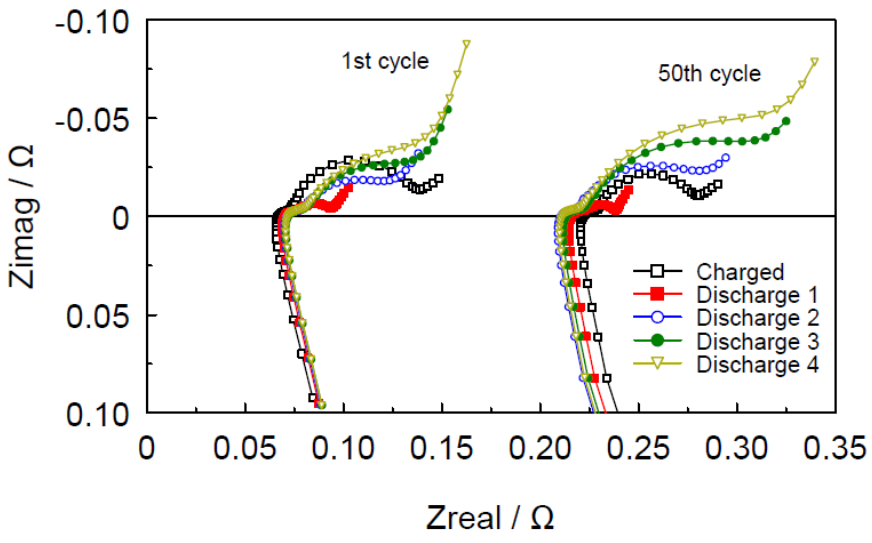

Figure 42: Nyquist plots of a used cell at different charge states for the 1st and 50th cycles.

Comparing the Nyquist diagrams of the first and last cycles (Figure 42), it is clear that R_{int} is the parameter which changes the most, increasing 237.8%. A more in depth look at R_{int} evolution with cycling can be found in Figure 43.

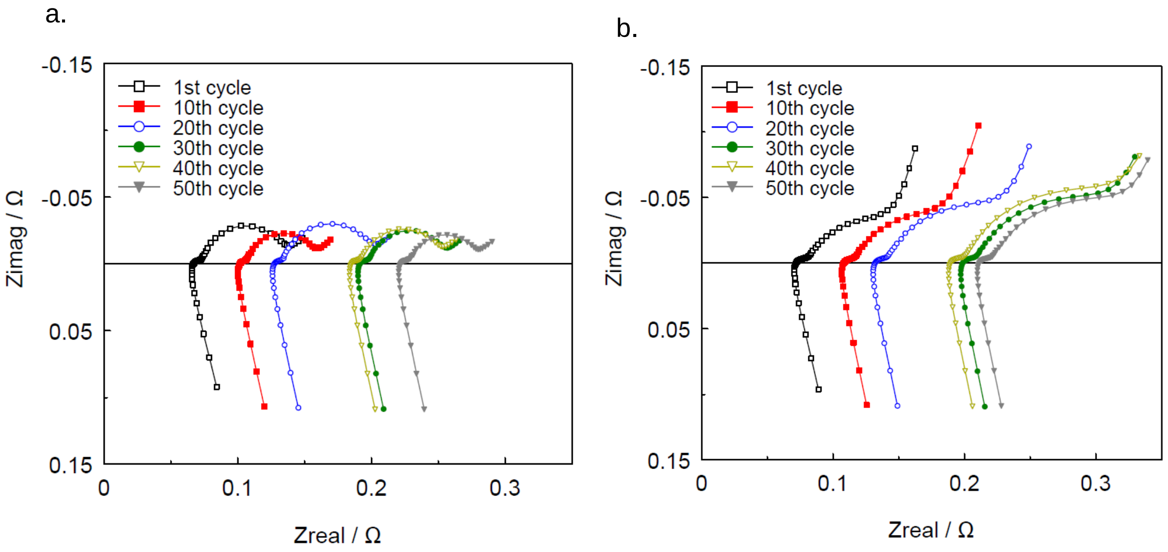

Figure 43: a. Nyquist plots of the charged used cell for every 10 cycles; b. Nyquist plots of the discharged used cell for every 10 cycles.

The Nyquist plots of the fully charged and discharged used cell reveal a continuous increase of R_{int}, except for the 40th cycle, which has a smaller R_{int} than the 30th cycle. A closer look is taken at R_{int} evolution between the 20th and 30th cycles and between the 30th and 40th cycles (Figure 44).

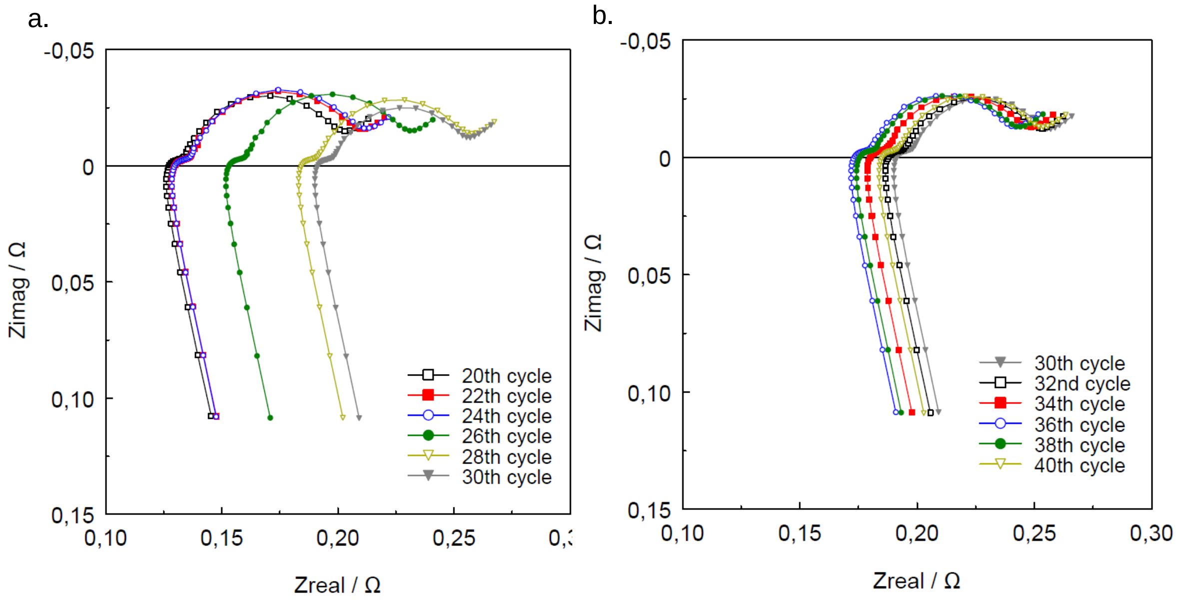

Figure 44: a. Impedance of a charged used cell between the 20th and 30th cycle; b. Impedance of a charged used cell between the 30th and the 40th cycle.

Figure 44 shows that R_{int} became much higher from the 24th to the 26th cycle, and from the 26th to the 28th cycle, increasing slightly until the 32nd cycle. Then, it decreases gradually until the 36th cycle, increasing from then on. The considerable R_{int} increase between the 24th to the 28th cycle was found to coincide with a considerable capacity drop, as well as the R_{int} decrease between the 32nd and the 36th cycle coincides with a capacity gain. From the 36th cycle onwards R_{int} increased, while capacity decreased. This finding reveals a significant relationship between capacity and internal resistance variation, suggesting that internal resistance may be a good parameter for SOH determination.

To analyse how the other parameters evolve with cycling, the charged-cell Nyquist plots' R_{int} for every 10 cycles are subtracted to all the spectra (Figure 45).

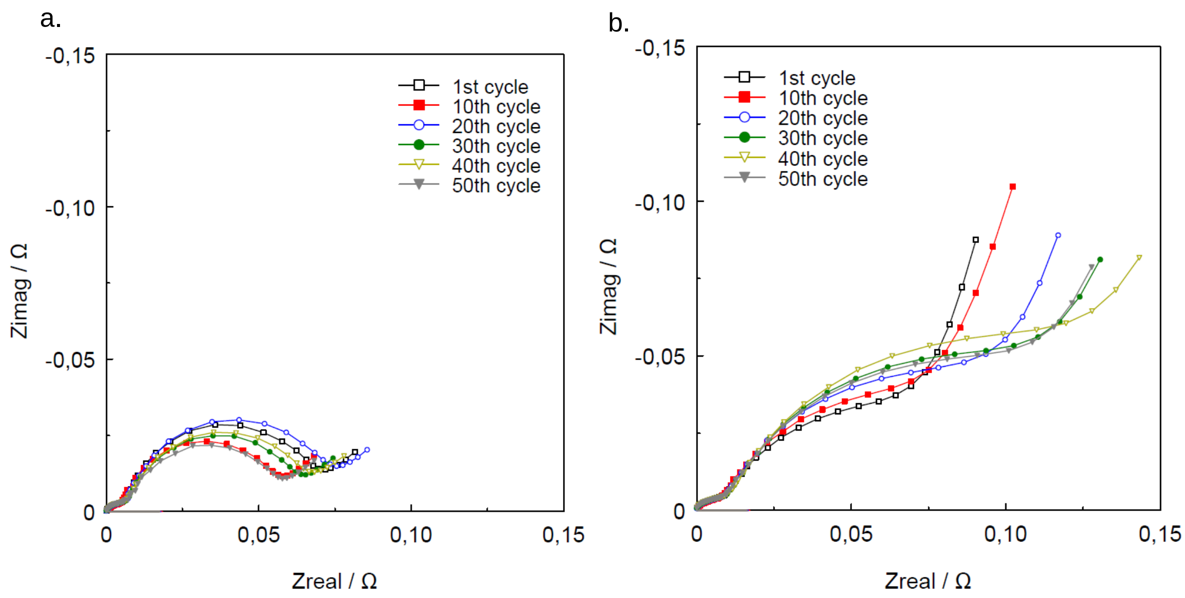

Figure 45: a. Nyquist plots of the charged used cell for every 10 cycles, moved to $R_{int} = 0\ \Omega$; Nyquist plots of the discharged used cell for every 10 cycles, moved to $R_{int} = 0\ \Omega$.

R_{SEI} shows a minimal variation with cycling. It is verified that R_{CT} does not increase regularly over cycling. In the charged state, it decreases from the 1st to the 10th cycle, increases until the 20th cycle and then tends to decrease until the 50th cycle, even though R_{CT} of the 40th cycle is slightly higher than in the 30th. As for the discharged state, it increases gradually and then decreases between the 40th and 50th cycles. R_{CT} variation was much more unstable than capacity evolution, and a correlation between both behaviors was not found. The charging profile of the cycles 45 to 50 presented some current and potential instability (Figure 46), which could be related to the decrease of R_{CT} between these cycles. However, no instability was found between the 1st and 10th cycles or between the 20th and the 30th cycles, where R_{CT} also decreased. W_o was found to vary irregularly, slightly decreasing over cycling, which was not expected. This behaviour was also reported by Krause et al. [27] and attributed to cathode particle cracking, which alters the diffusion path of the Li-ions. That could explain why this effect is only verified in the used cell, which suffered previous ageing.

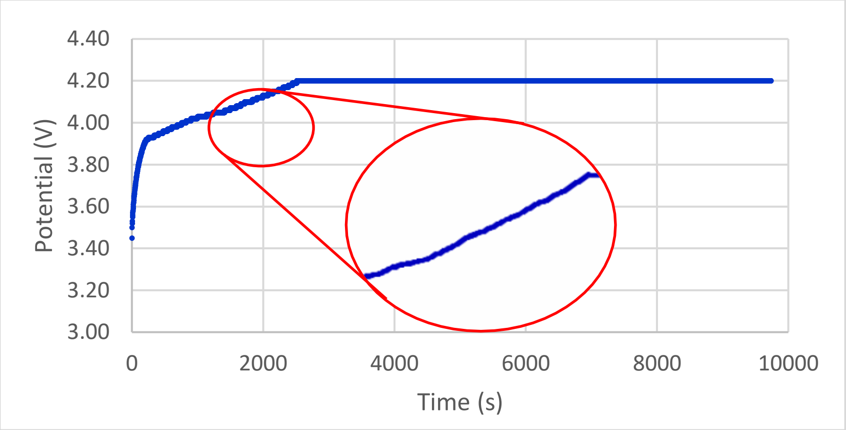

Figure 46: Voltage instability in a charge curve of the used cell (50th cycle).

Figure 47 represents the evolution of R_{int}, R_{SEI}, R_{CT} and W_o of the used cell at the charged state.

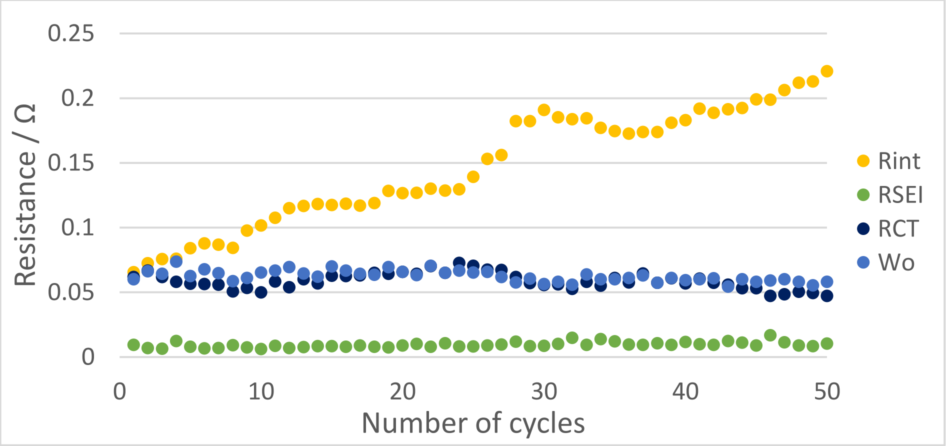

Figure 47: R_{int}, R_{SEI}, R_{CT} and W_o of the charged used cell over cycling.

Impedance analysis of the used cell allowed to verify once again that the different resistances that contribute to the total impedance do not necessarily increase for consecutive cycles. A decrease in R_{int} was found to coincide with a capacity gain and vice versa, except for the first 10 cycles, which may indicate a possible relationship between these two parameters. In the case of R_{CT} and W_o, the variation was very irregular and not so significant over the 50 cycles since these parameters vary mostly with SOC, and a relationship with capacity was not found, which suggests that these parameters are governed by quite complex mechanisms and several factors can influence the cell's dynamics in each cycle.

Just like it was mentioned previously, it would have been extremely useful to extend these studies to a larger number of cells, especially because in a used battery module it is expected that some cells have aged up to a larger extent than others. Once again, the required time to perform ageing studies reveals to be a major limitation.

Even though the new and the used cells are different in terms of rated capacity and specified cycling conditions, it is very clear that the overall impedance of the new cell is much lower than that of the used cell (Figure 48). Besides the used cell presented an initial R_{int} lower than the new cell, possibly related to contact resistance of the external circuit, this value increased much more for the used cell, confirming a certain level of previous cycling ageing.

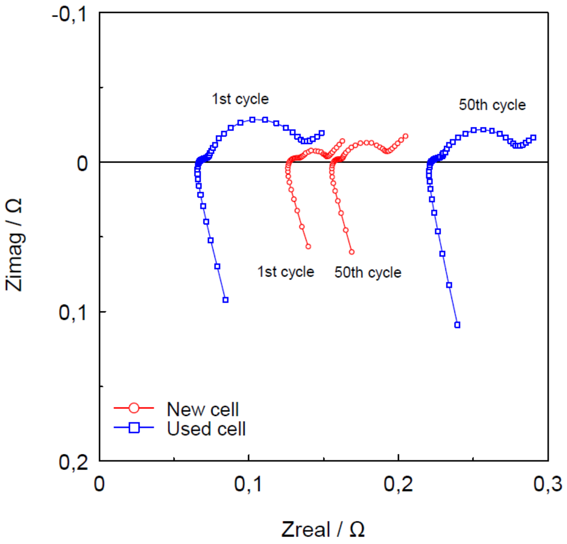

Figure 48: Nyquist diagrams in the charged state of new and used cells at the 1st and 50th charge-discharge cycle.

5.2 Capacity and impedance analysis of two parallel-connected cells

Capacity and impedance analysis are carried out for two parallel-connected cells, for both new and used cells.

5.2.1 Capacity and impedance analysis of two new cells

The capacity variation over cycling of two new cells connected in parallel is represented in Figure 49.

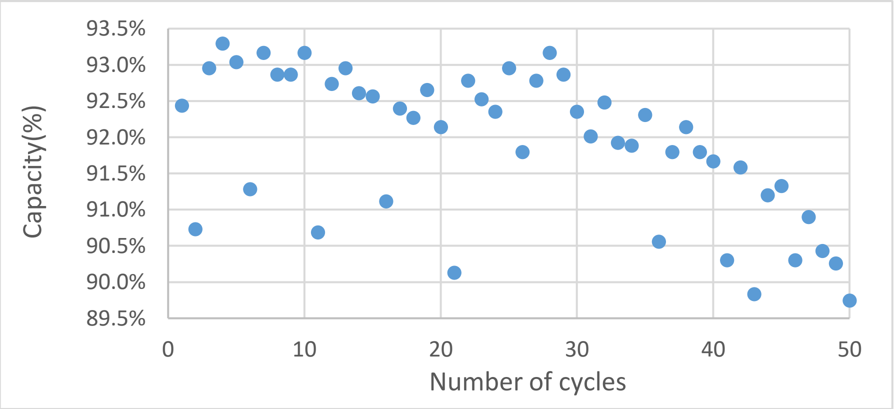

Figure 49: Capacity of two parallel-connected NCR18650B new cells over 50 charge-discharge cycles.

As cycling starts, the pair of new cells show a capacity of 92.5%, decreasing over cycling to about 89-90%. During the individual cycles performed to these two cells prior to connecting them in parallel, they revealed a capacity of 100% each, therefore they are not storing as much energy while parallel-connected than they did individually. This result could be related to the overpotentials caused by the experimental errors, such as unstable connection with the external current circuit, so the tests should be repeated as future work.

The sudden capacity drop verified for cycles 2, 6, 11, 16, 21, 26, 31, 36, 41 and 46 is explained by the fact that the cycle prior to each of them is a “long cycle”, where the discharge is done in four stages instead of one. After each discharge stage, the cell’s potential increases (stabilizes) during the rest period since the discharge current is high. Having some charge being recovered during the rest period after each discharge will result in needing less charge in the following cycle to fully charge the cell, which translates into a lower measured value of capacity. This effect promoted by a high discharge current highlights the influence that cycling conditions have on battery state determination.

For impedance analysis, an electric circuit representation of two cells in parallel would be as in Figure 50.

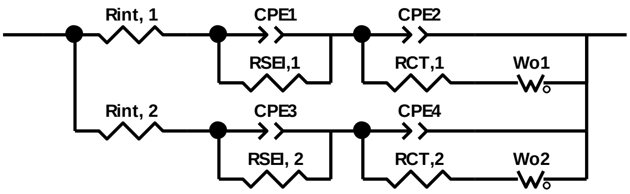

Figure 50: Electrical equivalent circuit for two cells in parallel.

However, this model has too many variables that cannot be readily identified in the impedance spectrum, besides the higher complexity of the model itself for data fitting. This issue would be even greater for more than two cells connected in parallel. Therefore, a simplified model is necessary for EEC analysis. In the literature, stacks of cells connected in parallel are analyzed with the EEC of an individual cell [8]. Even though mathematically the impedance of two cells in parallel would be half of the impedance of a single cell, physically this is not necessarily true for all the parameters of the EEC, especially for the second ZARC circuit, where there are elements in series inside a parallel branch. The EEC of a single cell, as described in 5.1, is used in this work to model two parallel-connected cells, having in mind that particularly in the second ZARC circuit the fitting results may not have the adequate physical meaning. This approach is selected for simplification purposes, already taking into account that R_{CT} and W_o do not seem to be the best parameters to represent the cell’s impedance or to correlate with capacity, as opposed to R_{int}, whose fitting results would not be affected by using this simplified model.

The Nyquist plots of the parallel-assembled new cells in the 1st and 50th cycles, at different charge states, are represented in Figure 51.

a.

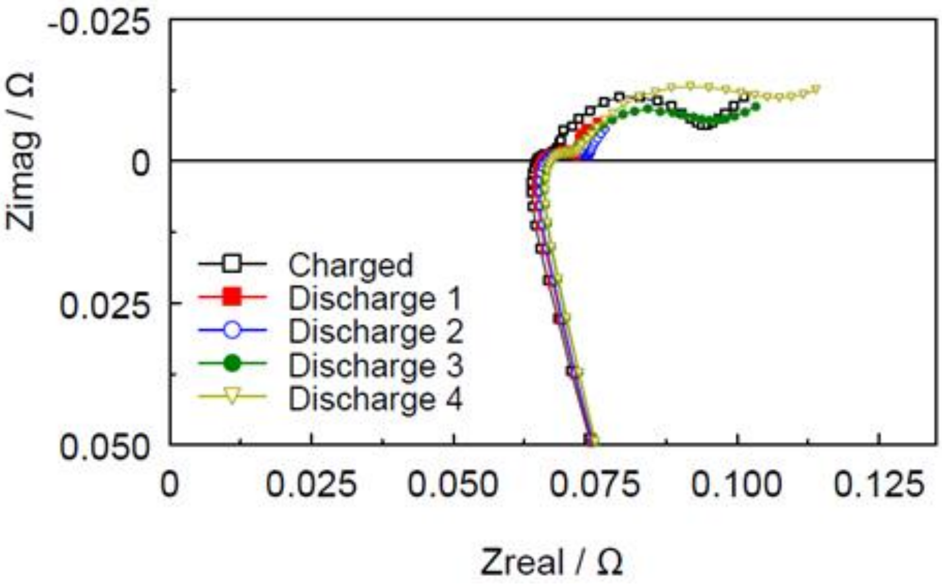

b.

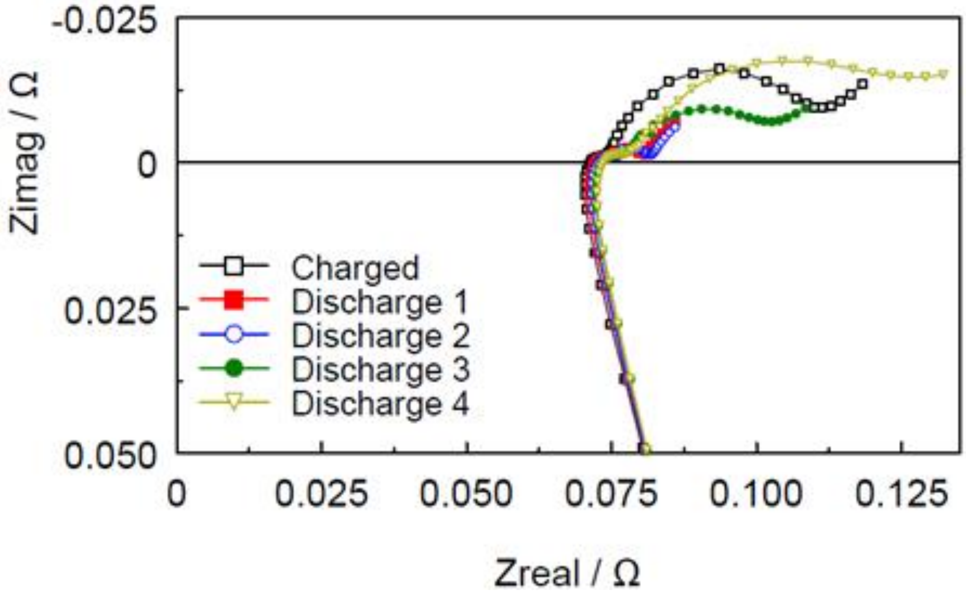

Figure 51: Full Nyquist plots of the two parallel-connected new cells at different charge states in the a. 1st cycle; b. 50th cycle.

Both the 1st and 50th cycles show a similar behavior. R_{int} increases slightly as SOC decreases and R_{SEI} does not show considerable changes. As for R_{CT}, it decreases strongly from the charged state to the first discharge, and increases gradually as the discharge progresses, as verified for individual cells. Warburg impedance increases for lower SOC.

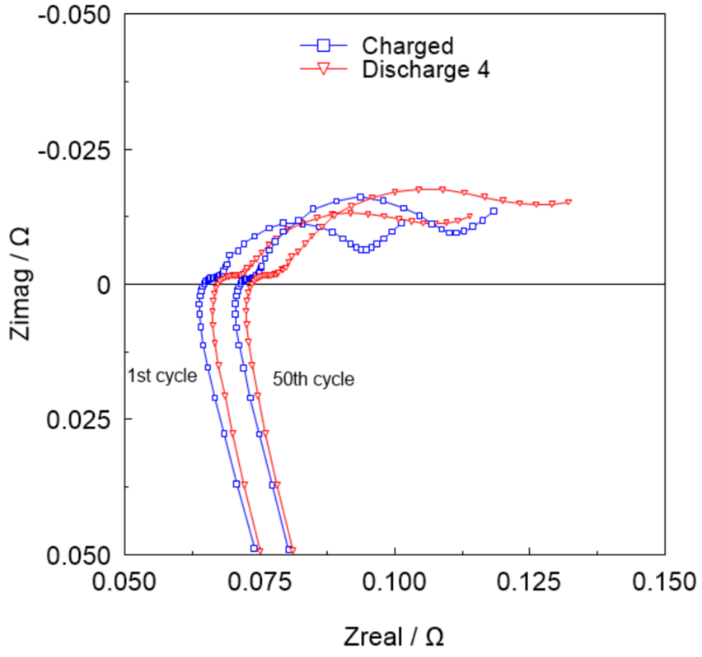

Figure 52: Nyquist plots of two new cells connected in parallel at the charged and discharged states for the 1st and 50th cycles.

Between the 1st and the 50th cycles an increase in R_{int} and R_{CT} is identified (Figure 52), but it is not as obvious as in the individual cells which parameter changes the most. A clarification on the weight of these parameters for the overall impedance is presented in section 5.3. For the charged state, R_{int} increased 10% over the 50 cycles.

Figure 53.a. shows the variation of R_{int} with cycling at the charged state, and in Figure 53.b. R_{int} is subtracted to all the Nyquist plots to compare the evolution of R_{CT}.

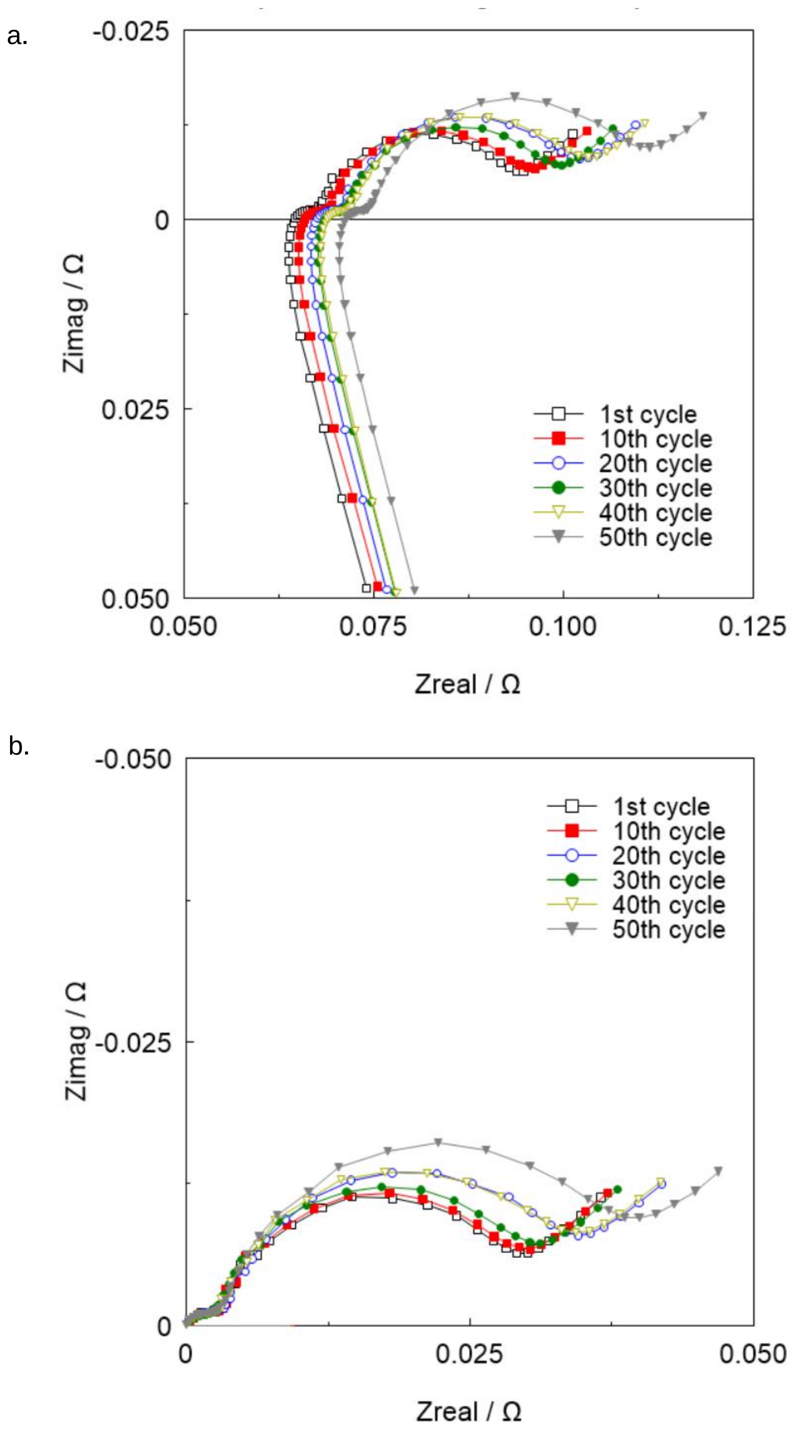

Figure 53: a. Impedance of two charged new cells connected in parallel for every 10 cycles; b. Impedance of charged new cells connected in parallel for every 10 cycles, moved to R_{int} = 0 Ω.

The cells in parallel show a similar behavior to the individual cells, with R_{int} increasing with cycling. R_{CT} tends to increase over cycling, but this increase is not significant and shows to be inconsistent, varying much more considerably with SOC. The same is verified for W_o.

5.2.2 Capacity and impedance analysis of two used cells

The capacity variation of two used cells during the 50 charge-discharge cycles is represented in Figure 54.

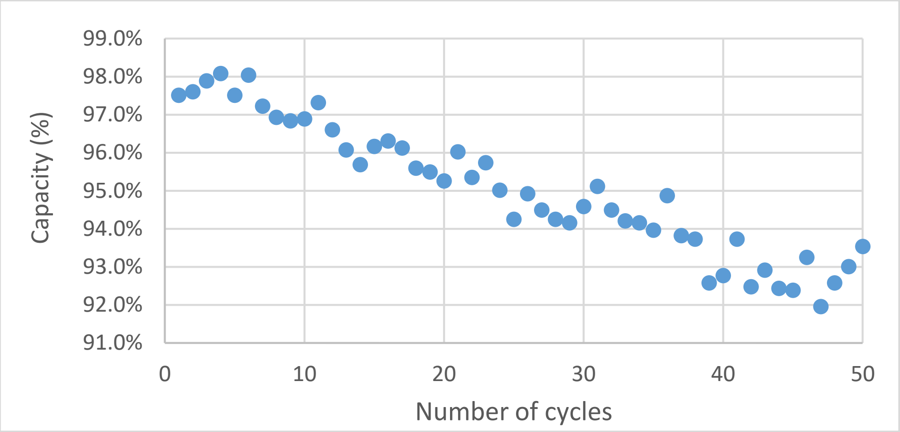

Figure 54: Capacity of two parallel-connected module used cells over 50 charge-discharge cycles.

During the 50 cycles, capacity decreases from 97.5% to 92-93% for the two module cells in parallel.

For impedance analysis, the same EEC used in 5.2.1 is applied for the used cells. The Nyquist plots of the parallel-assembled used cells in the 1st and 50th cycles, at different charge states, are represented in Figure 55.

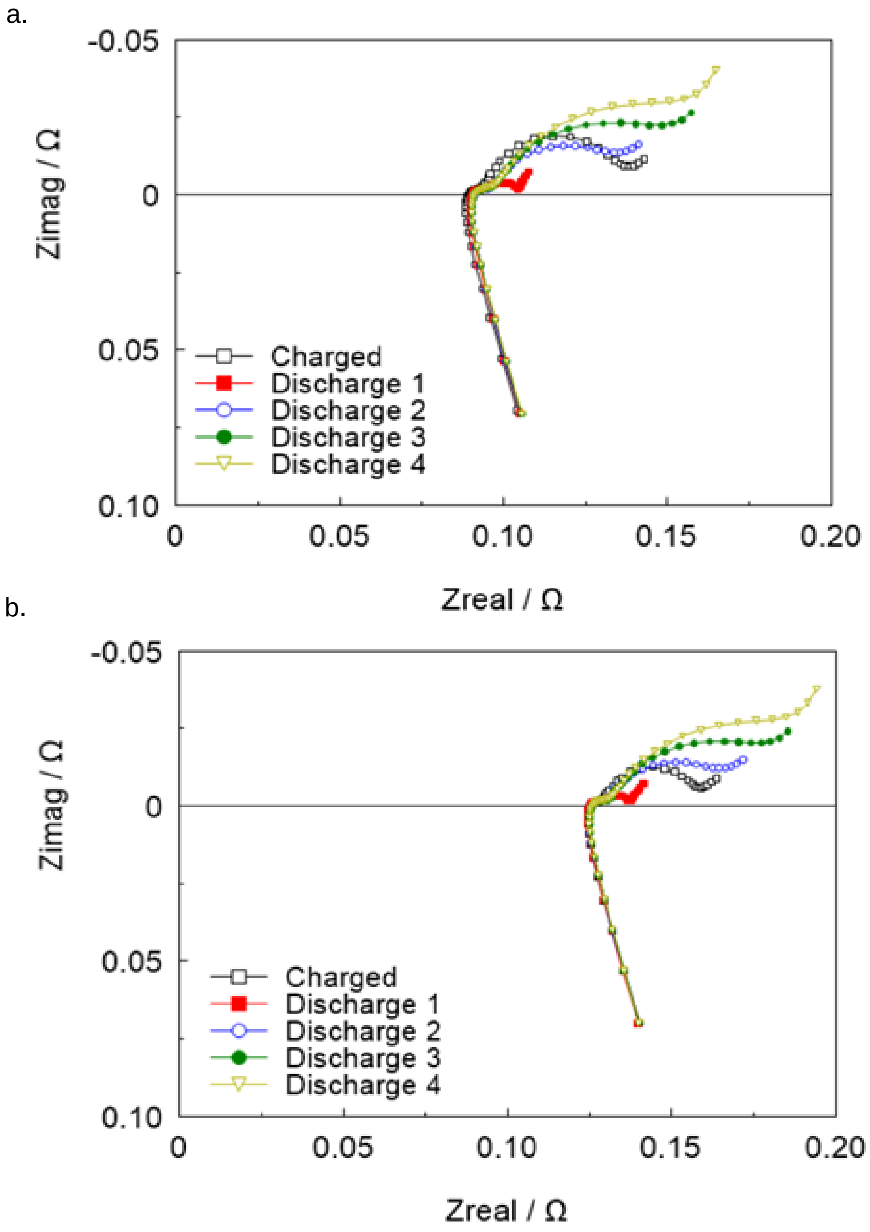

Figure 55: Full Nyquist plots of the two parallel-connected used cells at different charge states in the a. 1st cycle; b. 50th cycle.

The impedance of two used cells in parallel over a single cycle follows the same evolution as individual used cells. R_{int} shows a small increase as SOC decreases for both the 1st and the 50th cycles. R_{SEI} values do not vary significantly in a single cycle, while R_{CT} increases. W_o increases as discharge evolves (lower SOC), decreasing at the last discharge stage, for both cycles.

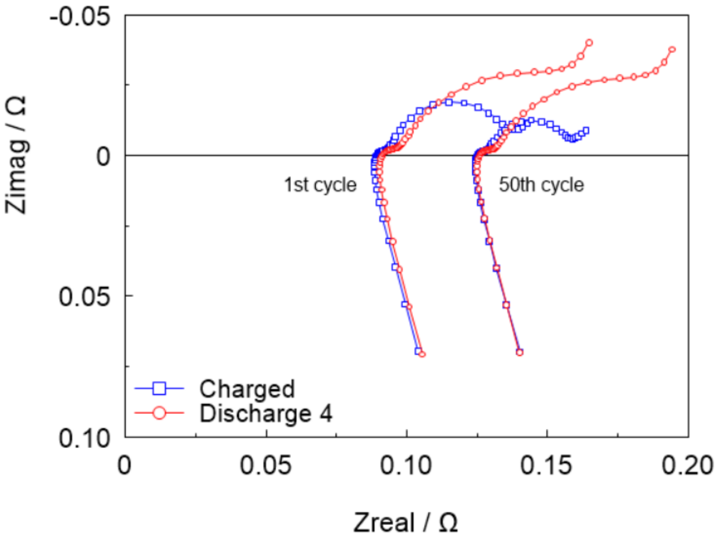

Figure 56: Nyquist plots of two used cells connected in parallel at the charged and discharged states for the 1st and 50th cycles.

By comparing the impedance of the totally charged and totally discharged used cells at the beginning and at the end of cycling (Figure 56), it is noticeable that R_{int} is again the parameter which changes the most, increasing 39.4%. A clear decrease of the second semicircle is also noted.

The evolution of the different resistances over cycling is analysed through the Nyquist diagrams of Figure 57.

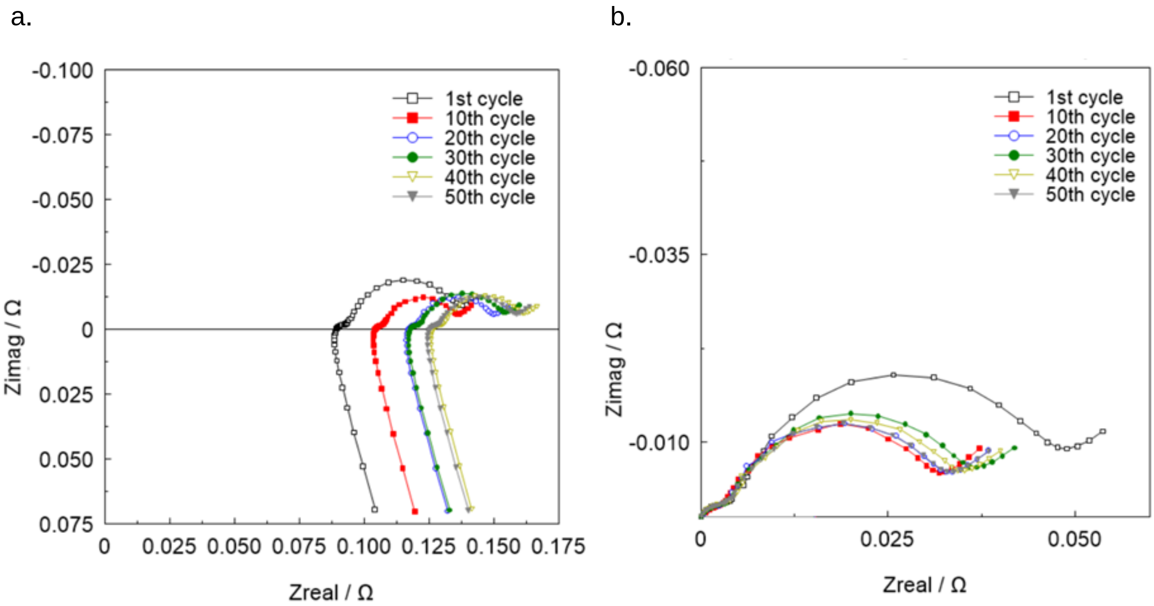

Figure 57: a. Impedance of two charged used cells connected in parallel for every 10 cycles; b. Impedance of charged used cells connected in parallel for every 10 cycles, moved to R_{int} = 0 Ω.

It was verified that R_{int} increases over cycling, even though it is slightly lower in the 50th cycle than in the 40th. Capacity varies more irregularly but with a decreasing tendency, increasing only in the last 4 cycles, which coincides with the overall increase in R_{int}, except for the last cycles, when it decreases. R_{SEI} does not present any substantial variation during cycling and R_{CT} is the highest in the 1st cycle, showing an irregular variation from the 10th cycle onwards. W_o shows a small decrease over the 50 cycles. R_{CT} and W_o show to vary much more with SOC than with cycling.

5.3 SOH definition based on resistance

The total resistance of a cell comprises R_{int}, R_{SEI}, R_{CT} and W_o, each of them representing a different contribution. To evaluate the weight of each of these resistances, their evolution over cycling was compared with the evolution of |Z| at the lowest frequency, for new and used charged cells. R_{int} at the discharged state was also compared, to understand if the weight of R_{int} on the total impedance is dependent on the charge state.

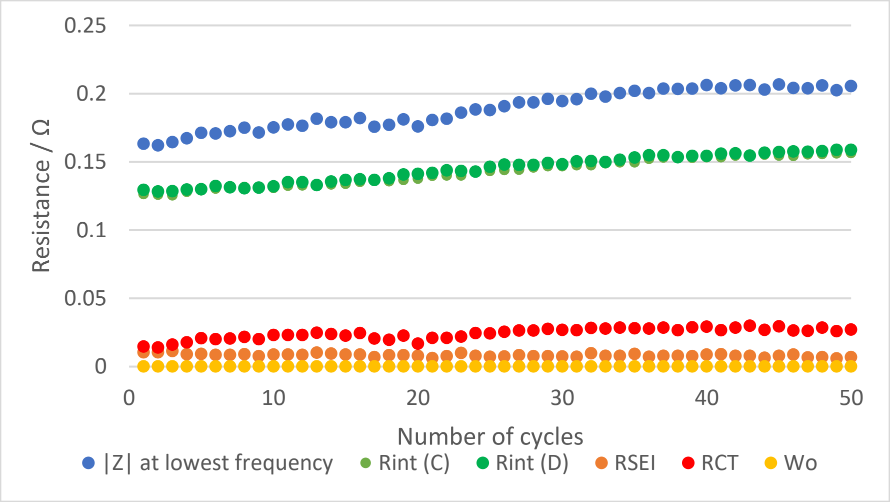

Figure 58: Evolution of R_{int} of the new charged and discharged cell, R_{int}(C) and R_{int}(D), respectively, R_{SEI}, R_{CT}, W_o and |Z| of the new cell at charged state with cycling.

R_{int} of the new cell at the fully charged state reveals to contribute the most to the overall impedance modulus of the cell (Figure 58). R_{int} at the discharged state is very close to R_{int} at the charged state, which reveals that this parameter is the one which most contributes to |Z| regardless of the SOC. Thus, SOH determination based on internal resistance has the advantage that it can be calculated at any SOC.

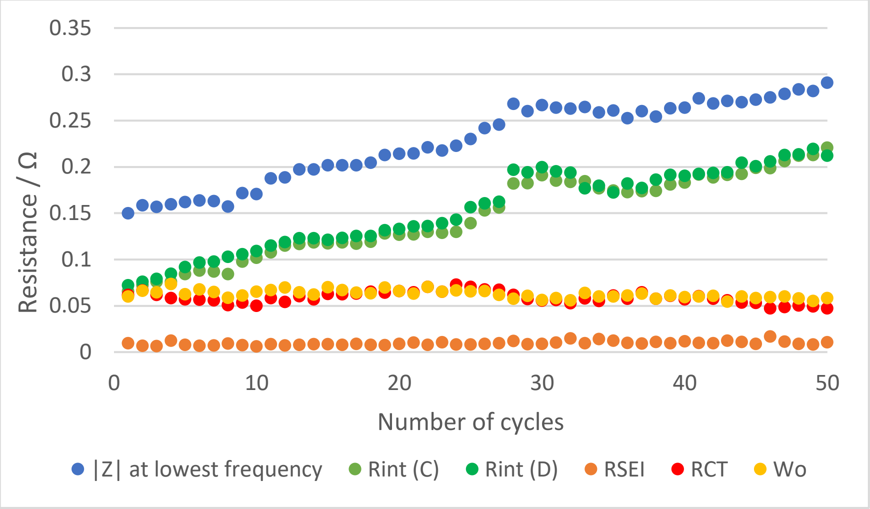

Figure 59: Evolution of R_{int} of the used charged and discharged cell, $R_{int}(C)$ and $R_{int}(D)$, respectively, R_{SEI}, R_{CT}, W_o and |Z| of the used cell at charged state with cycling.

The same is verified for the used cell (Figure 59), with R_{SEI}, R_{CT} and W_o having a smaller influence on |Z| than R_{int}.

Therefore, it is possible to conclude that while R_{SEI} shows little variation and R_{CT} and W_o change mostly with SOC, R_{int} is the parameter whose evolution is the most dependent on the number of cycles, being its variation directly related to battery ageing.

The same evaluation is carried out for the two new cells connected in parallel (Figure 60).

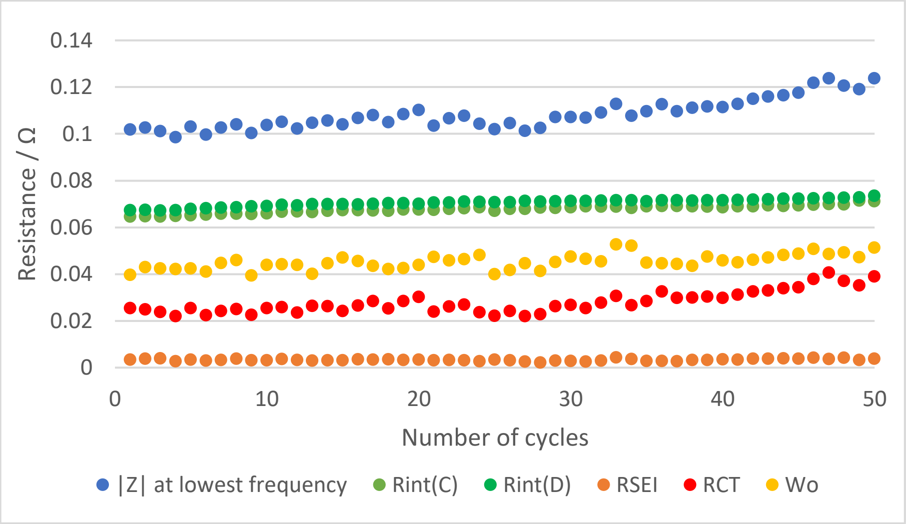

Figure 60: Evolution of R_{int} of the new charged and discharged cells, $R_{int}(C)$ and $R_{int}(D)$, respectively, R_{SEI}, R_{CT}, W_o and |Z| of the two new parallel-connected cells at charged state with cycling.

Regarding the new parallel-connected cells, R_{int} is still the resistance which mostly contributes to the impedance modulus, even though the other resistances show a larger contribution for the parallel-connected cells than for the individual cell. The values of R_{int} for the new cells in parallel are approximately half of R_{int} of the individual cells, which is in accordance with equation (26), indicating that each one of the cells tested in parallel had about the same initial internal resistance as the tested individual new cell.

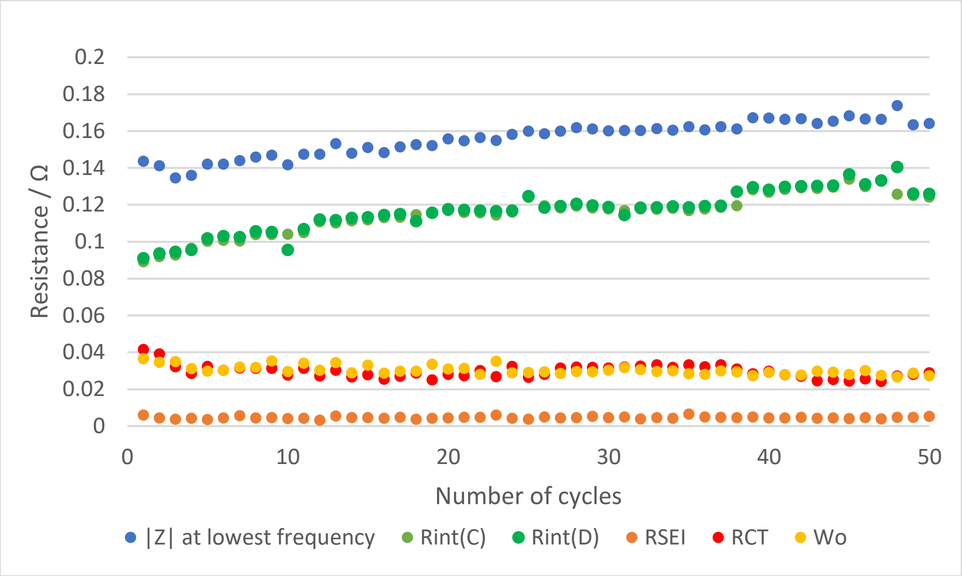

Figure 61: Evolution of R_{int} of the used charged and discharged cell, $R_{int}(C)$ and $R_{int}(D)$, R_{SEI}, R_{CT}, W_o and |Z| of the two used parallel-connected cells at charged state with cycling.

The impedance modulus of the used cells in parallel also revealed to be mostly influenced by R_{int}. In this case, the internal resistance of the two cells in parallel is not half of the resistance of the individual cell that was tested, and a much lower internal resistance increase of 34.9% was verified, compared to an increase of 237.8% for the individual cell. This reinforces the idea that the cells in an EV battery are often subjected to different conditions, resulting in having a module with cells with different SOH.

Since the internal resistance was found to be the parameter which is the most dependent on the number of cycles for both individual and parallel-connected cells, it is assessed whether there is a direct correlation between R_{int} increase and the loss of capacity. Figures 62 and 63 represent the variation of capacity and R_{int} with cycling to the new and used cell, respectively.

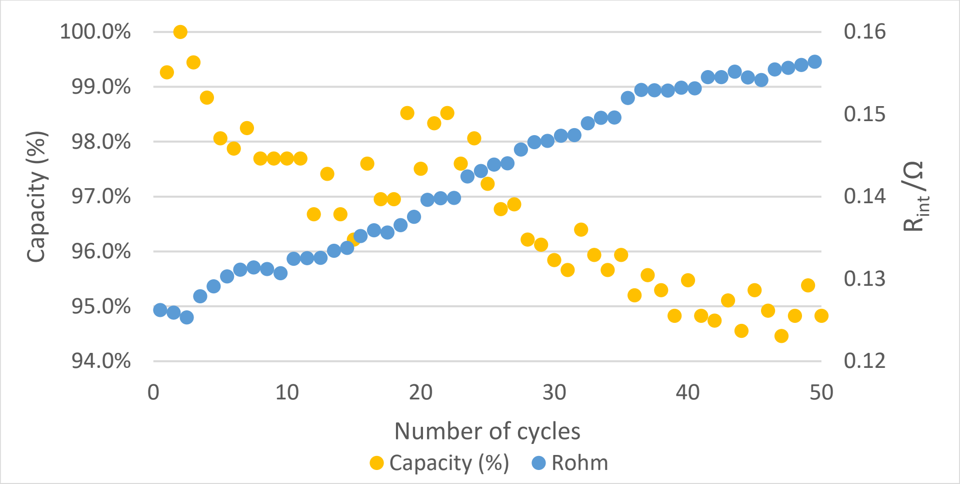

Figure 62: Capacity and R_{int} variation of a new charged cell over cycling.

In the case of the new cell, capacity has a decreasing tendency, except in between the 15th and the 20th cycles, while R_{int} keeps increasing over the 50 cycles.

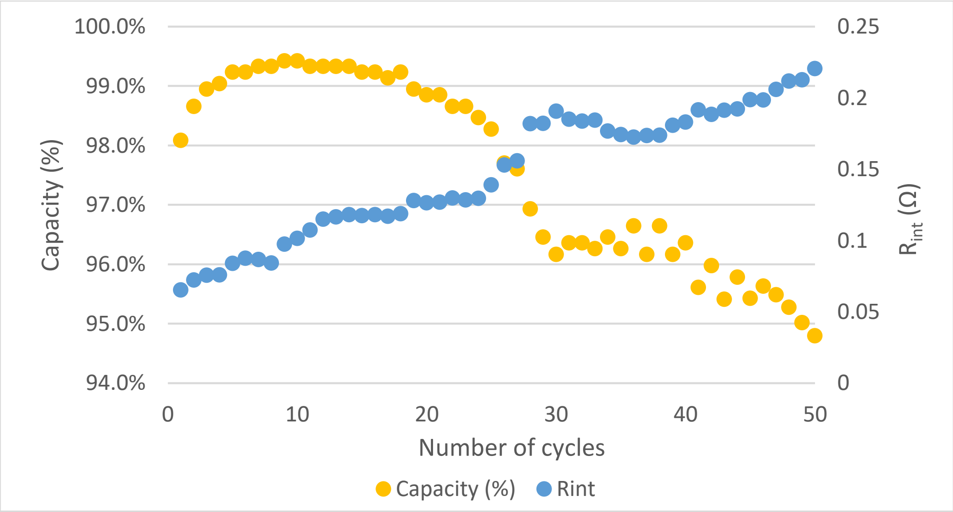

Figure 63: Capacity and R_{int} variation of a used charged cell with cycling.

Except for the first 10 cycles, where both capacity and R_{int} increase, these two parameters show an opposite behavior, with R_{int} increasing when capacity decreases and vice versa.

The same correlation is studied for the new and used cells in parallel (Figures 64 and 65, respectively).

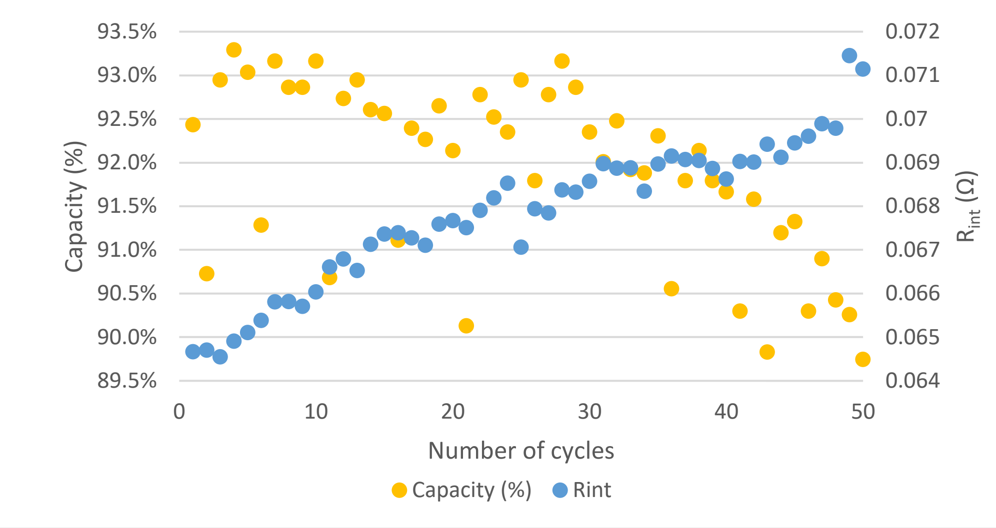

Figure 64: Capacity and R_{int} variation of two new cells connected in parallel with cycling.

Figure 64 shows capacity and R_{int} having a very irregular variation, thus it is not possible to directly find a correlation between the two parameters.

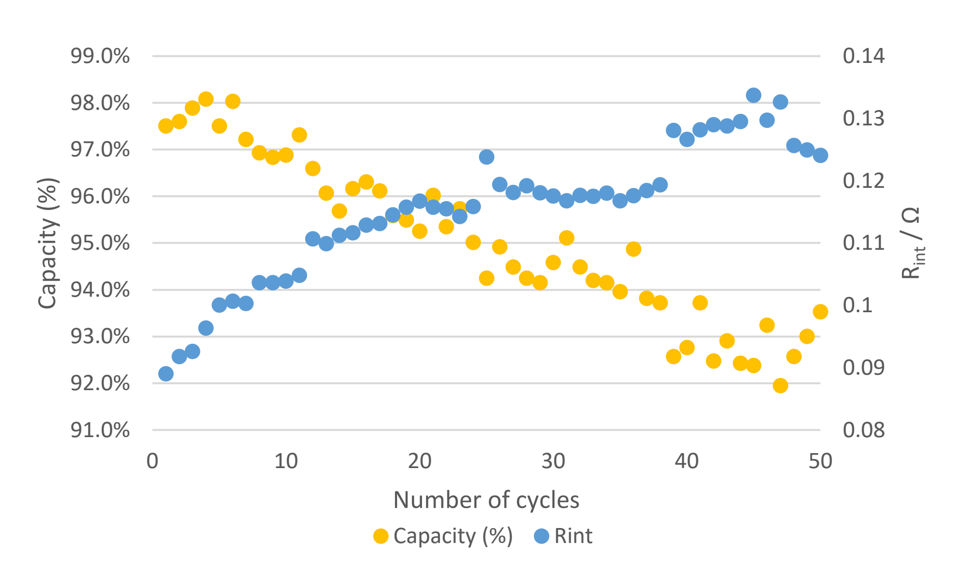

Figure 65: Capacity and R_{int} variation of two used cells connected in parallel with cycling.

Overall, the parallel association of used cells (Figure 65) presents an increase of R_{int} with cycling, accompanied by a decrease in capacity. In the last four cycles, capacity increases while R_{int} decreases.

These results show a certain relationship between the variations in capacity and internal resistance, suggesting that resistance-based SOH determination may have a correlation with capacity-based SOH determination.

In order to ascertain whether there may be a correlation between the capacity-based and resistance-based definitions of SOH, it is important to understand the meaning of both concepts.

According to the capacity-based definition of SOH applied in this work (SOH_C), the moment when the battery in an electric vehicle is replaced corresponds to a SOH of 80%, while according to the resistance-based definition of SOH, this moment corresponds to a SOH of 0%.

Therefore, an alternative definition based on resistance is proposed. Instead of the value $R_{int,subs}$, the internal resistance when the battery is replaced, it is used the value $R_{int,EOL}$, corresponding to the internal resistance of the battery when it dies, i.e. to the end-of-life of the battery, which is the moment when the SOH is considered 0%. State-of-health is defined as 80% at the moment when the battery is replaced.

Considering this, the challenge is to estimate $R_{int,EOL}$ (internal resistance when SOH is 0%) as a function of $R_{int,NEW}$ to use in SOH calculation. Furthermore, the goal is to find whether there is a correlation between SOH calculated based on capacity and SOH determination based on internal resistance.

The estimation of $R_{int,EOL}$ is done based on the resistance-based battery replacement criteria. Since a battery must be replaced when its internal resistance doubles, i.e., when $R_{int} = 2R_{int,NEW}$, and considering that at that moment the SOH is 80%, then $R_{int,EOL}$ can be calculated as follows:

$$SOH = \frac{R_{int,EOL} - R_{int}}{R_{int,EOL} - R_{int,NEW}} \times 100\% \Longrightarrow 0.80 = \frac{R_{int,EOL} - 2\,R_{int,NEW}}{R_{int,EOL} - R_{int,NEW}} \Longrightarrow R_{int,EOL} = 6\ R_{int,NEW} \qquad (31)$$

Therefore, SOH determination based on this criterion, SOH_2, can be calculated as:

$$SOH_2 = \frac{R_{int,EOL} - R_{int}}{R_{int,EOL} - R_{int,NEW}} \times 100\% = \frac{6\,R_{int,NEW} - R_{int}}{6\,R_{int,NEW} - R_{int,NEW}} \times 100\% = \frac{6\,R_{int,NEW} - R_{int}}{5\,R_{int,NEW}} \times 100\% \qquad (32)$$

SOH_C and SOH_2 are compared for each tested cell/set of cells in Figure 66.

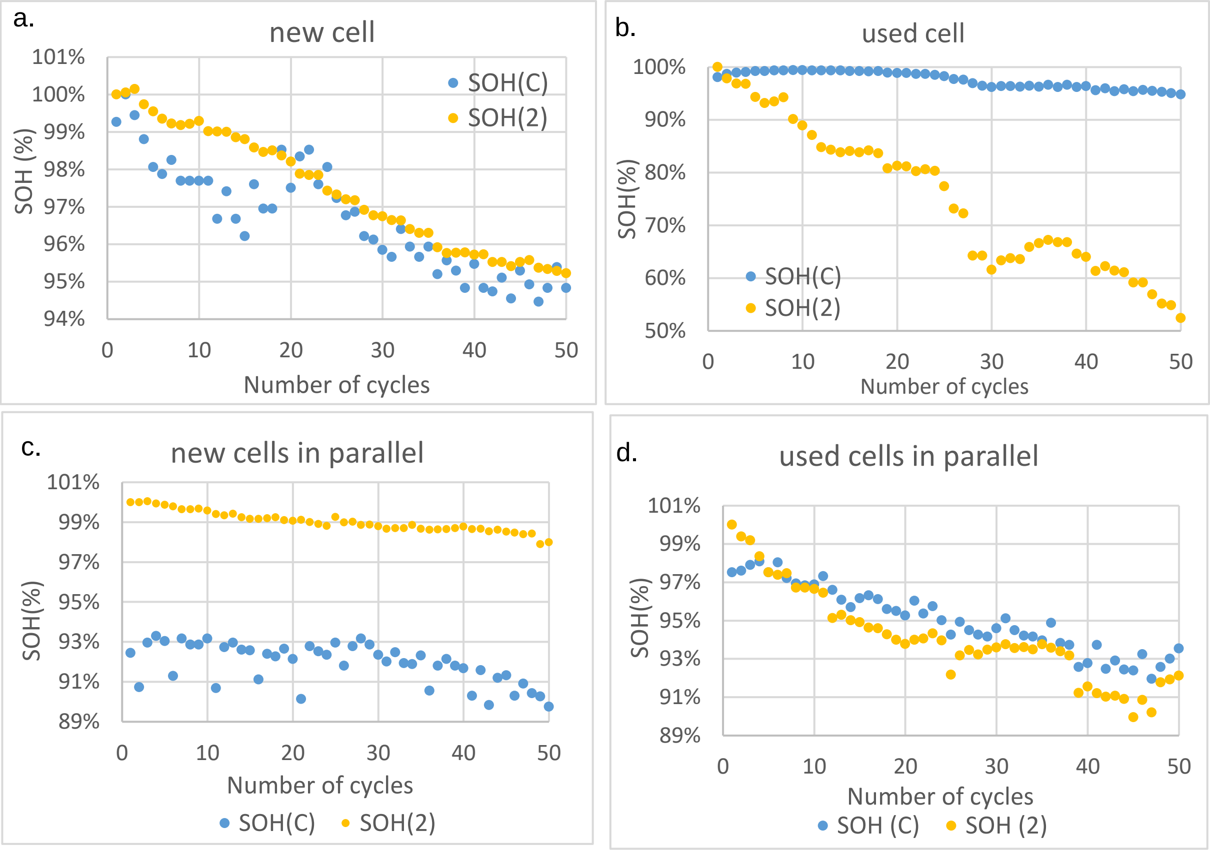

Figure 66: SOH calculated based on capacity, SOH(C) and based on resistance replacement criteria, SOH(2) for a. the new cell; b. the used cell; c. the parallel-connected new cells; d. the parallel-connected used cells.

SOH_C and SOH_2 seem to have a reasonable correlation in the case of the new cell and in the case of the association of two used cells in parallel, suggesting that achieving 80% of the rated capacity may coincide to reaching about twice the rated internal resistance, even though 80% of the capacity was not achieved over only 50 cycles. In the case of the used cell, these two definitions of SOH do not seem to be related, as capacity decreases much less than internal resistance increases. For the association of two new cells in parallel, the SOH values calculated based on capacity and internal resistance are very different. The rated internal resistance of lithium-ion cells is usually given by the manufacturer, but in the case of these two cell models this value is not given. Thus, $R_{int,NEW}$ was considered to be the internal resistance measured in the first cycle. That value is considered to be the internal resistance at a SOH of 100%, which is not true, because in this case capacity shows to be at about 92% in the first cycle, which explains why there is such a difference between SOH_C and SOH_2. However, both SOH_C and SOH_2 show to have a similar profile (SOH_2 having a more regular evolution), suggesting that if the rated internal resistance value had been used for SOH_2 calculation, there could have been a correlation between both definitions.

The advantage of this approach to calculate SOH based on internal resistance replacement criteria is that the relationship $R_{int,EOL} = f \cdot R_{int,NEW}$ is fixed for all lithium-ion cell types, meaning that SOH_2 can be easily estimated as long as $R_{int,NEW}$ is specified by the manufacturer.

However, for the used cell, this approach does not correlate with SOH$_C$. Thus, it was intended to determine a value $R_{int,EOL}$ which, if used in SOH calculation based on resistance, would allow approximating to SOH$_C$. $R_{int,EOL}$ is defined as a function of $R_{int,NEW}$, so that $R_{int,EOL} = f \cdot R_{int,NEW}$. SOH based on resistance, calculated with this new $R_{int,EOL}$ value, is determined and defined as SOH$_R$. Using the tool *Solver* in *Microsoft Excel*, it was calculated the parameter f for the relationship $R_{int,EOL} = f \cdot R_{int,NEW}$, by establishing that the SOH$_R$ of the last cycle should equal the SOH$_C$ of the last cycle: $SOH_{R,at\ the\ 50th\ cycle} = SOH_{C,at\ the\ 50th\ cycle}$. This was done for all the tested cells, in order to understand what is the value f that best approximates SOH$_C$ to SOH$_R$. $R_{int,NEW}$ was considered the value obtained for each test in the first cycle.

The parameter f calculated for the new cell is 5.62, therefore $R_{int,EOL.new\ cell} = 5.62 \cdot R_{int,NEW,new\ cell}$ and for the used cell is 46.73, so $R_{int,EOL,used\ cell} = 46.73 \cdot R_{int,NEW,used\ cell}$.

For the two new cells in parallel, f is 1.97 so $R_{int,EOL.new\ cells\ //} = 1.97 \cdot R_{int,NEW,new\ cells\ //}$, and for the two used cells in parallel f is 7.09, so $R_{int,EOL.used\ cells\ //} = 7.09 \cdot R_{int,NEW,used\ cells\ //}$.

Thus, SOH$_R$ is calculated as follows:

$$SOH_{R,new\ cell} = \frac{R_{int,EOL} - R_{int}}{R_{int,EOL} - R_{int,NEW}} \times 100\% = \frac{5.62\ R_{int,NEW} - R_{int}}{5.62\ R_{int,NEW} - R_{int,NEW}} \times 100\% = \frac{5.62\ R_{int,NEW} - R_{int}}{4.62\ R_{int,NEW}} \times 100\% \quad (33)$$

$$SOH_{R,used\ cell} = \frac{R_{int,EOL} - R_{int}}{R_{int,EOL} - R_{int,NEW}} \times 100\% = \frac{46.73\ R_{int,NEW} - R_{int}}{46.73\ R_{int,NEW} - R_{int,NEW}} \times 100\% = \frac{46.73\ R_{int,NEW} - R_{int}}{45.73\ R_{int,NEW}} \times 100\% \quad (34)$$

$$SOH_{R,new\ cells\ //} = \frac{R_{int,EOL} - R_{int}}{R_{int,EOL} - R_{int,NEW}} \times 100\% = \frac{1.97\ R_{int,NEW} - R_{int}}{1.97\ R_{int,NEW} - R_{int,NEW}} \times 100\% = \frac{1.97\ R_{int,NEW} - R_{int}}{0.97\ R_{int,NEW}} \times 100\% \quad (35)$$

$$SOH_{R,used\ cells\ //} = \frac{R_{int,EOL} - R_{int}}{R_{int,EOL} - R_{int,NEW}} \times 100\% = \frac{7.09\ R_{int,NEW} - R_{int}}{7.09\ R_{int,NEW} - R_{int,NEW}} \times 100\% = \frac{7.09\ R_{int,NEW} - R_{int}}{6.09\ R_{int,NEW}} \times 100\% \quad (36)$$

The only disadvantage of calculating SOH based on internal resistance through EIS tests is that those values require an EEC to be obtained, even though other techniques could be used to readily obtain internal resistance values. Alternatively, the impedance modulus |Z| can be obtained by EIS without the need for an EEC. SOH was then calculated using |Z| (SOH$_Z$) instead of the internal resistance, to understand how this alternative correlates with SOH$_C$.

As done for SOH$_R$, using the *Solver* tool, the parameter f is obtained for the relationship $|Z|_{EOL} = f \cdot |Z|_{NEW}$, where |Z| is the impedance modulus at the lowest frequency. $|Z|_{NEW}$ was considered the value obtained for each test in the first cycle.

It was found that for the tested new cell, f is equal to 6.01, therefore $|Z|_{EOL,new\ cell} = 6.01 \cdot |Z|_{NEW,new\ cell}$, and for the used cell f is equal to 20.30, so $|Z|_{EOL,used\ cell} = 20.30 \cdot |Z|_{NEW,used\ cell}$.

For the parallel connected new cells, f is equal to 3.09, so $|Z|_{EOL,new\ cells\ //} = 3.09 \cdot |Z|_{NEW,new\ cells\ //}$, and for the used cells in parallel it is 3.21, so $|Z|_{EOL,used\ cells\ //} = 3.21 \cdot |Z|_{NEW,used\ cells\ //}$.

SOH$_Z$ is calculated as follows:

$$SOH_{Z,new\ cell} = \frac{|Z|_{EOL} - |Z|}{|Z|_{EOL} - |Z|_{NEW}} \times 100\% = \frac{6.01\ |Z|_{NEW} - |Z|}{6.01\ |Z|_{NEW} - |Z|_{NEW}} \times 100\% = \frac{6.01\ |Z|_{NEW} - |Z|}{5.01\ |Z|_{NEW}} \times 100\% \quad (37)$$

$$SOH_{Z,used\ cell} = \frac{|Z|_{EOL} - |Z|}{|Z|_{EOL} - |Z|_{NEW}} \times 100\% = \frac{20.30\,|Z|_{NEW} - |Z|}{20.30\,|Z|_{NEW} - |Z|_{NEW}} \times 100\% = \frac{20.30\,|Z|_{NEW} - |Z|}{20.30\,|Z|_{NEW}} \times 100\% \quad (38)$$

$$SOH_{Z,new\ cells\ //} = \frac{|Z|_{EOL} - |Z|}{|Z|_{EOL} - |Z|_{NEW}} \times 100\% = \frac{3.09\,|Z|_{NEW} - |Z|}{3.09\,|Z|_{NEW} - |Z|_{NEW}} \times 100\% = \frac{3.09\,|Z|_{NEW} - |Z|}{2.09\,|Z|_{NEW}} \times 100\% \quad (39)$$

$$SOH_{Z,used\ cells\ //} = \frac{|Z|_{EOL} - |Z|}{|Z|_{EOL} - |Z|_{NEW}} \times 100\% = \frac{3.21\,|Z|_{NEW} - |Z|}{3.21\,|Z|_{NEW} - |Z|_{NEW}} \times 100\% = \frac{3.21\,|Z|_{NEW} - |Z|}{2.21\,|Z|_{NEW}} \times 100\% \quad (40)$$

The main disadvantage of this approach is that the impedance modulus of the cell as new is not currently given by the manufacturer.

SOH_C (SOH estimation based on capacity fade), SOH_2, SOH_R and SOH_Z were estimated for the new and the used cell and represented in Figures 67 and 68, respectively.

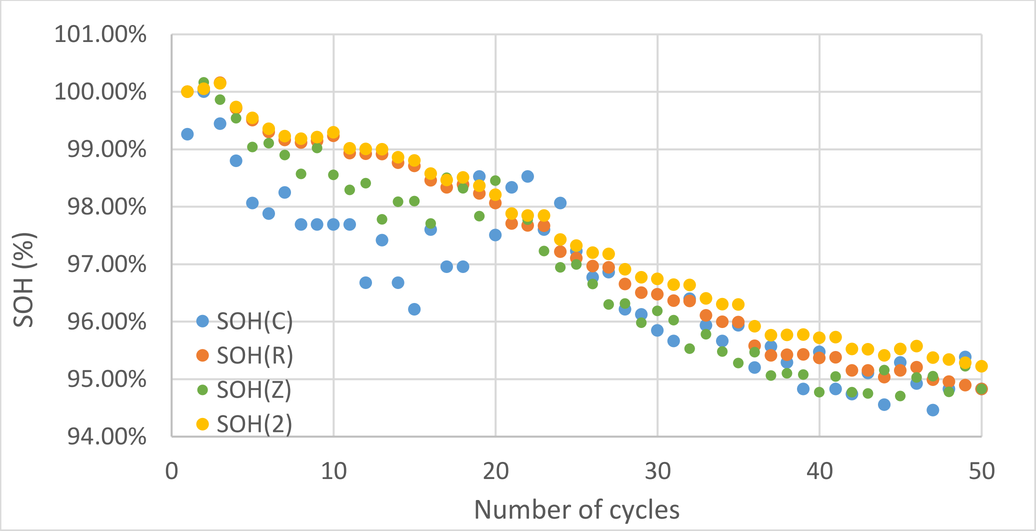

Figure 67: SOH of the new cell calculated based on capacity, SOH(C), internal resistance, SOH(R), impedance modulus at the lowest frequency, SOH(Z), and battery replacement criteria, SOH(2).

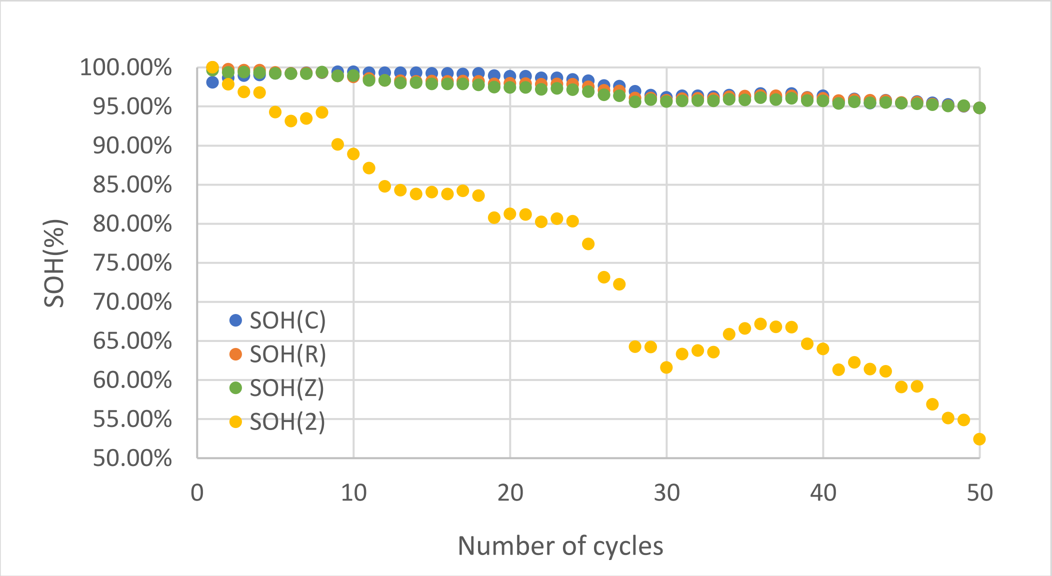

Figure 68: SOH of the used cell calculated based on capacity, SOH(C), internal resistance, SOH(R), impedance modulus at the lowest frequency, SOH(Z), and battery replacement criteria, SOH(2).

Figure 67 reveals that the different approaches selected for SOH estimation of the new cell show a reasonable correlation with SOH based on capacity (SOH_C). In fact, the factor f calculated for SOH based on internal resistance and impedance modulus was found to be very close to 6, as in the theoretical approach. This suggests that SOH determination based on capacity can be related to SOH determination based on internal resistance, in this case. SOH_Z seems to be the approach which better approximates to SOH_C, by following the most accentuated capacity variations especially in the first half of the cycles, but for the second half of the cycles the approach based on resistance (SOC_R) is also a good approximation.

Regarding the used cell (Figure 68), the first approach, based on replacement criteria, shows very different SOH values compared to SOH_C, presenting a SOH_2 of 52% when the SOH_C remains at 95%, due to the fact that the cell's capacity decreased very little over 50 cycles, while the internal resistance increased dramatically. The other two alternative SOH determination approaches are compared to SOH_C in Figure 69.

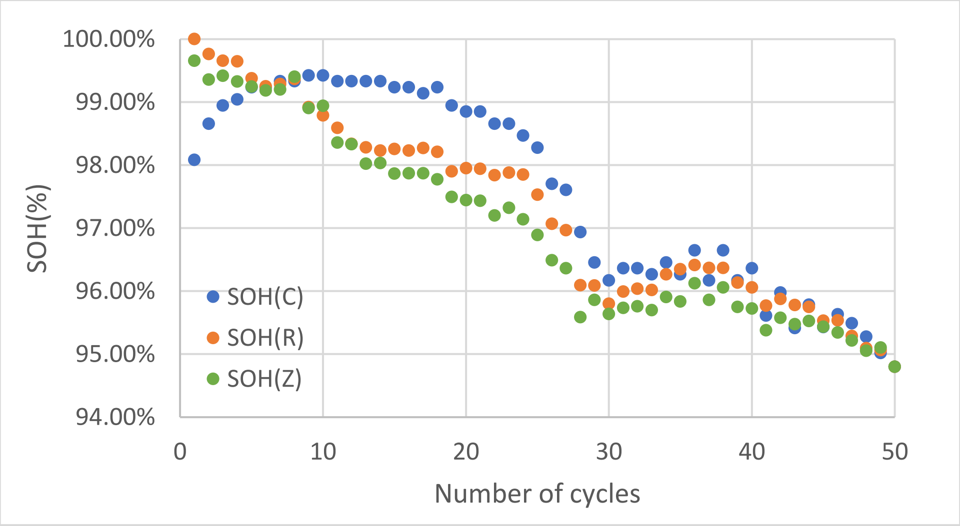

Figure 69: SOH of the used cell calculated based on capacity, SOH(C), internal resistance, SOH(R), and impedance modulus at the lowest frequency, SOH(Z).

In this case, SOH_R is the approach that mostly approximates to SOH_C, even though SOH_Z still shows a reasonable correlation. The determined f factor in SOH_R has a significant difference from the theoretical one (f = 6), being 46.73 in $R_{int,EOL} = f \cdot R_{int,NEW}$.

SOH estimation for the two cells connected in parallel is shown in Figure 70.

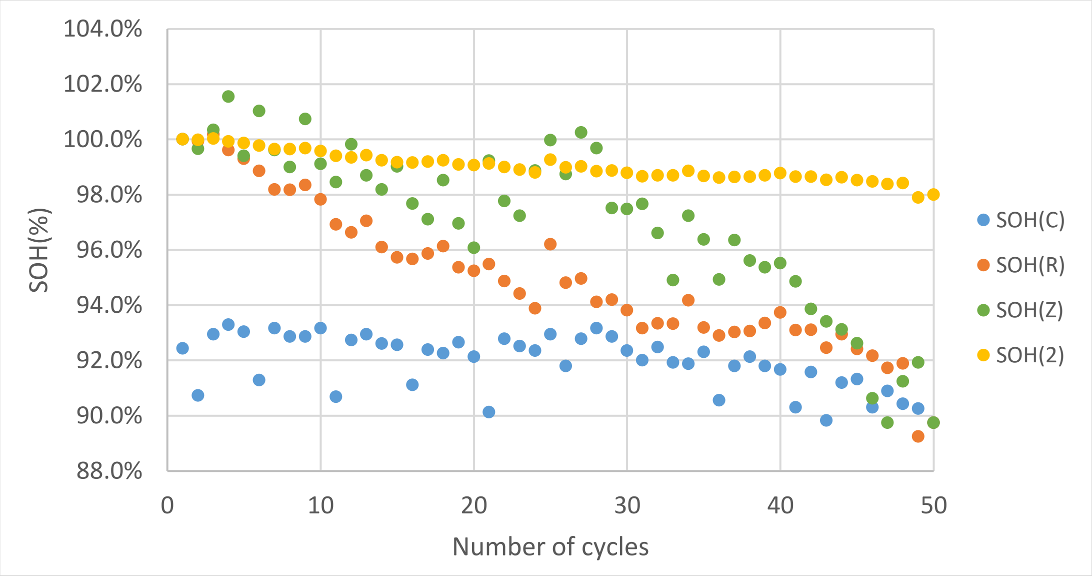

Figure 70: SOH of the two new cells in parallel, calculated based on capacity, SOH(C), internal resistance, SOH(R), impedance modulus at the lowest frequency, SOH(Z) and battery replacement criteria, SOH(2).

In this case, none of the approaches showed a good correlation with SOH estimation based on capacity, which is explained by the need to use the R_{int} and |Z| values of the first cycle as the $R_{int,NEW}$ and $|Z|_{NEW}$ values, since these are not given by the manufacturer. Using these values results in a SOH of 100% in the first cycle, while the SOH based on capacity was 92.4% in the first cycle.

Figure 71 represents the SOH estimation for the two used cells in parallel.

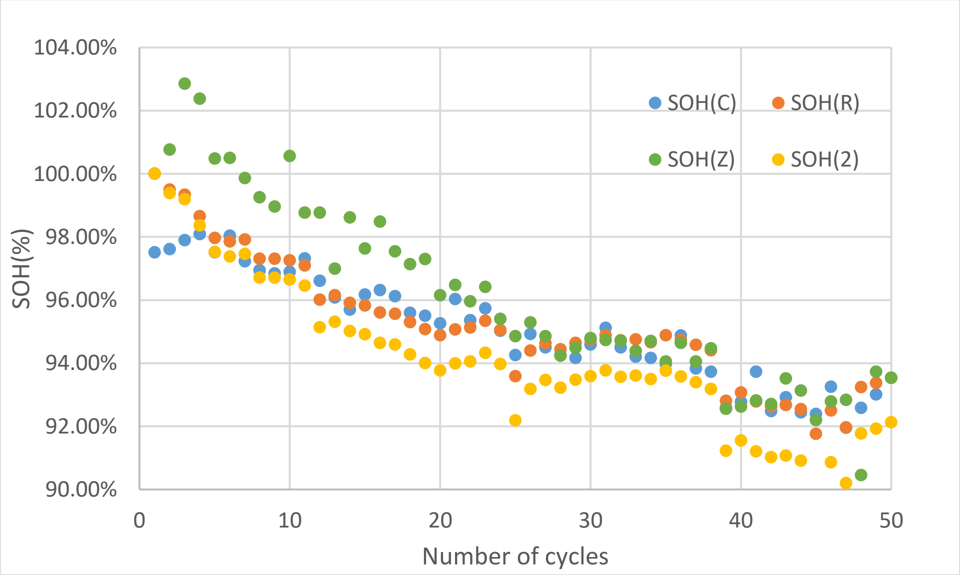

Figure 71: SOH of the two used cells in parallel, calculated based on capacity, SOH(C), internal resistance, SOH(R), impedance modulus at the lowest frequency, SOH(Z) and battery replacement criteria, SOH(2).

For the two used cells in parallel, SOH_R shows to be the best approximation to the values of SOH_C, with a factor f of 7.09 in $R_{int,EOL} = f \cdot R_{int,NEW}$.

The results of the individual cells and of the two used cells in parallel show that there may be a correlation between SOH_C and SOH based on resistance or impedance. None of the batteries reached 80% of its rated capacity during the 50 cycles, therefore it would have been useful to study cell ageing over a higher number of cycles, to compare capacity and resistance evolution.

SOH_Z and SOH_R, based on impedance modulus and internal resistance, respectively, revealed to be the best approximations to SOH_C for the new cell, while SOH_R better approximates SOH_C for the used battery. SOH_R was also the best approximation for the two parallel-connected used cells. Since SOH_Z estimation is a more complicated approach because initial impedance values are not given by the manufacturer, it is possible to see SOH_R as a potential method to estimate SOH based on resistance and have a reasonable correlation with capacity variation.

According to the results, in order to have a correlation between SOH_R and SOH_C for both the new and the used cell, the factor f in $R_{int,EOL} = f \cdot R_{int,NEW}$ had to be significantly different between the two cases, meaning that $R_{int,EOL}$ would be related to $R_{int,NEW}$ in a different way for the two cells. While the factor f for the new cell is close to the one determined by battery replacement criteria, for the used cell this value is very different. It is important to remember that besides their ageing, these cells are of different models, therefore it is expected that they have different characteristics and behavior, and they might have different $R_{int,NEW}$ values. With this in mind, it would be interesting to verify at which extent the battery replacement criteria $R_{int} = 2R_{int,NEW}$ is adequate for all types of lithium-ion cells. Since different cells may have different compositions and characteristics, it would be reasonable to consider that they could have different replacement criteria and different $R_{int,EOL}$ in relationship with $R_{int,NEW}$. SOH_2 determination has a fixed f value of 6, implying that $R_{int,EOL} = 6 \cdot R_{int,NEW}$ is valid for all types of Li-ion cells. While having this fixed value can be helpful in terms of generalization, and a reasonable approximation to most of the values that were determined in this work, finding the exact value for each cell model would allow for a more accurate SOH determination and a better correlation with SOH_C. In that case, if this type of study was previously made by the manufacturers, they could provide a value of $R_{int,EOL}$ in function of $R_{int,NEW}$, value at which the cell would be approximately reaching its end-of-life for both resistance and capacity thresholds.

The factor f in $R_{int,EOL} = f \cdot R_{int,NEW}$ was also found to be different in the cases of one individual used cell and two parallel-connected used cells. This factor is much larger for the individual cell ($f = 46.73$), which shows an extremely high increase of R_{int} during cycling, than for the association of used cells in parallel, where the factor f is 7.09, closer to the theoretical value. It is unclear if this high increase of R_{int} for the individual cell is solely related to extreme and abnormal power fade of that specific cell or if any experimental errors may have affected the measurements. Therefore, studying the hypothesis of $R_{int,EOL} = f \cdot R_{int,NEW}$ having a different f value for each cell type would require performing cycling tests to a larger number of cells of the module to verify if overall they show similar f values, identifying and eliminating any case of possible experimental errors. Nevertheless, the f factor calculated for the used parallel-connected cells was different than 6, which also suggests that by having a $R_{int,EOL}$ specific for each cell model, a better correlation between SOH_C and SOH determination based on internal resistance could be achieved.

Therefore, an underpinned study on this possible correlation requires a much larger sample of cells to be studied, of different characteristics, as well as a larger number of cycles.

6 Conclusions

This work allowed contributing to a better understanding of the ageing mechanisms governing lithium-ion cells by means of capacity and impedance analysis through charge-discharge tests and Electrochemical Impedance Spectroscopy.

EIS tests revealed that overall impedance increases with cycling, but this evolution is not linear, and some decreases can occur. Furthermore, some of these changes might only be perceived after a large number of cycles, meaning that 50 cycles are insufficient for a complete ageing study and longer tests should be done.

It was verified that the internal resistance is indeed the parameter that contributes most significantly to the impedance modulus, both for the individual and parallel-connected cells. In addition, unlike R_{SEI}, which does not show significant variation over the number of cycles selected for this study, and R_{CT} and W_o, which vary mostly with SOC, R_{int} changes mostly with the number of cycles, being therefore considered a good indicator of cell ageing to be used in SOH determination.

SOH was estimated based on the condition that a battery should be replaced when its internal resistance doubles, and assuming that in that moment the SOH is 80%. The internal resistance value when the battery's SOH is 0% was determined as $R_{int,EOL} = 6\ R_{int,NEW}$. This SOH determination method was found to approximate reasonably to SOH_C for the individual new cell and for the parallel-connected new cells and used cells, but not for the individual used cell. Thus, a factor f in the relationship $R_{int,EOL} = f \cdot R_{int,NEW}$ that better approximates to SOH_C was determined and SOH_R was calculated using that factor for each test. The same was done by using the impedance modulus |Z| at the lowest frequency instead of R_{int} in order to have an alternative that does not require an EEC. The factor f was calculated and SOH_Z with that factor f was determined.

SOH_R revealed to be the most approximate estimation approach to SOH_C, and it implies that different cell types would have different internal resistance values corresponding to the moment when the cell dies, $R_{int,EOL}$, as function of the initial internal resistance of the cell, $R_{int,NEW}$, which is reasonable to consider since different cell types can have different initial resistance values and ageing behavior.

In any case, it is important to emphasize that extended tests, in terms on number of cells and number of cycles, would be necessary to have a complete analysis of capacity and impedance evolution with cycling, as well as to study the relationship between internal resistance increase and capacity fade, and to conclude on a suitable SOH determination method based on resistance.

6.1 Future Work

As a continuation of this work, it becomes important to extend the charge-discharge and EIS tests to a larger number of cells, in order to verify the results obtained for a single cell and to identify possible errors associated with experimental conditions.

Additionally, it would also be useful to subject the cells to a greater number of cycles, or even cycling them until failure, to obtain more information about the evolution of capacity and impedance of the cell over its entire life. This would also allow an estimate of the internal resistance of the cell at the time of failure, which could be useful in ascertaining the feasibility of the methods presented in this study for impedance-based SOH calculation.

Moreover, in order to study the applicability of impedance-based SOH for diagnostics of complete electric vehicle battery modules or cell stacks, it would be important to extend these studies to multiple cells connected both in series and in parallel.

References

[1] B. Dunn, H. Kamath, and J.-M. Tarascon, “Electrical Energy Storage for the Grid: A Battery of Choices,” *Science (1979)*, vol. 334, pp. 928–935, 2011, doi: 10.1126/science.1212741.

[2] L. A. W. Ellingsen, G. Majeau-Bettez, B. Singh, A. K. Srivastava, L. O. Valøen, and A. H. Strømman, “Life Cycle Assessment of a Lithium-Ion Battery Vehicle Pack,” *J Ind Ecol*, vol. 18, no. 1, pp. 113–124, 2014, doi: 10.1111/jiec.12072.

[3] Gamry Instruments, “Testing Lithium-Ion Batteries.” Application note. https://www.gamry.com/application-notes/battery-research/testing-lithium-ion-batteries/ (accessed Apr. 2, 2022).

[4] I. Energy Agency, “Global EV Outlook 2022 Securing supplies for an electric future,” 2022. https://www.iea.org/reports/global-ev-outlook-2022/ (accessed Sep. 16, 2022).

[5] I. Energy Agency, “Global EV Outlook 2021: Accelerating ambitions despite the pandemic,” 2021. https://www.iea.org/reports/global-ev-outlook-2021/ (accessed Sep. 16, 2022).

[6] S. Sharma, A. K. Panwar, and M. M. Tripathi, “Storage technologies for electric vehicles,” *Journal of Traffic and Transportation Engineering (English Edition)*, vol. 7, no. 3. Chang’an University, pp. 340–361, Jun. 01, 2020. doi: 10.1016/j.jtte.2020.04.004.

[7] M. Murnane and A. Ghazel, “A Closer Look at State of Charge (SOC) and State of Health (SOH) Estimation Techniques for Batteries.”

[8] C. Pastor-Fernández, K. Uddin, G. H. Chouchelamane, W. D. Widanage, and J. Marco, “A Comparison between Electrochemical Impedance Spectroscopy and Incremental Capacity-Differential Voltage as Li-ion Diagnostic Techniques to Identify and Quantify the Effects of Degradation Modes within Battery Management Systems,” *J Power Sources*, vol. 360, pp. 301–318, 2017, doi: 10.1016/j.jpowsour.2017.03.042.

[9] P. Iurilli, C. Brivio, and V. Wood, “On the use of electrochemical impedance spectroscopy to characterize and model the aging phenomena of lithium-ion batteries: a critical review,” *Journal of Power Sources*, vol. 505. Elsevier B.V., Sep. 01, 2021. doi: 10.1016/j.jpowsour.2021.229860.

[10] S. Castano-Solis, D. Serrano-Jimenez, L. Gauchia, and J. Sanz, “The influence of BMSs on the characterization and modeling of series and parallel Li-ion packs,” *Energies (Basel)*, vol. 10, no. 3, 2017, doi: 10.3390/en10030273.

[11] M. A. Hannan, M. M. Hoque, A. Hussain, Y. Yusof, and P. J. Ker, “State-of-the-Art and Energy Management System of Lithium-Ion Batteries in Electric Vehicle Applications: Issues and Recommendations,” *IEEE Access*, vol. 6. Institute of Electrical and Electronics Engineers Inc., pp. 19362–19378, Mar. 20, 2018. doi: 10.1109/ACCESS.2018.2817655.

[12] N. S. Zhai, M. W. Li, W. L. Wang, D. L. Zhang, and D. G. Xu, “The application of the EIS in Li-ion batteries measurement,” *J Phys Conf Ser*, vol. 48, no. 1, pp. 1157–1161, Oct. 2006, doi: 10.1088/1742-6596/48/1/215.

[13] A. Barai *et al.*, “A comparison of methodologies for the non-invasive characterisation of commercial Li-ion cells,” *Progress in Energy and Combustion Science*, vol. 72. Elsevier Ltd, pp. 1–31, May 01, 2019. doi: 10.1016/j.pecs.2019.01.001.

[14] M. M. Thackeray, C. Wolverton, and E. D. Isaacs, “Electrical energy storage for transportation - Approaching the limits of, and going beyond, lithium-ion batteries,” *Energy and Environmental Science*, vol. 5, no. 7. Royal Society of Chemistry, pp. 7854–7863, 2012. doi: 10.1039/c2ee21892e.

[15] X. Hu, F. Feng, K. Liu, L. Zhang, J. Xie, and B. Liu, “State estimation for advanced battery management: Key challenges and future trends,” *Renewable and Sustainable Energy Reviews*, vol. 114. Elsevier Ltd, Oct. 01, 2019. doi: 10.1016/j.rser.2019.109334.

[16] M. Ecker *et al.*, “Development of a lifetime prediction model for lithium-ion batteries based on extended accelerated aging test data,” *J Power Sources*, vol. 215, pp. 248–257, Oct. 2012, doi: 10.1016/j.jpowsour.2012.05.012.

[17] B. Saha and K. Goebel, “Modeling Li-ion Battery Capacity Depletion in a Particle Filtering Framework,” 2009.

[18] W. Xia, A. Mahmood, R. Zou, and Q. Xu, “Metal-organic frameworks and their derived nanostructures for electrochemical energy storage and conversion,” *Energy and Environmental Science*, vol. 8, no. 7. Royal Society of Chemistry, pp. 1837–1866, Jul. 01, 2015. doi: 10.1039/c5ee00762c.

[19] C. Parag Jose and S. Meikandasivam, “A review on the trends and developments in hybrid electric vehicles,” *Lecture Notes in Mechanical Engineering*, vol. PartF9, pp. 211–229, 2017, doi: 10.1007/978-981-10-1771-1_25.

[20] Kazunori. Ozawa, *Lithium ion rechargeable batteries*. Wiley-VCH, 2009.

[21] K. Aifantis, S. Hackney, and R. Vasant Kumar, *High Energy Density Lithium Batteries*. Wiley-VCH, 2010.

[22] G. Graber, “Electric Mobility: Smart Transportation in Smart Cities COSMO-Cooperative Systems for Sustainable Mobility and Energy Efficiency View project,” 2016, doi: 10.13140/RG.2.1.2360.0240.

[23] W. Choi, H. C. Shin, J. M. Kim, J. Y. Choi, and W. S. Yoon, “Modeling and applications of electrochemical impedance spectroscopy (Eis) for lithium-ion batteries,” *Journal of Electrochemical Science and Technology*, vol. 11, no. 1. Korean Electrochemical Society, pp. 1–13, Feb. 01, 2020. doi: 10.33961/jecst.2019.00528.

[24] J. Kasnatscheew, R. Wagner, M. Winter, and I. Cekic-Laskovic, “Interfaces and Materials in Lithium Ion Batteries: Challenges for Theoretical Electrochemistry,” *Topics in Current Chemistry*, vol. 376, no. 3. Springer International Publishing, Jun. 01, 2018. doi: 10.1007/s41061-018-0196-1.

[25] X. Zeng, J. Li, and N. Singh, “Recycling of spent lithium-ion battery: A critical review,” *Critical Reviews in Environmental Science and Technology*, vol. 44, no. 10. Taylor and Francis Inc., pp. 1129–1165, May 19, 2014. doi: 10.1080/10643389.2013.763578.

[26] Ç. Ün, K. Aydin, C. Un, and K. Aydin, “Thermal Runaway and Fire Suppression for electric vehicle batteries,” 2020.

[27] F. C. Krause *et al.*, “Performance of Commercial Li-Ion Cells for Future NASA Missions and Aerospace Applications,” *J Electrochem Soc*, vol. 168, no. 4, p. 040504, Apr. 2021, doi: 10.1149/1945-7111/abf05f.

[28] N. Omar *et al.*, “Rechargeable energy storage systems for plug-in hybrid electric vehicles-assessment of electrical characteristics,” *Energies (Basel)*, vol. 5, no. 8, pp. 2952–2988, 2012, doi: 10.3390/en5082952.

[29] H. Zappen, G. Fuchs, A. Gitis, and D. U. Sauer, “In-operando impedance spectroscopy and ultrasonic measurements during high-temperature abuse experiments on lithium-ion batteries,” *Batteries*, vol. 6, no. 2, Jun. 2020, doi: 10.3390/batteries6020025.

[30] *Lithium-Ion Batteries Solid-Electrolyte Interphase*.

[31] T. Raj, A. A. Wang, C. W. Monroe, and D. A. Howey, “Investigation of Path-Dependent Degradation in Lithium-Ion Batteries,” *Batter Supercaps*, vol. 3, no. 12, pp. 1377–1385, Dec. 2020, doi: 10.1002/batt.202000160.

[32] E. M. Börger *et al.*, “Aging of ceramic coated graphitic negative and NCA positive electrodes in commercial lithium-ion battery cells – An ex-situ study of different states of health for identification and quantification of aging influencing parameters,” *J Energy Storage*, vol. 13, pp. 304–312, Oct. 2017, doi: 10.1016/j.est.2017.07.026.

[33] G. Dong and J. Wei, “A physics-based aging model for lithium-ion battery with coupled chemical/mechanical degradation mechanisms,” *Electrochim Acta*, vol. 395, Nov. 2021, doi: 10.1016/j.electacta.2021.139133.

[34] P. Kurzweil and M. Shamonin, “State-of-charge monitoring by impedance spectroscopy during long-term self-discharge of supercapacitors and lithium-ion batteries,” *Batteries*, vol. 4, no. 3, Sep. 2018, doi: 10.3390/batteries4030035.

[35] Q. Kellner, E. Hosseinzadeh, G. Chouchelamane, W. D. Widanage, and J. Marco, “Battery cycle life test development for high-performance electric vehicle applications,” *J Energy Storage*, vol. 15, pp. 228–244, Feb. 2018, doi: 10.1016/j.est.2017.11.019.

[36] S. S. Zhang, “Unveiling Capacity Degradation Mechanism of Li-ion Battery in Fast-charging Process,” *ChemElectroChem*, vol. 7, no. 2, pp. 555–560, Jan. 2020, doi: 10.1002/celc.201902050.

[37] R. Fang *et al.*, “Degradation mechanism and performance enhancement strategies of LiNixCoyAl1−x−yO2 (x ≥ 0.8) cathodes for rechargeable lithium-ion batteries: a review,” *Ionics*, vol. 26, no. 7. Springer, pp. 3199–3214, Jul. 01, 2020. doi: 10.1007/s11581-020-03569-7.

[38] X. Li *et al.*, “Degradation mechanisms of high capacity 18650 cells containing Si-graphite anode and nickel-rich NMC cathode,” *Electrochim Acta*, vol. 297, pp. 1109–1120, Feb. 2019, doi: 10.1016/j.electacta.2018.11.194.

[39] Y. Preger *et al.*, “Degradation of Commercial Lithium-Ion Cells as a Function of Chemistry and Cycling Conditions,” *J Electrochem Soc*, vol. 167, no. 12, p. 120532, Jan. 2020, doi: 10.1149/1945-7111/abae37.

[40] H. Chaoui, N. Golbon, I. Hmouz, R. Souissi, and S. Tahar, “Lyapunov-based adaptive state of charge and state of health estimation for lithium-ion batteries,” *IEEE Transactions on Industrial Electronics*, vol. 62, no. 3, pp. 1610–1618, 2015, doi: 10.1109/TIE.2014.2341576.

[41] L. Ungurean, G. Cârstoiu, M. v. Micea, and V. Groza, “Battery state of health estimation: a structured review of models, methods and commercial devices,” *International Journal of Energy Research*, vol. 41, no. 2. John Wiley and Sons Ltd, pp. 151–181, Feb. 01, 2017. doi: 10.1002/er.3598.

[42] G. Mulder *et al.*, “Enhanced test methods to characterise automotive battery cells,” *J Power Sources*, vol. 196, no. 23, pp. 10079–10087, Dec. 2011, doi: 10.1016/j.jpowsour.2011.07.072.

[43] Panasonic, “Panasonic Lithium-ion NCR18650B datasheet”. https://www.omnitron.cz/441-katalog-panasonic-nicd-akumulatory-panasonic (acessed Mar. 29, 2022).

[44] G. Instruments, “Basics of Electrochemical Impedance Spectroscopy.” https://www.gamry.com/application-notes/EIS/basics-of-electrochemical-impedance-spectroscopy/ (accessed Apr. 2, 2022).

[45] A. Kilic and D. Eroglu, “Characterization of the Effect of Cell Design on Li−S Battery Resistance Using Electrochemical Impedance Spectroscopy,” *ChemElectroChem*, vol. 8, no. 5, pp. 963–971, Mar. 2021, doi: 10.1002/celc.202100165.

[46] F. Single, B. Horstmann, and A. Latz, “Theory of Impedance Spectroscopy for Lithium Batteries,” *Journal of Physical Chemistry C*, 2019, doi: 10.1021/acs.jpcc.9b07389.

[47] J. S. Fernandes, *Espectroscopia de Impedância Electroquímica*. 2000. IST, Lisboa.

[48] H. Dai, B. Jiang, and X. Wei, “Impedance characterization and modeling of lithium-ion batteries considering the internal temperature gradient,” *Energies (Basel)*, vol. 11, no. 1, 2018, doi: 10.3390/en11010220.

[49] J. Huang, J. Zhang, Z. Li, S. Song, and N. Wu, “Exploring Differences between charge and discharge of limn 2o4/li half-cell with dynamic electrochemical impedance spectroscopy,” *Electrochim Acta*, vol. 131, pp. 228–235, Jun. 2014, doi: 10.1016/j.electacta.2014.02.030.

[50] J. L. Jespersen, A. E. Tønnesen, K. Nørregaard, L. Overgaard, and F. Elefsen, “Capacity Measurements of Li-Ion Batteries using AC Impedance Spectroscopy,” *World Electric Vehicle Journal*, vol. 3, pp. 127–133, May 2009.

[51] Q. A. Huang, Y. Shen, Y. Huang, L. Zhang, and J. Zhang, “Impedance Characteristics and Diagnoses of Automotive Lithium-Ion Batteries at 7.5% to 93.0% State of Charge,” *Electrochim Acta*, vol. 219, pp. 751–765, Nov. 2016, doi: 10.1016/j.electacta.2016.09.154.

[52] S. S. Zhang, “Identifying rate limitation and a guide to design of fast-charging Li-ion battery,” *InfoMat*, vol. 2, no. 5, pp. 942–949, Sep. 2020, doi: 10.1002/inf2.12058.

[53] Panasonic, “Panasonic Lithium-ion NCR18650 datasheet”. https://www.batteryspace.com/li-ioncylindricalcellseries.aspx/ (accessed Mar. 17, 2022).

Appendix

Appendix A – EEC fitting results

Table 1: Parameters obtained by EEC for the charged used cell.

Cycle	Chi-Sqr	Sum-Sqr	Rint(+)	CPE1-T(+)	CPE1-P(+)	RSEI(+)	CPE2-T(+)	CPE2-P(+)	RCT(+)	Wo(+)	Wo-T(+)	Wo-P(+)
1	9.24E-06	0.000554	0.065307	2.771	0.57195	0.009317	5.986	0.92924	0.061731	0.060005	86.83	0.61282
2	7.96E-06	0.000478	0.072404	1.52	0.74839	0.006711	5.923	0.9192	0.066605	0.066177	102.5	0.62375
3	7.97E-06	0.000478	0.075596	1.492	0.7478	0.006394	5.963	0.91538	0.061571	0.064259	102.5	0.60926
4	8.05E-06	0.000483	0.075817	5.221	0.4471	0.012331	6.257	0.94637	0.057992	0.073458	135.5	0.58514
5	6.85E-06	0.000411	0.083938	2.452	0.64117	0.007684	6.11	0.93004	0.056586	0.062454	97.43	0.60138
6	6.75E-06	0.000405	0.087696	1.811	0.72329	0.00655	6.049	0.9246	0.056318	0.067512	115.4	0.60013
7	8.29E-06	0.000497	0.086704	2.402	0.69013	0.00683	6.13	0.92735	0.055734	0.064608	104.1	0.60076
8	8.25E-06	0.000495	0.084167	3.779	0.53571	0.009092	6.214	0.93512	0.050668	0.058373	94.54	0.5902
9	5.50E-06	0.00033	0.097532	2.048	0.64426	0.007384	6.082	0.92841	0.05337	0.061065	97.61	0.59454
10	5.76E-06	0.000346	0.10153	2.15	0.72192	0.006102	6.134	0.93258	0.049856	0.065127	112	0.59454
11	6.09E-06	0.000365	0.10742	3.63	0.59454	0.008486	6.218	0.93727	0.058126	0.066694	108.6	0.59574
12	4.65E-06	0.000279	0.11494	2.272	0.68717	0.00685	6.189	0.92623	0.053854	0.06939	122.9	0.59854
13	4.43E-06	0.000266	0.11662	2.167	0.6541	0.007546	6.175	0.92309	0.060058	0.064397	102	0.60591
14	5.09E-06	0.000306	0.11815	2.793	0.5917	0.008345	6.173	0.92814	0.056849	0.061949	93.87	0.59701

15	4.74E-06	0.000285	0.11736	2.563	0.62355	0.008322	6.204	0.92678	0.062766	0.06995	117.7	0.59189
16	4.45E-06	0.000267	0.11819	2.197	0.6496	0.007824	6.175	0.92567	0.062324	0.066699	106.8	0.59746
17	3.88E-06	0.000233	0.11694	2.604	0.58755	0.008781	6.262	0.92147	0.063018	0.064114	99.89	0.60788
18	4.36E-06	0.000262	0.11882	1.994	0.65492	0.007759	6.185	0.91751	0.064882	0.063446	96.92	0.60634
19	3.66E-06	0.00022	0.12808	1.951	0.69947	0.007304	6.174	0.92425	0.064109	0.06942	114.2	0.59986
20	3.95E-06	0.000237	0.12644	2.54	0.61459	0.00875	6.241	0.92457	0.065569	0.06567	102.7	0.59989
21	3.48E-06	0.000209	0.12682	2.813	0.54363	0.010013	6.214	0.92992	0.064255	0.063129	98.13	0.59578
22	4.10E-06	0.000246	0.12985	1.83	0.70627	0.00769	6.16	0.92238	0.070073	0.070306	115.2	0.59362
23	3.27E-06	0.000196	0.12856	3.264	0.53268	0.010533	6.243	0.93359	0.065023	0.06496	102.7	0.59232
24	3.62E-06	0.000217	0.12956	2.068	0.67037	0.008074	6.242	0.91506	0.072629	0.066575	101.5	0.61861
25	3.23E-06	0.000194	0.13908	1.656	0.69073	0.008005	6.226	0.91192	0.070391	0.065244	102.5	0.60804
26	2.84E-06	0.00017	0.15294	2.018	0.67199	0.008669	6.242	0.92499	0.067387	0.065649	106.8	0.60314
27	2.86E-06	0.000172	0.1559	2.093	0.62145	0.009471	6.25	0.9206	0.067214	0.06175	94.42	0.60578
28	2.05E-06	0.000123	0.18203	2.8	0.52614	0.011668	6.265	0.92491	0.061731	0.057502	85.4	0.60636
29	1.83E-06	0.00011	0.1821	1.712	0.695	0.008263	6.157	0.92078	0.057097	0.060533	105.6	0.59355
30	1.80E-06	0.000108	0.19075	1.802	0.66032	0.008649	6.236	0.91642	0.055393	0.056155	92.56	0.61192
31	1.94E-06	0.000117	0.18505	2.253	0.59819	0.01004	6.21	0.92589	0.055987	0.057971	96.74	0.58637
32	1.73E-06	0.000104	0.18365	4.316	0.41904	0.014712	6.471	0.93616	0.05247	0.055826	91.22	0.59513
33	2.19E-06	0.000132	0.1843	2.318	0.64192	0.009331	6.259	0.93086	0.05786	0.06356	115.5	0.57885
34	1.86E-06	0.000111	0.1768	4.275	0.44531	0.013835	6.441	0.93686	0.055134	0.059911	100.1	0.58531

35	2.13E-06	0.000128	0.17441	2.722	0.53353	0.012103	6.331	0.92749	0.061065	0.059992	91.81	0.59635
36	2.40E-06	0.000144	0.17245	2.712	0.60429	0.009597	6.408	0.92513	0.057421	0.061022	102.1	0.5931
37	2.20E-06	0.000132	0.17373	1.932	0.67217	0.009176	6.255	0.9216	0.064293	0.063047	106.2	0.59805
38	2.22E-06	0.000133	0.17378	2.756	0.55811	0.010627	6.397	0.92088	0.057277	0.057324	85.85	0.60796
39	1.82E-06	0.000109	0.18082	1.994	0.64682	0.009242	6.254	0.92084	0.060637	0.060951	101.8	0.59752
40	2.09E-06	0.000126	0.18297	2.977	0.52808	0.011392	6.355	0.92516	0.056626	0.059299	93.55	0.59271
41	2.08E-06	0.000125	0.19164	2.074	0.63749	0.009865	6.32	0.91768	0.060348	0.059987	101.6	0.60258
42	1.75E-06	0.000105	0.18854	1.95	0.64823	0.009275	6.29	0.9205	0.057334	0.060683	103	0.58703
43	1.80E-06	0.000108	0.19138	2.881	0.51937	0.012283	6.442	0.92145	0.055855	0.054324	87.42	0.60813
44	2.06E-06	0.000123	0.19233	2.851	0.56085	0.010931	6.376	0.93125	0.053135	0.059912	100.4	0.58141
45	2.05E-06	0.000123	0.1988	2.297	0.65512	0.008734	6.37	0.91436	0.052921	0.058083	100.6	0.6053
46	1.94E-06	0.000116	0.19864	6.023	0.3813	0.016731	6.678	0.95585	0.047026	0.059005	102.1	0.58074
47	2.04E-06	0.000122	0.20601	3.62	0.54454	0.01129	6.528	0.94082	0.048399	0.059857	109.4	0.57217
48	1.43E-06	8.57E-05	0.2118	1.872	0.66437	0.008765	6.311	0.92008	0.050342	0.057952	102.5	0.58769
49	1.83E-06	0.00011	0.21269	1.563	0.69299	0.008181	6.276	0.90853	0.049278	0.055191	95.43	0.60107
50	1.88E-06	0.000113	0.22063	2.633	0.58056	0.01029	6.3	0.92458	0.047025	0.058094	104.5	0.57727

Table 2: Errors in value (E) and percentage (E%) of the parameters obtained by EEC for the charged used cell.

Cycle	Rint (E)	Rint (E%)	CPE1-T(E)	CPE1-T (E%)	CPE1-P (E)	CPE1-P (E%)	RSEI (E)	RSEI (E%)	CPE2-T (E)	CPE2-T (E%)	CPE2-P (E)	CPE2-P (E%)	RCT (E)	RCT (E%)	Wo (E)	Wo (E%)	Wo-T (E)	Wo-T (E%)	Wo-P (E)	Wo-P (E%)
1	0.000221	0.33787	0.40981	14.789	0.044112	7.7126	0.000476	5.1057	0.059465	0.9934	0.007716	0.83037	0.000939	1.521	0.006038	10.062	20.631	23.76	0.025979	4.2393
2	0.000215	0.29631	0.34128	22.453	0.042176	5.6356	0.000435	6.4751	0.053276	0.89948	0.006837	0.74384	0.00086	1.2913	0.005377	8.1244	17.202	16.782	0.023928	3.8362
3	0.000209	0.27673	0.35768	23.973	0.046446	6.211	0.000428	6.6858	0.061219	1.0266	0.007575	0.82757	0.00089	1.4454	0.005725	8.9093	19.573	19.096	0.025408	4.1703
4	0.000263	0.34701	0.66691	12.774	0.049526	11.077	0.000648	5.2534	0.06756	1.0798	0.008988	0.94974	0.001071	1.8466	0.007317	9.9613	25.269	18.649	0.025798	4.4089
5	0.000218	0.25993	0.44337	18.082	0.049413	7.7067	0.00047	6.111	0.06621	1.0836	0.008256	0.8877	0.000898	1.5863	0.005734	9.1813	19.929	20.455	0.02462	4.0939
6	0.000219	0.24973	0.45259	24.991	0.050752	7.0168	0.000475	7.2468	0.068054	1.125	0.008497	0.91902	0.000902	1.6017	0.00668	9.8945	23.472	20.34	0.024191	4.031
7	0.000251	0.28898	0.60992	25.392	0.057695	8.36	0.000575	8.4234	0.077038	1.2567	0.009764	1.0529	0.001047	1.8791	0.006172	9.5535	21.496	20.649	0.027722	4.6145
8	0.000242	0.28737	0.66712	17.653	0.059486	11.104	0.000584	6.4215	0.083095	1.3372	0.010473	1.12	0.001036	2.0451	0.007243	12.408	26.624	28.162	0.026927	4.5624
9	0.000217	0.22297	0.47719	23.3	0.053452	8.2967	0.000467	6.3233	0.07094	1.1664	0.008732	0.9405	0.000884	1.657	0.006328	10.362	22.985	23.548	0.02398	4.0334
10	0.000228	0.2241	0.61195	28.463	0.05871	8.1325	0.000527	8.6408	0.08046	1.3117	0.009939	1.0658	0.000933	1.8722	0.006421	9.8597	23.652	21.118	0.024582	4.1346
11	0.000298	0.27743	0.80747	22.244	0.060257	10.135	0.000722	8.5038	0.076763	1.2345	0.010109	1.0786	0.001174	2.0196	0.007002	10.498	24.318	22.392	0.027906	4.6843
12	0.000223	0.19438	0.49467	21.772	0.055318	8.0501	0.00049	7.1534	0.072015	1.1636	0.008912	0.96216	0.000889	1.6506	0.006745	9.7197	23.641	19.236	0.022948	3.834

13	0.000232	0.19916	0.45485	20.99	0.052475	8.0225	0.000486	6.4389	0.064377	1.0425	0.008092	0.87661	0.000916	1.5244	0.005878	9.1279	19.859	19.47	0.024074	3.9732
14	0.000262	0.22212	0.6244	22.356	0.060816	10.278	0.000584	7.0021	0.074996	1.2149	0.009508	1.0244	0.001041	1.8317	0.005974	9.6437	20.525	21.865	0.026725	4.4765
15	0.000268	0.22827	0.58761	22.927	0.053468	8.5748	0.000604	7.2541	0.0667	1.0751	0.00879	0.94847	0.001085	1.7291	0.00748	10.694	25.685	21.822	0.026137	4.4159
16	0.00025	0.21175	0.52029	23.682	0.052304	8.0517	0.000543	6.9397	0.064464	1.044	0.008358	0.90287	0.001011	1.6223	0.006427	9.6364	21.962	20.564	0.025567	4.2793
17	0.00023	0.19634	0.44877	17.234	0.048808	8.307	0.000481	5.4785	0.058115	0.92806	0.007404	0.80354	0.000888	1.4086	0.005407	8.4333	17.699	17.718	0.02274	3.7409
18	0.000251	0.21092	0.48724	24.435	0.052173	7.9663	0.000525	6.769	0.06164	0.9966	0.007925	0.86375	0.000987	1.5211	0.005991	9.4433	19.824	20.454	0.025135	4.1454
19	0.00025	0.19502	0.47795	24.498	0.049782	7.1171	0.00053	7.2501	0.060212	0.97525	0.007844	0.84873	0.000973	1.5172	0.006422	9.2512	21.752	19.047	0.024205	4.0351
20	0.000263	0.20838	0.49241	19.386	0.05037	8.1957	0.000561	6.4112	0.061056	0.9783	0.007994	0.86463	0.001029	1.5689	0.006123	9.3245	20.507	19.968	0.025755	4.2933
21	0.000252	0.1985	0.48455	17.225	0.048837	8.9835	0.000533	5.3273	0.058709	0.94479	0.007698	0.82778	0.000978	1.5223	0.006369	10.088	21.731	22.145	0.024249	4.0701
22	0.000275	0.21191	0.45889	25.076	0.049522	7.0118	0.000577	7.5053	0.06071	0.98555	0.008122	0.88057	0.001152	1.6436	0.007829	11.135	27.21	23.62	0.028456	4.7936
23	0.000259	0.20136	0.51138	15.667	0.046703	8.7676	0.000571	5.4174	0.05755	0.92183	0.007698	0.82452	0.00101	1.5533	0.006505	10.014	22.328	21.741	0.024227	4.0902
24	0.000289	0.22299	0.50031	24.193	0.04821	7.1916	0.000599	7.4232	0.054688	0.87613	0.007259	0.79324	0.001023	1.4084	0.005367	8.061	16.966	16.715	0.024903	4.0256
25	0.000259	0.1864	0.37889	22.88	0.046666	6.756	0.000516	6.4415	0.05551	0.89158	0.007201	0.78969	0.00098	1.3917	0.005582	8.5554	18.447	17.997	0.025318	4.1639
26	0.00029	0.18954	0.45584	22.589	0.046427	6.9089	0.000619	7.1359	0.060232	0.96495	0.00801	0.86596	0.001069	1.5861	0.006187	9.4247	21.654	20.275	0.026511	4.3955

27	0.000298	0.1911	0.46363	22.151	0.048362	7.7821	0.000629	6.6457	0.062544	1.0007	0.008292	0.90067	0.001109	1.6504	0.006342	10.271	22.517	23.848	0.02774	4.5792
28	0.000308	0.16909	0.48892	17.461	0.048405	9.2	0.000673	5.7659	0.066693	1.0645	0.008831	0.95482	0.001101	1.784	0.006365	11.07	24.181	28.315	0.027269	4.4972
29	0.000272	0.1496	0.39796	23.245	0.04577	6.5856	0.000579	7.0015	0.066449	1.0792	0.008537	0.92716	0.000947	1.6584	0.005496	9.0788	21.461	20.323	0.024969	4.2067
30	0.000294	0.15417	0.45844	25.441	0.049383	7.4786	0.000627	7.2545	0.070741	1.1344	0.008825	0.96293	0.000917	1.6556	0.004452	7.9273	16.648	17.986	0.024148	3.9463
31	0.000291	0.1572	0.44158	19.6	0.048505	8.1086	0.00063	6.2789	0.071566	1.1524	0.009179	0.99132	0.00102	1.8222	0.005956	10.274	23.536	24.329	0.026499	4.5192
32	0.000307	0.16708	0.57891	13.413	0.049318	11.769	0.000717	4.8737	0.074731	1.1549	0.009431	1.0074	0.001023	1.9501	0.00543	9.7268	21.275	23.323	0.024698	4.15
33	0.000342	0.18562	0.57429	24.775	0.051004	7.9455	0.000785	8.4125	0.077409	1.2368	0.010144	1.0897	0.001211	2.0925	0.007504	11.806	30.454	26.367	0.029123	5.0312
34	0.000311	0.17578	0.57686	13.494	0.048334	10.854	0.000723	5.2284	0.071532	1.1106	0.009176	0.97948	0.001063	1.9277	0.00583	9.7309	22.737	22.714	0.025357	4.3322
35	0.000307	0.1763	0.44962	16.518	0.045335	8.4972	0.00068	5.6207	0.068044	1.0748	0.008988	0.9691	0.001137	1.8616	0.006744	11.241	26.534	28.901	0.028222	4.7325
36	0.000328	0.19014	0.61491	22.674	0.052619	8.7076	0.00076	7.9213	0.077648	1.2117	0.009912	1.0715	0.001152	2.0061	0.006131	10.048	23.314	22.834	0.027629	4.6584
37	0.000316	0.18198	0.44376	22.969	0.044986	6.6927	0.000684	7.4535	0.064455	1.0305	0.008488	0.92103	0.001097	1.7058	0.005791	9.1849	21.476	20.222	0.027241	4.555
38	0.000303	0.17435	0.52266	18.964	0.050297	9.012	0.00068	6.4018	0.073638	1.1511	0.009415	1.0224	0.001076	1.8788	0.005748	10.027	21.727	25.308	0.026614	4.3776
39	0.000302	0.16709	0.46016	23.077	0.045034	6.9624	0.000656	7.101	0.064572	1.0325	0.008408	0.9131	0.001016	1.6747	0.00567	9.3026	21.563	21.182	0.025104	4.2014
40	0.000327	0.17854	0.57094	19.178	0.051615	9.7741	0.000747	6.5578	0.077435	1.2185	0.009977	1.0784	0.001161	2.0496	0.006464	10.901	25.564	27.327	0.028202	4.7581

41	0.000342	0.17828	0.48209	23.244	0.04859	7.6221	0.000754	7.6416	0.074026	1.1713	0.00948	1.0331	0.00113	1.8725	0.005867	9.78	22.129	21.781	0.027931	4.6352
42	0.000284	0.15058	0.40473	20.755	0.045673	7.0458	0.00061	6.5743	0.069386	1.1031	0.008891	0.96593	0.001022	1.7824	0.006019	9.9194	23.959	23.261	0.026221	4.4667
43	0.000326	0.17025	0.49368	17.136	0.04785	9.2131	0.000729	5.9371	0.07476	1.1605	0.009456	1.0262	0.001052	1.8829	0.005833	10.737	22.671	25.933	0.025754	4.2349
44	0.000334	0.17348	0.55574	19.493	0.053038	9.4567	0.000764	6.9913	0.084501	1.3253	0.010712	1.1503	0.001171	2.2036	0.006311	10.534	25.427	25.326	0.028934	4.9765
45	0.000362	0.18218	0.66476	28.94	0.056925	8.6892	0.000858	9.8224	0.090725	1.4243	0.011085	1.2123	0.001155	2.1821	0.005144	8.857	19.738	19.62	0.027574	4.5554
46	0.000371	0.18693	0.77641	12.891	0.05728	15.022	0.000946	5.6554	0.099206	1.4856	0.012281	1.2848	0.001289	2.7415	0.007147	12.113	30.121	29.501	0.029097	5.0103
47	0.000386	0.18732	0.83676	23.115	0.05889	10.815	0.00103	9.1187	0.1091	1.6713	0.013355	1.4195	0.001394	2.8796	0.007976	13.325	34.501	31.537	0.030765	5.3769
48	0.000274	0.1296	0.41301	22.063	0.048092	7.2387	0.000604	6.8926	0.079048	1.2525	0.009743	1.0589	0.000953	1.8929	0.005491	9.4756	22.59	22.039	0.025041	4.2609
49	0.000314	0.14743	0.48494	31.026	0.055767	8.0473	0.0007	8.5517	0.093325	1.487	0.011328	1.2468	0.001053	2.1373	0.005575	10.101	22.709	23.797	0.027832	4.6304
50	0.000357	0.16159	0.6005	22.807	0.059626	10.27	0.00084	8.1632	0.10427	1.6551	0.012944	1.4	0.001233	2.6209	0.00722	12.429	31.243	29.898	0.03059	5.2991